SINGLE PROBE IN-CIRCUIT IMPEDANCE EXTRACTION BASED ON INDUCTIVE COUPLING APPROACH

SUDHARMA DESHAPRIYA KOTUWEGEDARA HARSHA
YASHOMAN ARJUNA WEERASINGHE

School of Electrical & Electronic Engineering

A thesis submitted to the Nanyang Technological University
in partial fulfillment of the requirement for the degree of
Doctor of Philosophy

2022

STATEMENT OF ORIGINALITY

I hereby certify that the work embodied in this thesis is the result of original research, is free of plagiarised materials, and has not been submitted for a higher degree to any other University or Institution.

16-07-2021

. . . . . .

Date

. . . . . .

Sudharma Deshapriya Kotuwegedara Harsha
Yashoman Arjuna Weerasinghe

SUPERVISOR DECLARATION STATEMENT

I have reviewed the content and presentation style of this thesis and declare it is free of plagiarism and of sufficient grammatical clarity to be examined. To the best of my knowledge, the research and writing are those of the candidate except as acknowledged in the Author Attribution Statement. I confirm that the investigations were conducted in accord with the ethics policies and integrity standards of Nanyang Technological University and that the research data are presented honestly and without prejudice.

05-04-2022

Date

Kye Yak See

AUTHORSHIP ATTRIBUTION STATEMENT

This thesis contains material from 5 papers published in the following peer-reviewed journals / from papers accepted at conferences in which I am listed as an author.

Chapter 3, Chapter 5 Section 5.1 and 5.2, and Chapter 6 are published as A. Weerasinghe, Z. Zhao, N. B. Narampanawe, T. Svimonishvili, Z. Yang and K. Y. See, "Single-Probe Inductively Coupled In-Circuit Impedance Measurement" IEEE Transactions on Electromagnetic Compatibility, 2021, DOI: 10.1109/TEMC.2021.3091761.

The contributions of the co-authors are as follows:

- A/Prof See Kye Yak, Z. Zhao, T. Svimonishvili, Z. Yang edited the manuscript drafts.
- I prepared the manuscript drafts and drew figures. The manuscript was revised by See Kye Yak, Z. Zhao, T. Svimonishvili.
- I, N. B. Narampanawe and Z. Zhao performed the laboratory work at the School of Electrical and Electronic Engineering
- I and Z. Zhao analyzed and interpreted the data.

Chapter 4 has been submitted to IEEE Transactions on Industrial Electronics as A. Weerasinghe, Z. Zhao, Q. Sun, F. Fan, P. Tu, W. Wang, and K. Y. See, A Novel Single-Probe Setup for Multi-Frequency Simultaneous Measurement of In-Circuit Impedance.

The contributions of the co-authors are as follows:

- I developed the fundamental derivations and performed equipment programming, setting up and data collection.

- I and Z. Zhao analyzed data and wrote the drafts of the manuscript.
- The manuscript was revised together with A/Prof See Kye Yak, Q. Sun, F. Fan, P. Tu, and W. Wang.

Chapter 5 has been accepted to Asia-Pacific International Symposium on Electromagnetic Compatibility (APEMC), Beijing, 2022 as Arjuna Weerasinghe, Zhenyu Zhao, Wensong Wang, Huamin Jie, and Kye Yak See, Inductively Coupled In-Circuit Impedance Measurement Under Low Signal-To-Noise Ratio.

The contributions of the co-authors are as follows:

- I developed the fundamental conceptual derivations.
- I and Z. Zhao wrote the drafts of the manuscript.
- The manuscript is revised together with A/Prof See Kye Yak, Wensong Wang, and Huamin Jie.
- I performed laboratory data collection, interpretation, and drew figures.

Chapter 6 has been published as A. Weerasinghe, Z. Zhao, F. Fan, P. Tu, K. Y. See, "In-Circuit Differential-Mode Impedance Extraction at the AC Input of a Motor Drive System," Asia-Pacific International Symposium on Electromagnetic Compatibility (APEMC), Bali, 2021.

The contributions of the co-authors are as follows:

- I prepared the manuscript drafts and drew figures. The manuscript was revised by See Kye Yak, Z. Zhao, F. Fan, P. Tu.
- I performed laboratory work at the School of Electrical and Electronic Engineering.
- I and Z. Zhao analyzed and interpreted the data.

And Z. Zhao, F. Fan, A. Weerasinghe, P. Tu, K. Y. See, "Measurement of In-Circuit Common-Mode Impedance at the AC Input of a Motor Drive System," Asia-Pacific International Symposium on Electromagnetic Compatibility (APEMC), Bali, 2021.

The contributions of the co-authors are as follows:

- Z. Zhao prepared the manuscript drafts. The manuscript was revised by me, See Kye Yak, Z. Zhao, F. Fan, P. Tu.
- I performed laboratory work at the School of Electrical and Electronic Engineering.
- F. Fan, Z. Zhao, and I analyzed and interpreted the data.

18-02-2022

. . . . . .

Date

. . . . . .

Sudharma Deshapriya Kotuwegedara Harsha Yashoman Arjuna Weerasinghe

ACKNOWLEDGEMENTS

I would like to express my enormous gratitude towards my supervisor, Associate Professor See Kye Yak. His guidance, generous support, and inspiration were immense. My genuine appreciations also go to Ms. Alexandra Chua, the laboratory manager of SMRT-NTU Smart Urban Rail Corporate Laboratory, and Mr. Wee Seng Khoon and Mr. Yuen Sien, the technical staff of Electronic System Reliability Laboratory, for their technical support. Also, I would like to thank fellow research staff and Ph.D. students, Dr. Chua Eng Kee, Dr. Arun Shankar Narayanan, Dr. Tengiz Svimonishvili, Dr. Narampanawe, Dr. Sooriya Bandara, Dr. Li Kang Rong, Dr. Manish Prajapati, Dr. Fan Fei, Dr. Zhao Zhenyu, Mr. Yang Zhenning and Mr. Jeremy Chua for their technical advice and friendship. Finally, I wish to convey my love and heartfelt gratitude to my beloved girlfriend, parents for their uncompromising love and understanding, and continuous encouragement throughout the period of my study. I dedicate my thesis to them.

TABLE OF CONTENTS

ABSTRACT

The in-circuit impedance of a critical electrical system provides valuable information on its operating status and health. There are three common in-circuit impedance measurement approaches, namely the voltage-current (V-I) measurement approach, the capacitive coupling approach, and the inductive coupling approach. Among them, the inductive coupling approach does not require a direct electrical contact to the energized system-under-test (SUT) and therefore greatly simplifies the implementation without the need to shut down the system and eliminates the concern of electrical safety hazards.

The conventional measurement setup of the inductive coupling approach requires two inductive probes and a two-port vector network analyzer (VNA) or a signal generation and data acquisition system (SGAS). This well-established two-probe setup (TPS) has been refined and improved over the years. Despite all these recent improvements, it still cannot eliminate the inherent probe-to-probe coupling which compromises the measurement accuracy when the two probes are placed very close to each other.

This thesis develops an in-circuit impedance measurement setup with the use of only one inductive probe and it is experimentally verified. By introducing a single-probe setup (SPS), not only reduces the hardware overhead of the measurement setup but also fundamentally addresses the concern of probe-to-probe coupling. In addition, the proposed SPS incorporates power amplification and protection devices to maintain the measurement system's accuracy and improve the ruggedness for in-circuit impedance measurement of electrical systems in harsh electromagnetic environments with the presence of strong background noise and transient events. An error correction scheme has also been developed to recover measurement

results contaminated with errors if the available signal-to-noise ratio (SNR) of the SPS is poor due to correlated noise interfering with the excitation signal.

The proposed SPS has also been designed so that it has the flexibility to extract in-circuit impedance using either frequency-domain (FD) or time-domain (TD) based instrumentation so that the application scope is broadened. The SPS TD-based instrumentation is capable of measuring time-varying in-circuit impedance at multiple frequencies simultaneously to improve its measurement efficiency.

To demonstrate the practical value of the proposed SPS, firstly, it is applied to extract the in-circuit differential-mode (DM) and common-mode (CM) impedances of a variable frequency drive (VFD) under different operating modes using FD-based instrumentation. Then, the in-circuit impedance of a grid-connected induction motor is extracted based on both FD and TD-based instrumentations. The measured in-circuit impedance of the induction motor is also compared against the conventional V-I measurement approach to showcase the measurement accuracy of the proposed SPS.

LIST OF FIGURES

LIST OF TABLES

LIST OF ABBREVIATIONS

AC – Alternating Current

CM – Common-mode

DC – Direct Current

DFT – Discrete Fourier Transform

DM – Differential -mode

DSP – Digital Signal Processing

EMC – Electromagnetic Compatibility

EMI – Electromagnetic Interference

ESL – Equivalent Series Inductance

FD – Frequency-Domain

FFT – Fast Fourier Transform

IA – Impedance Analyzer

OSL – Open-Short-Load

REF – Reference

RF – Radio Frequency

SLV – Sensor-less Vector

SMPS – Switch Mode Power Supply

SPS – Single-Probe Setup

SNR – Signal-to-Noise Ratio

SOC – State-of-Charge

SOH – State-of-Health

STDFT – Short Time Discrete Fourier Transform

SUT – System Under Test

TD – Time-Domain

VFD – Variable-Frequency Drive

V-I – Voltage-Current

VNA – Vector Network Analyzer

Chapter 1 Introduction

1.1 Background of In-Circuit Impedance Measurement

The in-circuit impedance of critical electrical assets, such as power converters and electrical machines, provides valuable information for electromagnetic interference (EMI) filter design and health monitoring purposes [1]–[6]. It serves as one of the key parameters that reflects the characteristics of the electrical system under its actual operating conditions [7], [8], which finds many practical applications [9]–[11]. For example, the in-circuit impedance of a battery provides information on its state-of-charge (SOC) and the state-of-health (SOH) [12], [13]; the stability criteria of a power converter can be established once its in-circuit impedance is known [14], and systematic EMI filter design of a switch-mode power supply (SMPS) becomes possible with the known in-circuit noise source equivalent model [15]. Given its practical value, various in-circuit impedance measurement methods have been reported. In general, these met. s are based on three basic approaches. These threefold approaches are the voltage-current (V-I) measurement approach [16]–[18], the capacitive coupling approach [19], [20], and the inductive coupling approach [21]–[23].

As opposed to the (V-I) measurement approach and the capacitive coupling approach, the system-under-test (SUT) does not establish a direct electrical connection in the inductive coupling approach [24]. The inductive probes are of the clamp-on type and can be easily attached on or detached from the insulated conductors that deliver power to the SUT, which can be easily implemented on-site without the concern of electrical safety hazards and without

the need to shut down the electrical power [25]. The inductive coupling approach has been implemented using two-probe and multi-probe setups to measure the in-circuit impedance [26], [27]. The multi-probe setup (MPS) has specific applications that are for simultaneous impedance measurement of multiple SUTs in multi-branch cables powered by the same power source [28]. The two-probe setup (TPS) is targeted for general purpose applications, which has been widely used to obtain in-circuit impedance of critical electrical systems, such as high voltage power delivery path [29], induction motor [30], and power converter [31].

The early development of the TPS has been mainly based on frequency-domain (FD) measurement instruments such as a vector network analyzer (VNA) [32] or a spectrum analyzer with a tracking generator [31]. Firstly, the two inductive probes are characterized offline using a calibration fixture and a two-port VNA so that two-port network parameters of the respective probes are obtained in terms of the transmission (*ABCD*) parameters [33]. Then, the inductive probes are attached to the power cables feeding the SUT by clamping to provide excitation and extract its in-circuit impedance. To identify time-variant in-circuit impedance, the TPS uses time-domain (TD) based instrumentation with digital signal processing (DSP) [34], [35]. Such TPS consists of a signal generation and data acquisition system (SGAS) to produce an excitation test signal at a specific frequency and to measure the response of the same signal [36]. Time-variant or time-invariant in-circuit impedance is extracted using a moving window discrete Fourier transform (MWDFT) technique [37]. The latest development of the TPS has incorporated signal amplification and protection (SAP) devices to improve the measurement system's signal-to-noise ratio (SNR) and ruggedness for SUTs with the presence of strong background noise and frequent power transients [38].

Despite the above-mentioned refinements and improvements of the TPS, its major issue is the undesirable probe-to-probe coupling when the two probes are physically placed very close to each other due to space constraints in some practical situations, which can compromise the

measurement accuracy [39]. Although a calibration and compensation method has been developed to correct the errors due to the probe-to-probe coupling, it can be a tedious process and havemustrepeated every time if the types of probes and spacing between probes change [40]. An improved characterization technique has been proposed in [41] but the extracted transfer impedance parameter alone is not sufficient to perform impedance measurements.

1.2 Motivation

Although the TPS of the inductive coupling approach has been refined and improved over the years, there are still several shortcomings to be addressed. As mentioned earlier, even there is a calibration method to compensate for the measurement errors due to probe-to-probe coupling when the probes are placed very close to each other, it can be cumbersome. For situations where there are space constraints to accommodate two probes with sufficient separation, the TPS becomes infeasible. Also, the cascaded representation of the SUT and the two probes are error-prone because the inductive probe characterization errors propagate to the final impedance measurement, especially at high frequencies.

Therefore, the motivation of this thesis is to explore the possibility of using a single inductive probe for the measurement setup so that the above-mentioned limitations can be overcome.

1.3 Objectives

The proposed single-probe setup (SPS) presented in this thesis aims to achieve the two main objectives:

- To derive the theory behind the SPS for in-circuit measurement and to validate it experimentally.
- To improve its robustness for practical applications.

1.4 Contributions

The major contributions are highlighted as below,

- Successful development and experimental validation of the SPS for in-circuit impedance extraction with frequency-domain (FD) and time-domain (TD) based instrumentation.
- Incorporating signal amplification and protection devices to enhance its measurement accuracy and ruggedness.
- Detailed analysis of the impact of SNR on the accuracy of in-circuit impedance extraction and proposing an error correction scheme.
- Development of a quasi-log multitone excitation signal algorithm with TD-based instrumentation to extract in-circuit impedance efficiently across a wide frequency band.

1.5 Organization of Thesis

The thesis has been organized as follows:

Chapter 1 elaborates the significance of in-circuit impedance measurement and gives an overview of the existing in-circuit impedance extraction approaches with a special focus on

the TPS of the inductive coupling approach. Accordingly, the motivation, objectives, and contributions of the work presented in the thesis are articulated.

Chapter 2 gives a comprehensive literature review on various in-circuit impedance extraction approaches and compares their strengths and limitations.

Chapter 3 describes the proposed SPS for in-circuit impedance measurement with FD-based instrumentation.

Chapter 4 extends the SPS with TD-based instrumentation. A multitone excitation signal synthesis technique and a digital signal processing (DSP) technique are described for simultaneous time-variant in-circuit impedance measurement at multiple frequencies.

Chapter 5 introduces signal amplification and protection features to tailor the SPS for high-power applications. Also, a non-statistical error correction scheme is proposed to recover measurement results contaminated with errors due to correlated noise interfering with the excitation signals.

Chapter 5 introduces signal amplification and protection features to the SPS to enhance its measurement accuracy and ruggedness in a harsh electromagnetic environment. Also, a novel error correction method is proposed to achieve measurement accuracy mathematically under situations where there is a limitation on SNR.

Chapter 6 demonstrates the practical application value of the proposed SPS with several test cases.

Finally, Chapter 7 concludes the thesis with suggestions for potential future work.

Chapter 2 Literature Review

This chapter reviews various methods for in-circuit impedance measurement. Generally, these methods can be classified into three: the voltage-current (V-I) measurement approach, the capacitive coupling, and the inductive coupling approaches. The basic instrumentation and principles of these three approaches will be elaborated, and their merits and drawbacks will be discussed.

2.1 Voltage-Current Measurement Approach

The V-I measurement approach is a straightforward way to determine the in-circuit impedance of an energized SUT through direct voltage and current measurements [42]. It can be realized by measuring the voltage and current due to an external excitation test signal [43] or by measuring any existing voltage and current harmonics in the SUT [44].

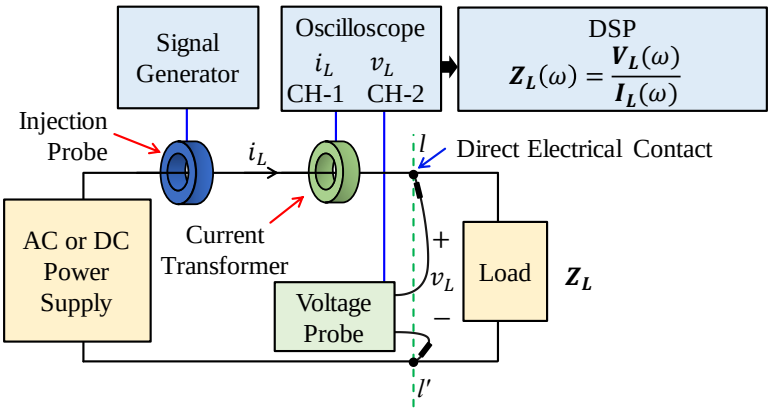

Fig. 2-1 A typical in-circuit impedance measurement setup using the V-I measurement approach with externally injected excitation signal.

Fig. 2-1 shows a SUT energized by an AC or DC power supply connected by cables. The signal generator provides an excitation of a known frequency ω through the injection probe.

The resultant terminal voltage v_L and current i_L of $\boldsymbol{Z_L}$ due to the excitation signal are sampled and digitized through an analog-to-digital converter (ADC) of an oscilloscope in the time domain. The subsequent DSP stage converts and processes the measured voltage and current in the frequency domain and computes $\boldsymbol{Z_L}$ in the frequency of interest ω using the following relationship [45].

$$\boldsymbol{Z_L}(\omega) = \frac{\boldsymbol{V_L}(\omega)}{\boldsymbol{I_L}(\omega)} \tag{2.1}$$

2.2 Capacitive Coupling Approach

Fig. 2-2 shows a typical setup that measures the in-circuit impedance of an energized SUT by an AC or DC power supply. The in-circuit impedance of the SUT to be extracted is denoted by $\boldsymbol{Z_L}$. The measurement instrument (VNA or IA) injects an excitation signal through a coupling capacitor C_1 and receives the response for the same signal through another coupling capacitor C_2 [46]. The values of these capacitors are chosen such that they provide isolation to the power frequencies (50 or 60 Hz) but essentially serve as a low impedance path for the high-frequency excitation signal. The roles of inductors L_1 and L_2 are to block the high-frequency excitation signal from coupling into the power supply so that the excitation signal only couples to the SUT to extract $\boldsymbol{Z_L}$.

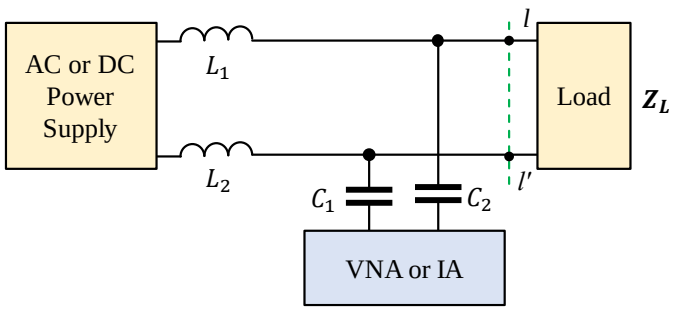

Fig. 2-2 Typical in-circuit impedance measurement setup based on capacitive coupling approach.

$$\boldsymbol{Z_m} = \frac{1}{j\omega C_1} + \frac{1}{j\omega C_2} + (j\omega L_1 + j\omega L_2 + \boldsymbol{Z_s})//\boldsymbol{Z_L} \tag{2.2}$$

where $\boldsymbol{Z_m}$ is the measured impedance by a VNA or an impedance analyzer (IA) and $\boldsymbol{Z_s}$ is the impedance of the power supply. ω is the frequency at which the impedance is evaluated. Since $(j\omega L_1 + j\omega L_2)$ is large and $(1/j\omega C_1 + 1/j\omega C_2)$ is small at high test frequencies, $\boldsymbol{Z_L}$ can be approximated by $\boldsymbol{Z_m}$.

$$\boldsymbol{Z_L} \approx \boldsymbol{Z_m} \tag{2.3}$$

Alternatively, the effects of the C_1 and C_2 can be de-embedded by using two known impedances to replace $\boldsymbol{Z_L}$ at *l-l′* for better measurement accuracy [19].

2.3 Inductive Coupling Approach

The inductive coupling approach was firstly proposed for the power line impedance measurement [47]. Subsequently, it was improved and employed to extract the in-circuit impedance of the SMPS for EMI filter design [48]. It was later improved with the two-port network theory-based interpretation [49]. Based on the application focus, the inductive coupling approach can be either set up as a TPS or as a multi-probe setup (MPS). The MPS has been developed for specific applications such as impedance measurement of systems with multibranch cables [50]. As opposed to the MPS, the TPS is for more general applications. The TPS can be implemented with FD-based instrumentation [51] and TD-based instrumentation [52]. Under this section, the inductive probe and the concept ofprobe,TPS for in-circuit impedance measurement are explained using two-port network theory.

2.3.1 Inductive Probe

Inductive probes are commonly used for current measurement and signal injection in the electromagnetic compatibility (EMC) testing field [41], [53], [54]. This section describes the basic principle and characteristics of an inductive probe.

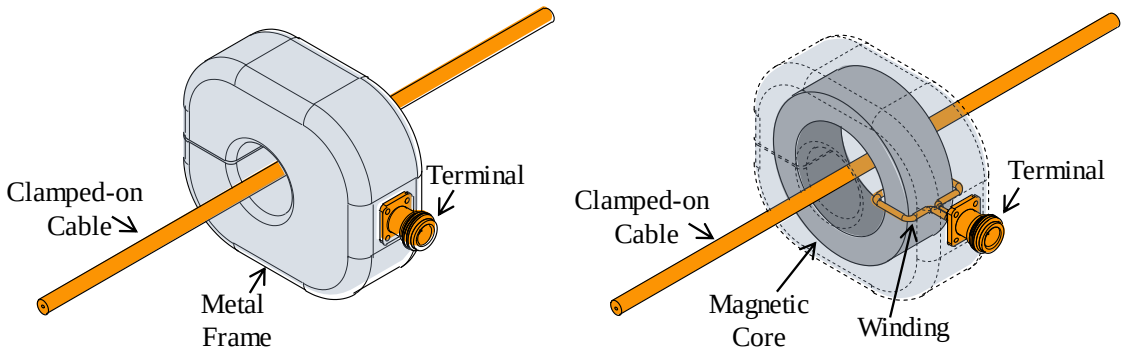

(a) (b)

Fig. 2-3 Illustration of an inductive probe clamped on to a cable (a) external view (b) internal view.

An inductive probe consists of a copper winding wound on a toroidal-shaped magnetic core covered by a metal frame as shown in Fig. 2-3. The core is usually split into two halves to allow easy installation by clamping onto a cable. The ends of the winding are interfaced to a radio frequency (RF) coaxial connector as an input or output. Fig. 2-4(a) and Fig. 2-4(b) show the actual photographs of a clamp-on type inductive probe (SOLAR 9144-1N) and its internals.

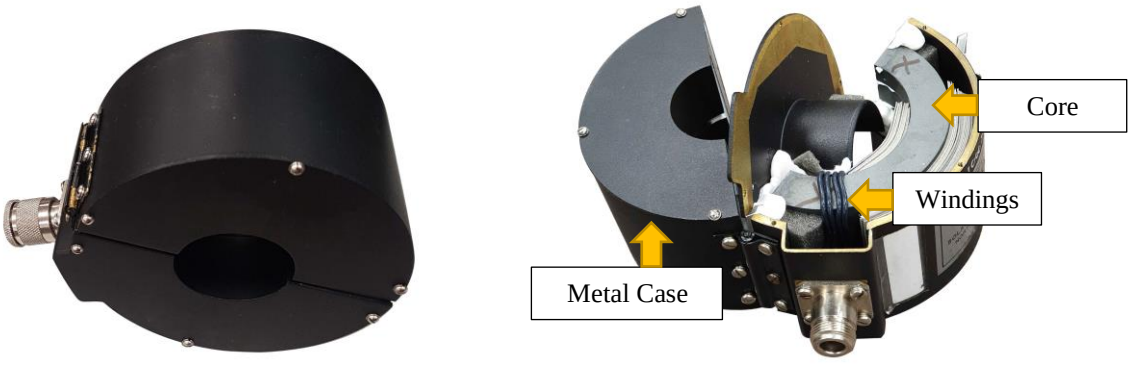

(a) (b)

Fig. 2-4 SOLAR 9144-1N inductive probe structure (a) externals (b) Internals.

For an inductive probe clamped onto a section of a cable labeled by *c*-*c′* as shown in Fig. 2-5(a), where the cable is part of a closed-loop of an electrical system, the equivalent circuit model of the probe is represented by Fig. 2-5(b). The inductive coupling between the probe and the clamped cable can be described through the magnetizing inductances (L_1 and L_2) and the mutual inductance M. L_{lk} and C_P represent leakage inductance and parasitic capacitance between the winding of the probe and its metal frame [55].

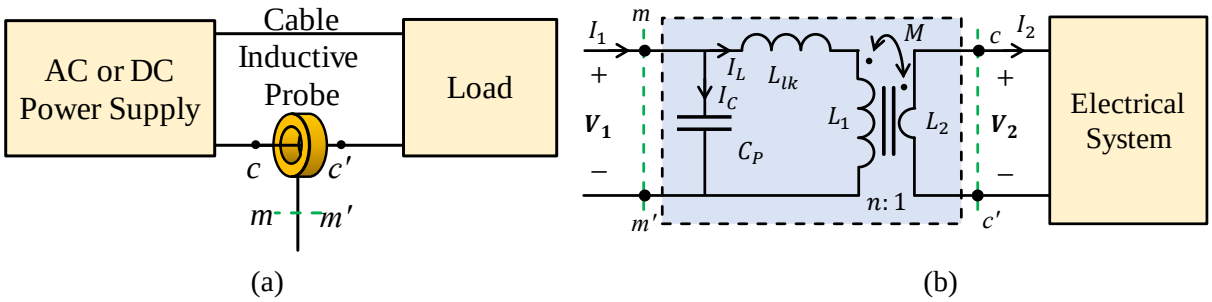

Fig. 2-5 Inductive probe clamped on to a wire of an electrical system (a) physical illustration (b) equivalent circuit model.

The equivalent circuit of Fig. 2-5(b) can be represented as a two-port network. Therefore, the resultant effects of the C_P, L_1, L_2, L_{lk}, and M can be represented by the equivalent transmission (*ABCD*) parameters as shown in Fig. 2-6 where *m*-*m′* and *l*-*l′* boundaries represent the two ports (Port 1 and Port 2) of the two-port network.

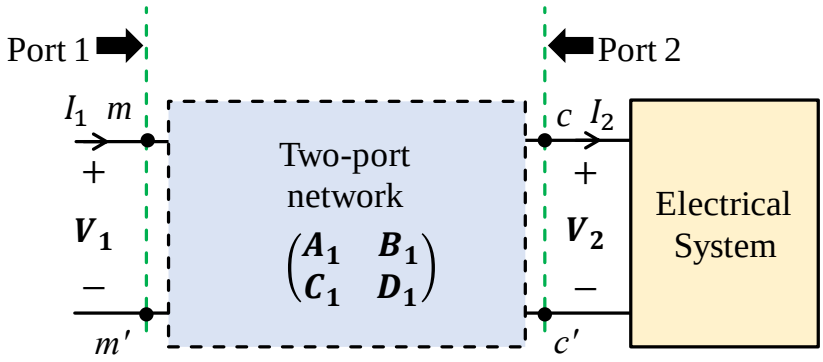

Fig. 2-6 The two-port network representation of an inductive probe clamped on to a wire of an electrical system.

The *ABCD* parameters that relate Ports 1 and 2 can be expressed in the following format [56].

$$\begin{pmatrix} \boldsymbol{V_1} \\ \boldsymbol{I_1} \end{pmatrix} = \begin{pmatrix} \boldsymbol{A_1} & \boldsymbol{B_1} \\ \boldsymbol{C_1} & \boldsymbol{D_1} \end{pmatrix} \begin{pmatrix} \boldsymbol{V_2} \\ \boldsymbol{I_2} \end{pmatrix} \tag{2.4}$$

Where the *ABCD* parameters are defined in terms of $\boldsymbol{V_1}$, $\boldsymbol{V_2}$, $\boldsymbol{I_1}$, and $\boldsymbol{I_2}$ as follows.

$$\boldsymbol{A_1} = \left(\frac{\boldsymbol{V_1}}{\boldsymbol{V_2}}\right)_{\boldsymbol{I_2}=0} \tag{2.5}$$

$$\boldsymbol{B_1} = \left(\frac{\boldsymbol{V_1}}{\boldsymbol{I_2}}\right)_{\boldsymbol{V_2}=0} \tag{2.6}$$

$$\boldsymbol{C_1} = \left(\frac{\boldsymbol{I_1}}{\boldsymbol{V_2}}\right)_{\boldsymbol{I_2}=0} \tag{2.7}$$

$$\boldsymbol{D_1} = \left(\frac{\boldsymbol{I_1}}{\boldsymbol{I_2}}\right)_{\boldsymbol{V_2}=0} \tag{2.8}$$

By circuit analysis, the frequency-dependant *ABCD* parameters relate to equivalent circuit parameters C_P, L_1, L_2, L_{lk}, and M as follows.

$$\begin{pmatrix} \boldsymbol{A_1} & \boldsymbol{B_1} \\ \boldsymbol{C_1} & \boldsymbol{D_1} \end{pmatrix} = \begin{pmatrix} \dfrac{L_1}{M} + \dfrac{L_{lk}}{M} & -Mj\omega + \dfrac{L_1 L_2}{M} j\omega + \dfrac{L_2 L_{lk}}{M} j\omega \\ -\dfrac{j}{M\,\omega} + \dfrac{C_P}{M}(L_1 + L_{lk}) j\omega & -\dfrac{C_P L_1 L_2 \omega^2}{M} + C_P M \omega^2 + \dfrac{L_2}{M} - \dfrac{C_P L_2 L_{lk} \omega^2}{M} \end{pmatrix} \tag{2.9}$$

where ω is the frequency at which the *ABCD* parameters are evaluated. It is worth noting that $\boldsymbol{A_1}$ is proportional to the turn-ratio and $\boldsymbol{D_1}$ is inversely proportional to the turns-ratio n as $L_1/M \propto n$ and $L_2/M \propto 1/n$. Using a two-port VNA, the *ABCD* parameters of a two-port network can be experimentally obtained. Since the VNA measurements are usually represented in *S*-parameter format, firstly the *S*-parameters of the two-port network should be measured as $\boldsymbol{S_{11}}$, $\boldsymbol{S_{12}}$, $\boldsymbol{S_{21}}$ and $\boldsymbol{S_{22}}$ and converted into *ABCD* parameters using the following conversion formulae.

$$\boldsymbol{A_1} = \frac{(1 + \boldsymbol{S_{11}})(1 - \boldsymbol{S_{22}}) + \boldsymbol{S_{12}}\boldsymbol{S_{21}}}{2\boldsymbol{S_{21}}} \tag{2.10}$$

$$\boldsymbol{B_1} = \boldsymbol{Z_0}\frac{(1 + \boldsymbol{S_{11}})(1 + \boldsymbol{S_{22}}) - \boldsymbol{S_{12}}\boldsymbol{S_{21}}}{2\boldsymbol{S_{21}}} \tag{2.11}$$

$$\boldsymbol{C_1} = \frac{1}{\boldsymbol{Z_0}} \frac{(1-\boldsymbol{S_{11}})(1-\boldsymbol{S_{22}}) - \boldsymbol{S_{12}}\boldsymbol{S_{21}}}{2\boldsymbol{S_{21}}} \tag{2.12}$$

$$\boldsymbol{D_1} = \frac{(1-\boldsymbol{S_{11}})(1+\boldsymbol{S_{22}}) + \boldsymbol{S_{12}}\boldsymbol{S_{21}}}{2\boldsymbol{S_{21}}} \tag{2.13}$$

where $\boldsymbol{Z_0}$ is the reference impedance of the VNA *S*-parameter measurement.

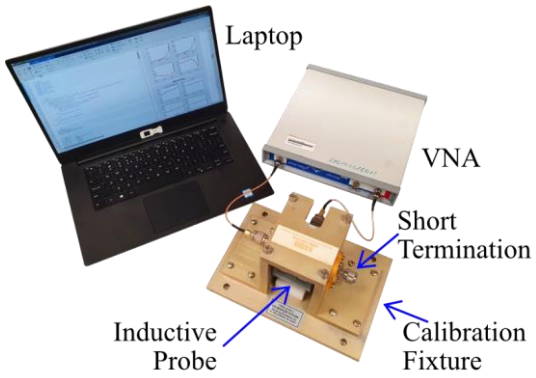

Fig. 2-7 Inductive probe characterization using a two-port VNA and a calibration fixture.

In order to measure the *S*-parameters of an inductive probe, a suitable calibration fixture should be used [57]. Fig. 2-7 shows an example of an inductive probe being measured for *S*-parameters using a two-port VNA and a coaxial type calibration fixture, where the probe (FCC F-120-6A-3) is clamped onto the inner conductor and surrounded by the outer conductor of the calibration fixture (Solar 9124-1). The inductive probe terminal is connected to port 1 of the VNA. One end of the calibration fixture is terminated by a short termination and the other end is terminated by port 2 of the VNA.

Fig. 2-8 shows an equivalent network representation of inductive probe characterization using a calibration fixture. With two frequency sweep excitations from the two ports respectively, the two-port *S*-parameters are measured in two steps. When the Port 1 of the VNA is the signal source, $\boldsymbol{S_{11}}$ and $\boldsymbol{S_{21}}$ are measured. When the Port 1 of the VNA is the signal source, $\boldsymbol{S_{22}}$ and $\boldsymbol{S_{12}}$ are measured. Then, the *ABCD* parameters are derived by using the conversion formulae of (2.10)-(2.13).

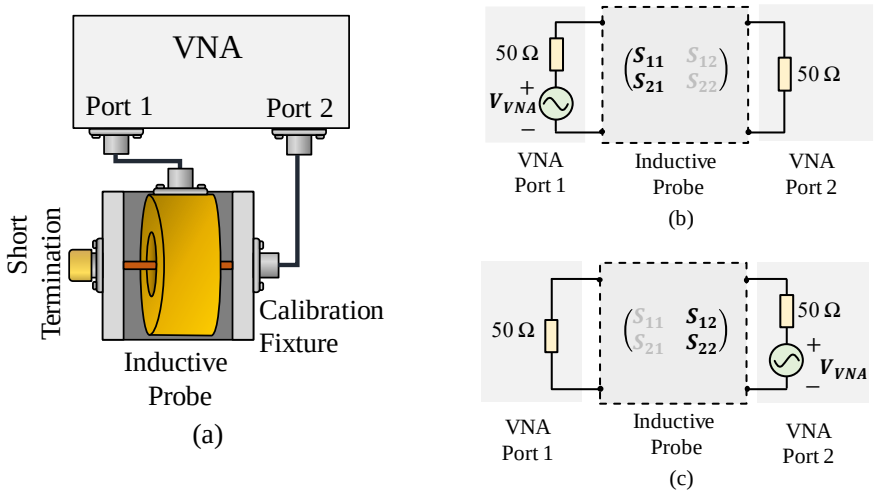

Fig. 2-8 inductive probe characterization of the (a) physical connection (b) Port 1 as the (c) Port 2 as the excitation source.

As an illustration, Fig. 2-9 and Fig. 2-10 show the magnitude and phase information of the two-port *ABCD* parameters from 150 kHz to 30 MHz obtained for the inductive probe the probe (FCC F-120-6A-3) using the setup shown in Fig. 2-7. It is observed that $\boldsymbol{A_1} \approx 1$ and $\boldsymbol{D_1} \approx 1$ at low frequencies because the turns-ratio $n = 1$ according to the manufacturer. But they deviate from unity when the coupling to the wire becomes non-ideal due to leakage flux. For the same reason, $\boldsymbol{B_1}$ has a non-zero value as frequency increases and $\boldsymbol{C_1}$ becomes smaller in accordance with (2.9) as L_{lk} and C_P are small parasitic elements. The measured *ABCD* parameters of inductive probes are required for impedance measurement with the TPS.

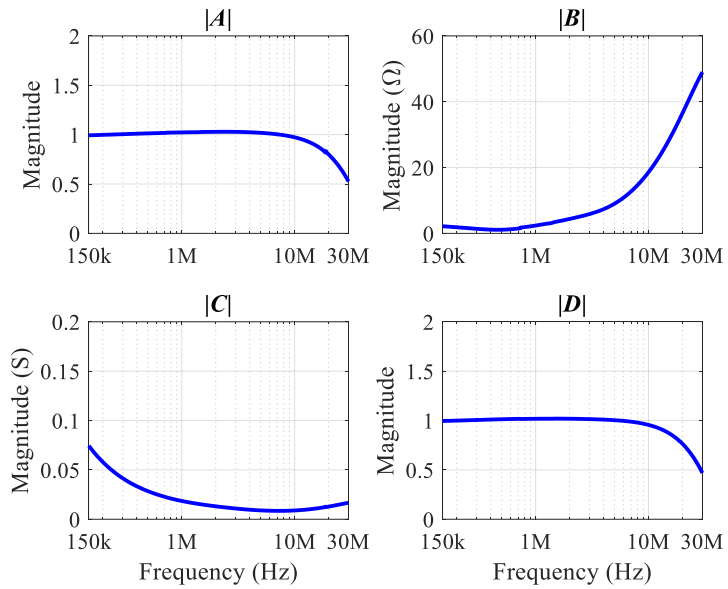

Fig. 2-9 Measured two-port ABCD parameters of the inductive probe (magnitude).

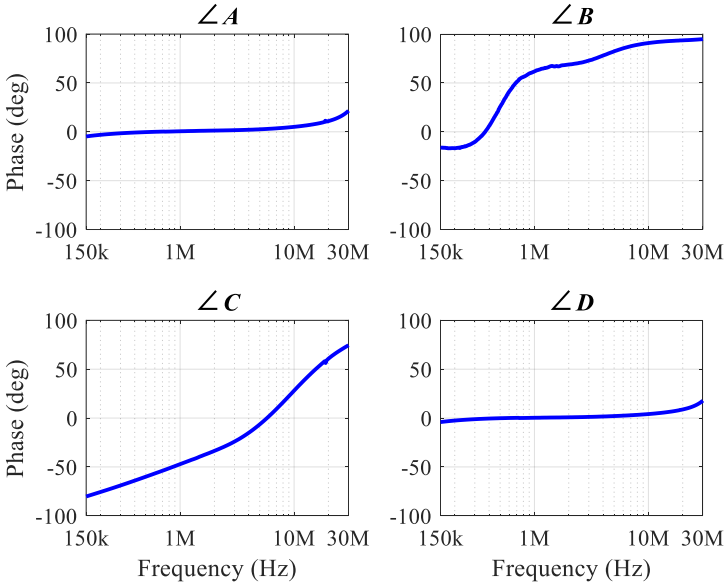

Fig. 2-10 Measured two-port ABCD parameters of the inductive probe (phase).

2.3.2 Two-Probe In-Circuit Impedance Measurement Setup

In this section, the TPS for in-circuit impedance measurement is explained under two possible implementations based on the type of instrumentation used. The first implementation uses a VNA which is FD-based instrumentation [58]. and the second implementation utilizes TD-based instrumentation [52].

2.3.2.1 TPS with Frequency-Domain Based Instrumentation

Fig. 2-11 shows a load powered by either an AC or a DC power supply $\boldsymbol{V_S}$ with an internal impedance $\boldsymbol{Z_S}$. $\boldsymbol{Z_W}$ is the equivalent impedance of the cable connection between the power supply and the load. $\boldsymbol{Z_L}$ is the equivalent impedance of the load. The power supply and the load with the cable connection are regarded as the SUT. $\boldsymbol{Z_X}$ is the equivalent impedance of the SUT and is equal to the resultant series impedance of $\boldsymbol{Z_L}$, $\boldsymbol{Z_W}$, and $\boldsymbol{Z_S}$ [51]. The two inductive probes are clamped onto a section of the cable connection. A two-port VNA is terminated by the two inductive probes. The two-port network representation of the setup is shown in Fig. 2-12 when the Port 1 of the VNA is the excitation signal source. The inductive probes and the SUT have been represented by their respective *ABCD* parameters. $\boldsymbol{N_1}$, $\boldsymbol{N_2}$, and $\boldsymbol{N_{SUT}}$ are the two-port networks of the inductive probe 1, probe 2, and SUT respectiSUT,y. $\boldsymbol{N_{SYS}}$ is the cascaded two port network of $\boldsymbol{N_1}$, $\boldsymbol{N_2}$, and $\boldsymbol{N_{SUT}}$.

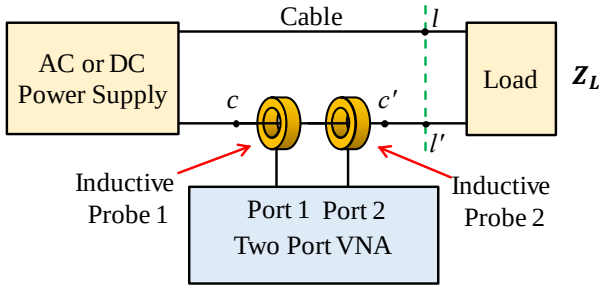

Fig. 2-11 TPS for in-circuit impedance measurement using FD-based instrumentation.

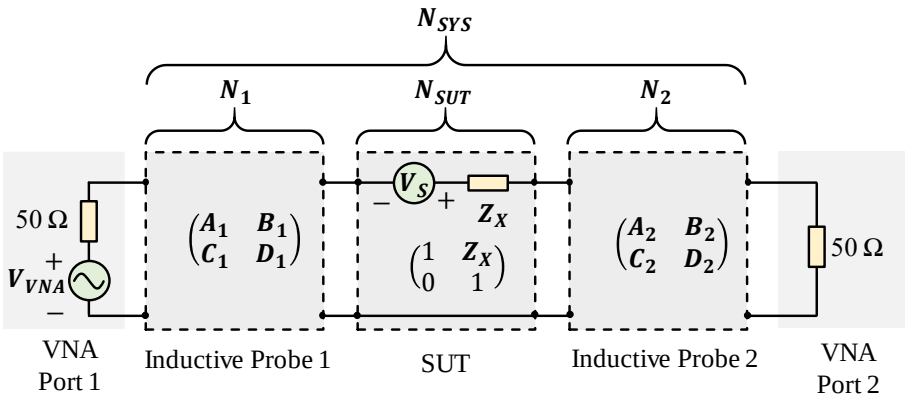

Fig. 2-12 Cascaded two-port network representation of the TPS with FD-based instrumentation.

To measure the in-circuit impedance $\boldsymbol{Z_X}$ through the TPS, firstl, the *ABCD* parameters of two-port networks $\boldsymbol{N_1}$ and $\boldsymbol{N_2}$ can be known by inductive probe characterization, as described in subsection 2.3.1. Second, using Port 1 of VNA as the sweep frequency excitation source, $\boldsymbol{S_{11}}$ and $\boldsymbol{S_{21}}$ of $\boldsymbol{N_{SYS}}$ are measured. Third, using Port 2 of VNA as the sweep frequency excitation source, $\boldsymbol{S_{22}}$ and $\boldsymbol{S_{12}}$ of $\boldsymbol{N_{SYS}}$ are measured. The measured *S*-parameters of the two-port network $\boldsymbol{N_{SYS}}$ are converted to the *ABCD* parameters.

The *ABCD* parameters of the two-port network $\boldsymbol{N_{SUT}}$ can be obtained by solving the following equation as $\boldsymbol{N_{SYS}}$ is the cascaded combination of $\boldsymbol{N_1}$, $\boldsymbol{N_2}$, and $\boldsymbol{N_{SUT}}$.

$$\begin{pmatrix} 1 & \boldsymbol{Z_X} \\ 0 & 1 \end{pmatrix} = \begin{pmatrix} \boldsymbol{A_1} & \boldsymbol{B_1} \\ \boldsymbol{C_1} & \boldsymbol{D_1} \end{pmatrix}^{-1} \begin{pmatrix} \boldsymbol{A_{SYS}} & \boldsymbol{B_{SYS}} \\ \boldsymbol{C_{SYS}} & \boldsymbol{D_{SYS}} \end{pmatrix} \begin{pmatrix} \boldsymbol{A_2} & \boldsymbol{B_2} \\ \boldsymbol{C_2} & \boldsymbol{D_2} \end{pmatrix}^{-1} \tag{2.14}$$

Finally, the unknown impedance $\boldsymbol{Z_X}$ can be extracted as follows.

$$\boldsymbol{Z_X} = \frac{\boldsymbol{A_2(D_1B_{SYS} - B_1D_{SYS}) + B_2(B_1C_{SYS} - D_1A_{SYS})}}{\boldsymbol{(A_1D_1 - B_1C_1)(A_2D_2 - B_2C_2)}} \tag{2.15}$$

In the cases where the load's in-circuit impedance $\boldsymbol{Z_L}$ needs to be extracted, $(\boldsymbol{Z_S + Z_W})$ can be de-embedded from $\boldsymbol{Z_X}$ [35]. To perform the de-embedding, a known impedance $\boldsymbol{Z_{known}}$ is used to replace the unknown $\boldsymbol{Z_L}$. The respectively obtained $\boldsymbol{Z_X}$ is denoted by $\boldsymbol{Z'_X}$. Then the unknown $\boldsymbol{Z_L}$ can be calculated with respect to $\boldsymbol{Z_X}$, $\boldsymbol{Z'_X}$, and $\boldsymbol{Z_{known}}$ as follows.

$$\boldsymbol{Z_L = Z_X - Z'_X + Z_{known}} \tag{2.16}$$

2.3.2.2 TPS with Time-Domain Based Instrumentation

Fig. 2-13 shows a load powered by either an AC or a DC power supply $\boldsymbol{V_S}$ with an internal impedance $\boldsymbol{Z_S}$. $\boldsymbol{Z_W}$ is the equivalent impedance of the cable connection between the power supply and the load. $\boldsymbol{Z_L}$ is the equivalent impedance of the load. The power supply and the load with the cable connection are regarded as the SUT. $\boldsymbol{Z_X}$ is the equivalent impedance of the SUT and is equal to the resultant series impedance of $\boldsymbol{Z_L}$, $\boldsymbol{Z_W}$, and $\boldsymbol{Z_S}$ [34]. The two inductive

probes are clamped onto a section of the wire connecting to the load. A SGAS with TD-based instruments provides the excitation and measures the response. The arbitrary waveform generator (AWG) of the SGAS is connected to the inductive probe 1 and channel 1 (CH 1) of the analog to digital converter (ADC) of the SGAS. Inductive probe 2 is terminated by channel 2 (CH 2) of ADC with 50 Ω resistive termination impedance.

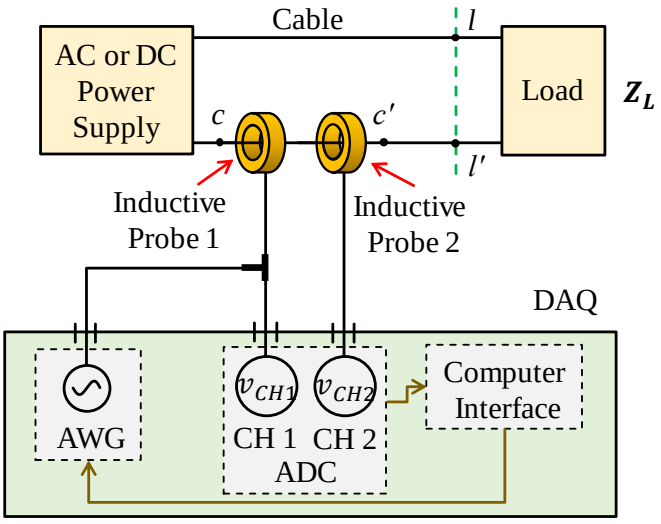

Fig. 2-13 TPS for in-circuit impedance measurement using TD-based instrumentation.

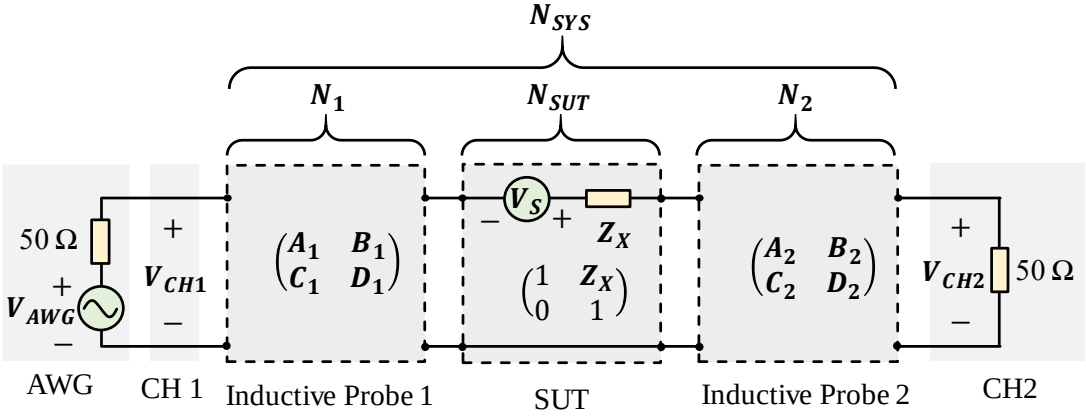

Fig. 2-14 Cascaded two-port network representation of the TPS for in-circuit impedance measurement using TD-based instrumentation.

By computer control, AWG provides an excitation signal with a known frequency ω to the SUT through the inductive probe 1. The time-domain terminal voltage of the inductive probes 1 and 2 (v_{CH1} and v_{CH2}) are digitized and recorded by the two ADC channels of the SGAS.

By discrete Fourier transform (DFT), the frequency-domain counterparts of the v_{CH1} and v_{CH2} are obtained at the frequency ω as $\boldsymbol{V_{CH1}}$ and $\boldsymbol{V_{CH2}}$ The cascaded two-port network representation of the setup based on $\boldsymbol{V_{CH1}}$ and $\boldsymbol{V_{CH2}}$ is given in Fig. 2-14. The inductive probes and the SUT are represented by their respective two-port *ABCD* parameters. $\boldsymbol{N_1}$, $\boldsymbol{N_2}$, and $\boldsymbol{N_{SUT}}$ are the two-port network of the inductive probe 1, probe 2, and SUT. $\boldsymbol{N_{SYS}}$ is the cascaded two-port network $\boldsymbol{N_1}$, $\boldsymbol{N_2}$, and $\boldsymbol{N_{SUT}}$, To measure the in-circuit impedance $\boldsymbol{Z_X}$ through the TPS, firstly, The *ABCD* parameters of the two-port networks $\boldsymbol{N_1}$ and $\boldsymbol{N_2}$ can be known by inductive probe characterization as described in subsection 2.3.1. Secondly, the system is excited by the AWG. Then $\boldsymbol{V_{CH1}}$ and $\boldsymbol{V_{CH2}}$ are obtained from v_{CH1} and v_{CH2} using DSP. Finally, the unknown impedance $\boldsymbol{Z_X}$ can be extracted as follows [35].

$$\boldsymbol{Z_X} = \frac{\boldsymbol{V_{CH1}}}{\boldsymbol{V_{CH2}}} \cdot \frac{1}{\boldsymbol{A_1}\left(\boldsymbol{C_2} - \frac{1}{50}\boldsymbol{D_2}\right)} - \frac{\boldsymbol{A_2} + \frac{\boldsymbol{B_2}}{50}}{\left(\boldsymbol{C_2} - \frac{1}{50}\boldsymbol{D_2}\right)} - \frac{\boldsymbol{B_1}}{\boldsymbol{A_1}} \tag{2.17}$$

In the cases where the in-circuit impedance $\boldsymbol{Z_L}$ needs to be extracted, $(\boldsymbol{Z_S} + \boldsymbol{Z_W})$ can be de-embedded from $\boldsymbol{Z_X}$ [35]. To perform the de-embedding, a known impedance $\boldsymbol{Z_{known}}$ is used to replace the unknown $\boldsymbol{Z_L}$. The respectively obtained $\boldsymbol{Z_X}$ is denoted by $\boldsymbol{Z_X'}$. Then the unknown $\boldsymbol{Z_L}$ can be calculated with respect to $\boldsymbol{Z_X}$, $\boldsymbol{Z_X'}$, and $\boldsymbol{Z_{known}}$ as follows.

$$\boldsymbol{Z_L} = \boldsymbol{Z_X} - \boldsymbol{Z_X'} + \boldsymbol{Z_{known}} \tag{2.18}$$

2.4 Summary and Discussion

This chapter provides an overview of three prevalent in-circuit impedance measurement approaches; the voltage-current (V-I) measurement approach, the capacitive coupling approach, and the inductive coupling approach. Both the V-I measurement approach and the capacitive coupling approach require the measurement instruments to have direct electrical

contact to the energized SUT due to the needs of the voltage sensor and the coupling capacitors, respectively. Such direct electrical contact can cause electrical safety hazard to the service personnel who conducts the on-site implementation. In addition, SUT energized at high voltage and power levels can cause high dielectric and thermal stress to the voltage sensor and the coupling capacitors, which may require regular maintenance and replacement and results in unnecessary interruption of the SUT's operation. In contrast to these two approaches, the inductive coupling approach does not require any direct contact to the energized SUT. The clamp-on type inductive probes can be quickly attached and detached from the insulated power cables of the SUT, which greatly simplifies the on-site setup and implementation. Even though the TPS based on the inductive coupling approach has been well-established and has shown its advantages for in-circuit impedance measurement, there are still some limitations to be overcome and will be discussed in the subsequent sections.

2.4.1 Limitation Related to Probe Characterization

As explained in the earlier section, the inductive probes must be characterized prior to the in-circuit impedance measurement using a TPS. This section elaborates on the errors caused by the calibration fixture in the measurement of the two-port *ABCD* parameters of the inductive probes.

Fig. 2-15 shows the measured impedance obtained from the TPS. The setup consists of a two-port VNA (Bode 100, 1 Hz – 40 MHz, an injecting inductive probe (Solar 9144-1N, 4 kHz - 100 MHz), and a receiving inductive probe (Solar 9134-1, 20 Hz - 100 MHz). The inductive probes have been characterized using the Solar 9125-1 (20 Hz to 500 MHz) calibration fixture. The actual TPS and a load $\boldsymbol{Z_L}$ are shown in Fig. 2-16. Three passive components are selected as the load (1 nF capacitor, 100 Ω resistor, and 10 Ω resistor). The

reference impedance is obtained by offline direct impedance measurement using an impedance analyzer (IA) (Bode 100 configured as an IA).

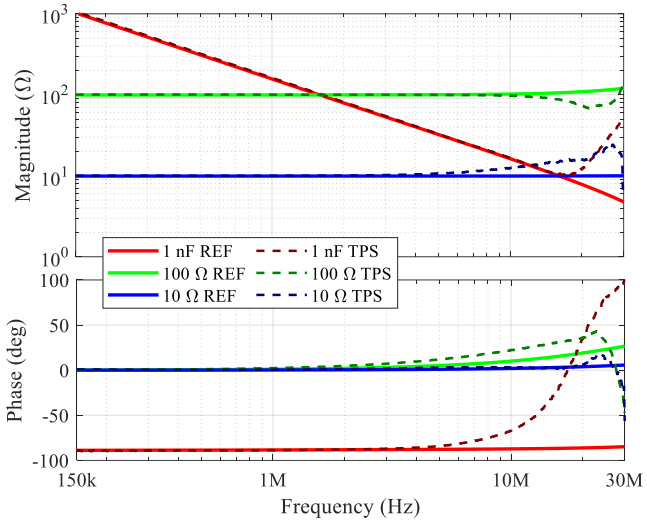

Fig. 2-15 Comparison of in-circuit impedance extracted from the TPS with the reference impedance (REF).

From Fig. 2-15, it is clearly observed that the agreement between the measured and the reference impedances is rather poor as frequency increases, especially above 10 MHz. The measurement discrepancy is largely due to the non-ideal behaviors of the calibration fixture, which will be discussed in the following section [59].

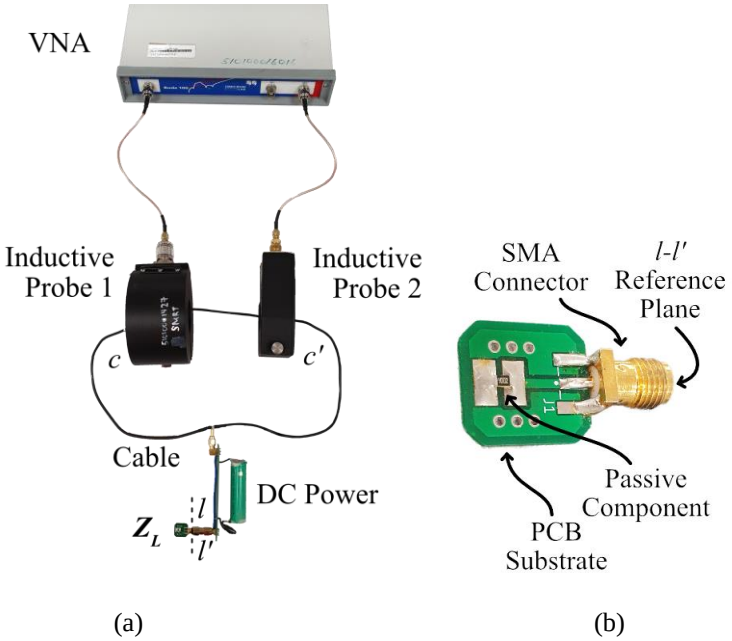

Fig. 2-16 Measurement of $\boldsymbol{Z_L}$ (a) with TPS (b) with impedance analyzer.

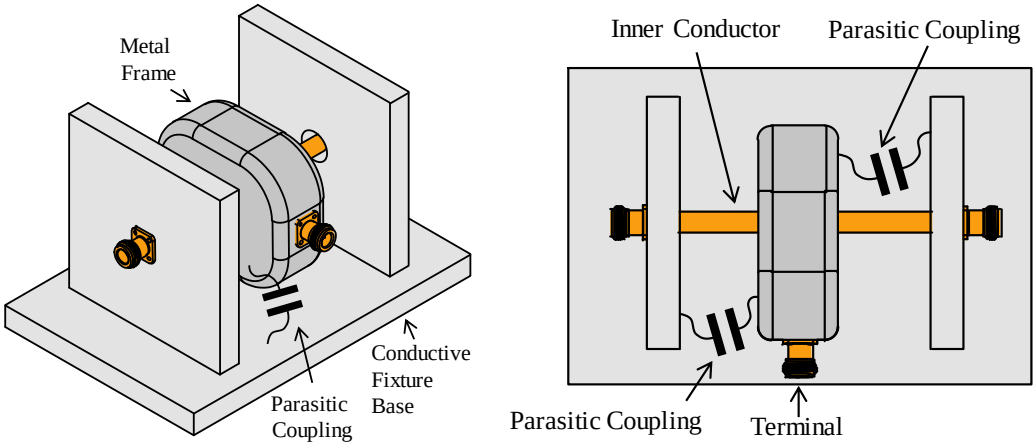

Fig. 2-17 Non-ideal behaviors of the calibration fixture.

These non-ideal behaviors of the calibration fixture are illustrated in Fig. 2-17, where the presence of parasitic capacitance between the frame of the inductive probe and the calibration fixture is highlighted. Another no-ideal effect comes from the equivalent series inductance (ESL) of the calibration fixture. It is to take note that the calibration fixture cannot fully resemble the true TPS in a specific application due to different conductor diameters, and therefore it can lead to measurement discrepancy in the TPS, especially at higher frequencies.

2.4.2 Probe-to-Probe Coupling in TPS

As observed in Fig. 2-16, it is not always possible to maintain a large physical separation between the two inductive probes. Once they are placed closer to each other, undesirable probe-to-probe coupling can compromise the measurement accuracy. This coupling occurs because part of the leaked magnetic flux from one inductive probe directly couples to the winding of the other probe. Due to the clamp-on type design of the inductive probe, a split-magnetic core is adopted, and it is prone to magnetic flux leakage, especially when the split gaps of both probes are aligned. If the probe-to-probe coupling is not well-taken care of in the measurement setup, significant errors in the impedance measurement can occur [39].

Fig. 2-18 shows the TPS with the gap between two probes indicated as d. To illustrate how the probe-to-probe coupling affects the measurement accuracy, the in-circuit impedance measurement of a DC-powered $\boldsymbol{Z_L}$ is carried out. The details of the instruments and circuit components are listed in Table 2-1.

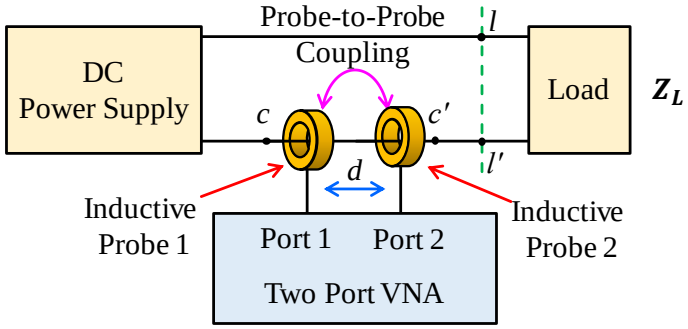

Fig. 2-18 Probe-to-probe coupling of TPS.

Table 2-1. Details of Instruments and Loads for the TPS.

Instrument	Model	Component	Description
VNA	Bode 100 (5Hz – 40 MHz)	$\boldsymbol{Z_L}$	5 kΩ Resistor (1%)
Probe 1	SOLAR 9144-1N (4kHz – 100 MHz)	DC Power Supply	3.7 V 18650 Lithium Battery
Probe 2	SOLAR 9134-1 (20 Hz – 100 MHz)	Wires	16 AWG 80 cm

Fig. 2-19 shows the comparison of the measured $\boldsymbol{Z_L}$ using TPS for $d = 0$ cm and $d = 10$ cm. $\boldsymbol{Z_L}$ is also measured off-circuit by an IA (Bode 100 configured as an IA) as a reference. The comparison shows that the measured in-circuit impedance with $d = 0$ cm deviates significantly due to the strong probe-to-probe coupling. When d increases to 10 cm, the measured in-circuit impedance resembles the reference measurement. Therefore, the probe-to-probe coupling becomes negligible and can be ignored. A comprehensive analysis of the impact of the probe-to-probe coupling has been reported and will not be repeated here [39].

Although an error correction method has been developed to compensate for the error the process can be tedious and cumbersome [40].

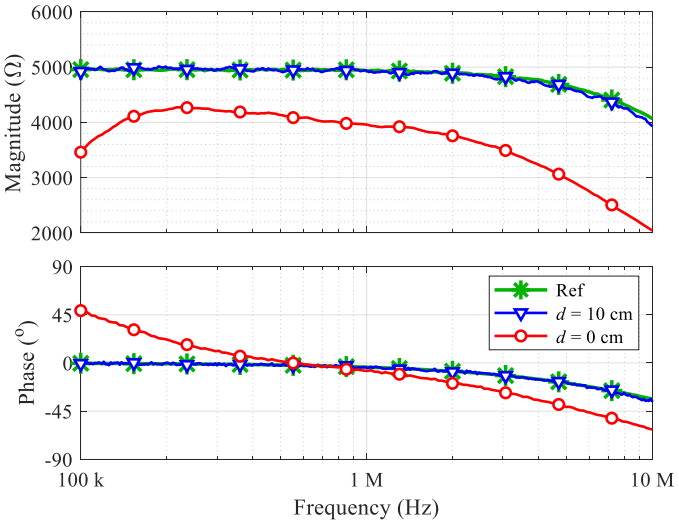

Fig. 2-19. Impact of the probe-to-probe coupling on the measurement accuracy of the TPS.

2.5 Concluding Remarks

In this chapter, three existing in-circuit measurement approaches have been reviewed. Since the V-I measurement approach and the capacitive coupling approach require a direct electrical contact to the energized SUT, the inductive coupling approach is an attractive choice for in-circuit impedance measurement. TPS with FD-based instrumentation has been briefly described and its shortcomings have also been elaborated. To overcome these shortcomings, the SPS of the inductive coupling approach with both FD and TD-based instrumentations will be discussed in the subsequent chapters.

Chapter 3 Single-Probe In-Circuit Impedance Extraction with Frequency-Domain Based Instrumentation

This chapter focuses on the principle and implementation of SPS with FD-based instrumentation for in-circuit impedance measurement. A comprehensive investigation of the SPS is performed to show that the systematic error that occurred in the TPS will be canceled in the SPS. The validity of the SPS with FD-based instrumentation will be demonstrated experimentally.

3.1 Principle of the Single-Probe Setup

Fig. 3-1 shows the proposed SPS for in-circuit impedance measurement of an energized SUT. The SUT has a load powered by an AC or DC power supply through connecting cables. The measurement plane at the load is denoted by *l*-*l′*. An inductive probe is clamped onto one of the power cables at a clamping location marked by *c*-*c′*. The inductive probe is connected to an impedance measurement instrument, where the measurement reference plane is labeled as *m*-*m′*.

The objective of the proposed SPS is to extract the in-circuit SUT impedance seen at *c*-*c′* or at *l*-*l′* (if the load termination is accessible). By establishing a relationship between *m*-*m′* and *c*-*c′*, the SUT impedance can be determined. Similarly, by establishing the relationship between *m*-*m′* and *l*-*l′*, the load impedance can also be extracted.

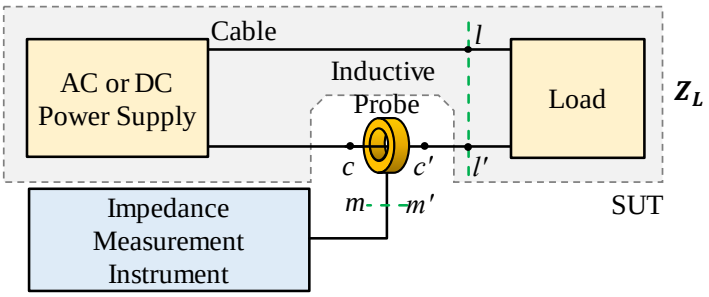

Fig. 3-1 Basic SPS for in-circuit impedance measurement.

The equivalent circuit of the SPS is given in Fig. 3-2. The power supply of the energized SUT is represented by its equivalent Thevenin voltage $\boldsymbol{V_s}$ and impedance $\boldsymbol{Z_s}$. The load is represented by its impedance $\boldsymbol{Z_L}$. In the maximum frequency range of interest (30 MHz), the length of the power cables is much shorter than the wavelength of the highest signal frequency and therefore can be represented by a lumped series and shunt impedances $\boldsymbol{Z_{W1}}$ and $\boldsymbol{Z_{W2}}$, which include the non-ideal parasitic effects of the cables, especially above 10 MHz.

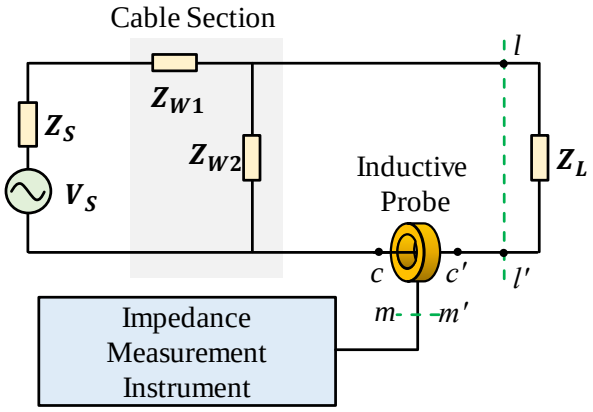

Fig. 3-2. Equivalent circuit of the SPS.

The setup can also be expressed as two cascaded two-port networks, as shown in Fig. 3-3. The two-port networks in the setup are denoted by their respective *ABCD* parameters. The cable and the power supply are combined and treated as one two-port network. The impedance seen by the measurement instrument is denoted by $\boldsymbol{Z_m}$. Similarly, the impedance seen by the

inductive probe at *c*-*c′* is denoted by $\boldsymbol{Z_c}$. The impedance measurement instrument can be an IA or a VNA, which will be discussed in the following sections.

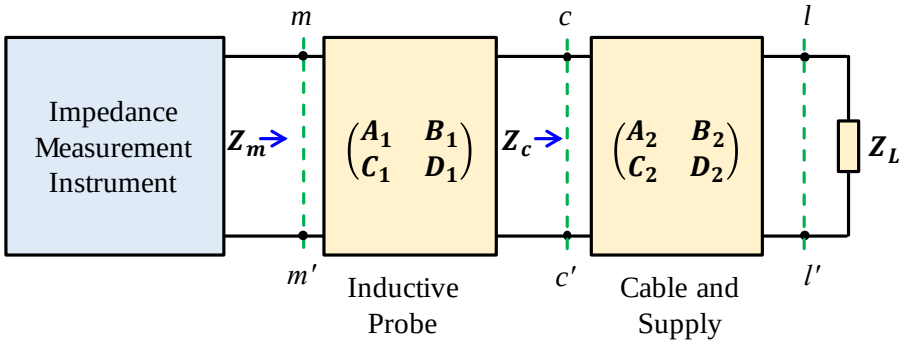

Fig. 3-3. Cascaded two-port network representation of the SPS.

3.2 Impedance Analyzer as Measurement Instrument

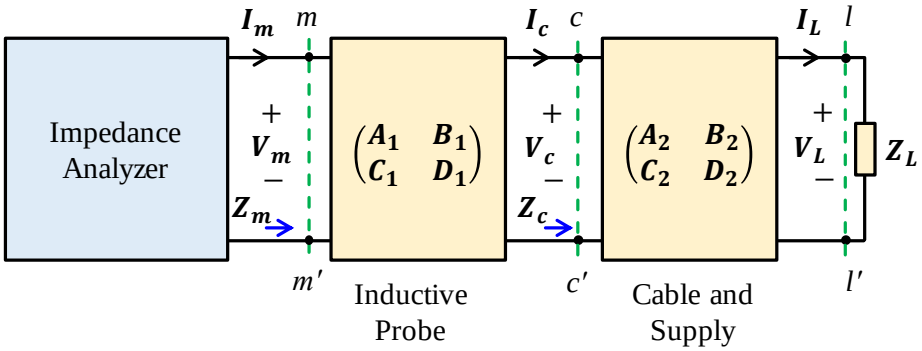

Fig. 3-4. In-circuit impedance measurement using SPS with IA as the measurement instrument

Fig. 3-4 shows the SPS with an IA as the impedance measurement instrument. The voltage and current due to the excitation provided by the IA at *m*-*m′* are given as $\boldsymbol{V_m}$ and $\boldsymbol{I_m}$, respectively. The resultant voltage and current at *c*-*c′* are given as $\boldsymbol{V_c}$ and $\boldsymbol{I_c}$, respectively. The resultant voltage and current at *l*-*l′* are given as $\boldsymbol{V_L}$ and $\boldsymbol{I_L}$, respectively. The impedance seen by the IA is $\boldsymbol{Z_m}$. Through network analysis, *m*-*m′* is related to *c*-*c′* by:

$$\boldsymbol{Z_m = \frac{V_m}{I_m} = \frac{A_1 V_c + B_1 I_c}{C_1 V_c + D_1 I_c}} \tag{3.1}$$

Since $\boldsymbol{Z_c = V_c / I_c}$, (3.1) can be expressed as:

$$\boldsymbol{Z_m = \frac{A_1 Z_c + B_1}{C_1 Z_c + D_1}} \tag{3.2}$$

This can be rearranged to:

$$\boldsymbol{Z_c = \frac{k_1 Z_m + k_2}{Z_m + k_3}} \tag{3.3}$$

where

$$\boldsymbol{k_1 = -D_1 / C_1} \tag{3.4}$$

$$\boldsymbol{k_2 = B_1 / C_1} \tag{3.5}$$

$$\boldsymbol{k_3 = -A_1 / C_1} \tag{3.6}$$

Once $\boldsymbol{k_1}$, $\boldsymbol{k_2}$, and $\boldsymbol{k_3}$ are known, $\boldsymbol{Z_c}$ can be determined using (3.3) based on the measured $\boldsymbol{Z_m}$. Note that $\boldsymbol{k_1}$, $\boldsymbol{k_2}$, and $\boldsymbol{k_3}$ are dependent on the two-port *ABCD* parameters of the inductive probe. To determine $\boldsymbol{k_1}$, $\boldsymbol{k_2}$, and $\boldsymbol{k_3}$ a pre-measurement characterization of the SPS must be performed by removing the energized SUT from *c*-*c′* and replacing it with three known distinct impedances, $\boldsymbol{Z_1}$, $\boldsymbol{Z_2}$ and $\boldsymbol{Z_3}$, where $\boldsymbol{Z_1 \neq Z_2 \neq Z_3}$. The off-circuit pre-measurement characterization of the SPS is shown in Fig. 3-5.

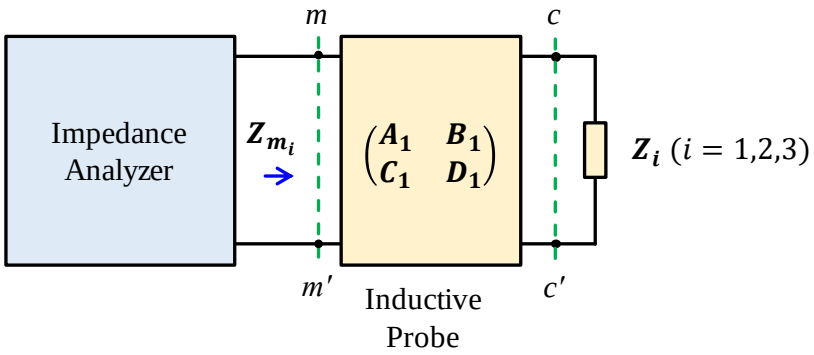

Fig. 3-5. Pre-measurement characterization at *c*-*c′*.

By substituting $\boldsymbol{Z_1}$, $\boldsymbol{Z_2}$, and $\boldsymbol{Z_3}$ into (3.3):

$$\boldsymbol{Z_1 = \frac{k_1 Z_{m_1} + k_2}{Z_{m_1} + k_3}} \tag{3.7}$$

$$\boldsymbol{Z_2 = \frac{k_1 Z_{m_2} + k_2}{Z_{m_2} + k_3}} \tag{3.8}$$

$$\boldsymbol{Z_3 = \frac{k_1 Z_{m_3} + k_2}{Z_{m_3} + k_3}} \tag{3.9}$$

where $\boldsymbol{Z_{m_1}}$, $\boldsymbol{Z_{m_2}}$, and $\boldsymbol{Z_{m_3}}$ are the impedances measured by the IA at *m*-*m′* for $\boldsymbol{Z_1}$, $\boldsymbol{Z_2}$ and $\boldsymbol{Z_3}$, respectively. Combining (3.3), (3.7), and (3.8) leads to:

$$\boldsymbol{\left(\frac{Z_c - Z_1}{Z_1 - Z_2}\right) = \left(\frac{\frac{k_1 Z_m + k_2}{Z_m + k_3} - \frac{k_1 Z_{m_1} + k_2}{Z_{m_1} + k_3}}{\frac{k_1 Z_{m_1} + k_2}{Z_{m_1} + k_3} - \frac{k_1 Z_{m_2} + k_2}{Z_{m_2} + k_3}}\right)} \tag{3.10}$$

Similarly, combining (3.3), (3.8), and (3.9) leads to:

$$\boldsymbol{\left(\frac{Z_2 - Z_3}{Z_3 - Z_c}\right) = \left(\frac{\frac{k_1 Z_{m_2} + k_2}{Z_{m_2} + k_3} - \frac{k_1 Z_{m_3} + k_2}{Z_{m_3} + k_3}}{\frac{k_1 Z_{m_3} + k_2}{Z_{m_3} + k_3} - \frac{k_1 Z_m + k_2}{Z_m + k_3}}\right)} \tag{3.11}$$

By multiplying (3.10) and (3.11):

$$\boldsymbol{Z_c = \frac{a + bZ_m}{c + dZ_m}} \tag{3.12}$$

where

$$\boldsymbol{a = Z_1 Z_2 (Z_{m_2} - Z_{m_1}) Z_{m_3} + Z_1 Z_3 (Z_{m_1} - Z_{m_3}) Z_{m_2} + Z_2 Z_3 (Z_{m_3} - Z_{m_2}) Z_{m_1}} \tag{3.13}$$

$$\boldsymbol{b = Z_1 Z_2 (Z_{m_1} - Z_{m_2}) + Z_1 Z_3 (Z_{m_3} - Z_{m_1}) + Z_2 Z_3 (Z_{m_2} - Z_{m_3})} \tag{3.14}$$

$$\boldsymbol{c = Z_1 (Z_{m_2} - Z_{m_3}) Z_{m_1} + Z_2 (Z_{m_3} - Z_{m_1}) Z_{m_2} + Z_3 (Z_{m_1} - Z_{m2}) Z_{m_3}} \tag{3.15}$$

$$\boldsymbol{d = Z_1 (Z_{m_3} - Z_{m_2}) + Z_2 (Z_{m_1} - Z_{m_3}) + Z_3 (Z_{m_2} - Z_{m_1})} \tag{3.16}$$

Comparing (3.3) and (3.12), $\boldsymbol{k_1}$, $\boldsymbol{k_2}$ and $\boldsymbol{k_3}$ can be expressed as:

$$\boldsymbol{k_1 = b/d} \tag{3.17}$$

$$\boldsymbol{k_2 = a/d} \tag{3.18}$$

$$\boldsymbol{k_3 = c/d} \tag{3.19}$$

With the measured $\boldsymbol{Z_{m_1}}$, $\boldsymbol{Z_{m_2}}$, and $\boldsymbol{Z_{m_3}}$ for the respective $\boldsymbol{Z_1}$, $\boldsymbol{Z_2}$, and $\boldsymbol{Z_3}$, $\boldsymbol{k_1}$, $\boldsymbol{k_2}$, and $\boldsymbol{k_3}$ can be determined. Then, the relationship between $\boldsymbol{Z_c}$ and $\boldsymbol{Z_m}$ can be fully established. With this relationship, any unknown $\boldsymbol{Z_c}$ can be determined from its respective measured $\boldsymbol{Z_m}$ at *m*-*m′*. Note that both $\boldsymbol{k_1}$ and $\boldsymbol{k_2}$ have a unit of Ω, and $\boldsymbol{k_3}$ is unitless.

Similarly, through network analysis, *m*-*m′* of Fig. 3-4 is related to *l*-*l′* by the following expression:

$$\boldsymbol{Z_L = \frac{h_1 Z_m + h_2}{Z_m + h_3}} \tag{3.20}$$

where

$$\boldsymbol{h_1 = -(B_2 C_1 + D_1 D_2)/(A_2 C_1 + C_2 D_1)} \tag{3.21}$$

$$\boldsymbol{h_2 = (A_1 B_2 + B_1 D_2)/(A_2 C_1 + C_2 D_1)} \tag{3.22}$$

$$\boldsymbol{h_3 = -(A_1 A_2 + B_1 C_2)/(A_2 C_1 + C_2 D_1)} \tag{3.23}$$

Again, once $\boldsymbol{h_1}$, $\boldsymbol{h_2}$, and $\boldsymbol{h_3}$ are known, $\boldsymbol{Z_L}$ can be extracted based on the measured $\boldsymbol{Z_m}$. Note that $\boldsymbol{h_1}$, $\boldsymbol{h_2}$, and $\boldsymbol{h_3}$ are dependent on the two-port *ABCD* parameters of the inductive probe, the power supply, and the cables. To determine $\boldsymbol{h_1}$, $\boldsymbol{h_2}$, and $\boldsymbol{h_3}$, a pre-measurement characterization of the SPS must be performed by removing $\boldsymbol{Z_L}$ (only if $\boldsymbol{Z_L}$ is accessible) from *l*-*l′* and replaced it with three known distinct impedances, $\boldsymbol{Z_1}$, $\boldsymbol{Z_2}$ and $\boldsymbol{Z_3}$, where $\boldsymbol{Z_1 \neq Z_2 \neq Z_3}$. The pre-measurement characterization setup is shown in Fig. 3-6.

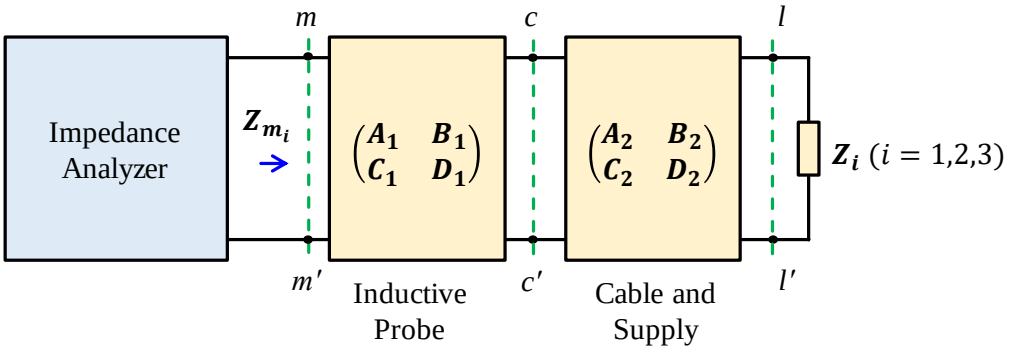

Fig. 3-6. Pre-measurement characterization of SPS at *l*-*l′*.

By substituting $\boldsymbol{Z_1}$, $\boldsymbol{Z_2}$, and $\boldsymbol{Z_3}$ into (3.20) leads to:

$$\boldsymbol{Z_1 = \frac{h_1 Z_{m_1} + h_2}{Z_{m_1} + h_3}} \tag{3.24}$$

$$\boldsymbol{Z_2 = \frac{h_1 Z_{m_2} + h_2}{Z_{m_2} + h_3}} \tag{3.25}$$

$$\boldsymbol{Z_3 = \frac{h_1 Z_{m_3} + h_2}{Z_{m_3} + h_3}} \tag{3.26}$$

where $\boldsymbol{Z_{m_1}}$, $\boldsymbol{Z_{m_2}}$, and $\boldsymbol{Z_{m_3}}$ are the measured impedances by the IA at *m*-*m'* for $\boldsymbol{Z_1}$, $\boldsymbol{Z_2}$ and $\boldsymbol{Z_3}$, respectively. Combining (3.20), (3.24), and (3.25) leads to:

$$\boldsymbol{\left(\frac{Z_L - Z_1}{Z_1 - Z_2}\right) = \left(\frac{\frac{h_1 Z_m + h_2}{Z_m + h_3} - \frac{h_1 Z_{m_1} + h_2}{Z_{m_1} + h_3}}{\frac{h_1 Z_{m_1} + h_2}{Z_{m_1} + h_3} - \frac{h_1 Z_{m_2} + h_2}{Z_{m_2} + h_3}}\right)} \tag{3.27}$$

Similarly, combining (3.20), (3.25), and (3.26) leads to:

$$\boldsymbol{\left(\frac{Z_2 - Z_3}{Z_3 - Z_L}\right) = \left(\frac{\frac{h_1 Z_{m_2} + h_2}{Z_{m_2} + h_3} - \frac{h_1 Z_{m_3} + h_2}{Z_{m_3} + h_3}}{\frac{h_1 Z_{m_3} + h_2}{Z_{m_3} + h_3} - \frac{h_1 Z_m + h_2}{Z_m + h_3}}\right)} \tag{3.28}$$

By multiplying (3.27) and (3.28):

$$\boldsymbol{Z_L = \frac{a + bZ_m}{c + dZ_m}} \tag{3.29}$$

where

$$\boldsymbol{a = Z_1 Z_2 (Z_{m_2} - Z_{m_1}) Z_{m_3} + Z_1 Z_3 (Z_{m_1} - Z_{m_3}) Z_{m_2} + Z_2 Z_3 (Z_{m_3} - Z_{m_2}) Z_{m_1}} \tag{3.30}$$

$$\boldsymbol{b = Z_1 Z_2 (Z_{m_1} - Z_{m_2}) + Z_1 Z_3 (Z_{m_3} - Z_{m_1}) + Z_2 Z_3 (Z_{m_2} - Z_{m_3})} \tag{3.31}$$

$$\boldsymbol{c = Z_1 (Z_{m_2} - Z_{m_3}) Z_{m_1} + Z_2 (Z_{m_3} - Z_{m_1}) Z_{m_2} + Z_3 (Z_{m_1} - Z_{m2}) Z_{m_3}} \tag{3.32}$$

$$\boldsymbol{d = Z_1 (Z_{m_3} - Z_{m_2}) + Z_2 (Z_{m_1} - Z_{m_3}) + Z_3 (Z_{m_2} - Z_{m_1})} \tag{3.33}$$

Comparing (3.20) and (3.29), $\boldsymbol{h_1}$, $\boldsymbol{h_2}$ and $\boldsymbol{h_3}$ can be expressed as:

$$\boldsymbol{h_1 = b/d} \tag{3.34}$$

$$\boldsymbol{h_2 = a/d} \tag{3.35}$$

$$h_3 = c/d \tag{3.36}$$

With the measured Z_{m1}, Z_{m2}, and Z_{m3} for the respective Z_1, Z_2, and Z_3, h_1, h_2 and h_3 can be determined. Then, the relationship between Z_L and Z_m can be established. With this relationship, any unknown Z_L can be extracted from the respective measured Z_m at *m-m'*. Note that both h_1 and h_2 have units of Ω, and h_3 is unitless. Also, to take note that any changes in the cabling and the power supply will require re-characterization of h_1, h_2 and h_3.

3.3 VNA Based Implementation

Fig. 3-7 shows the SPS with a VNA as the impedance measurement instrument. The reflection coefficient measured by the VNA at *m-m'* is Γ_m. The reflection coefficient and the impedance seen at *c-c'* are Γ_c and Z_c, respectively. The reflection coefficient and the impedance of the load at *l-l'* are Γ_L and Z_L, respectively.

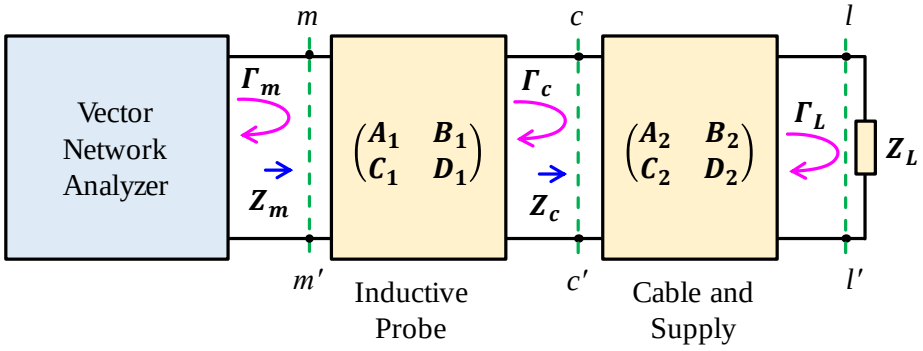

Fig. 3-7. In-circuit impedance measurement using SPS with VNA as the measurement instrument.

Through network analysis, *m-m'* is related to *c-c'* by:

$$\Gamma_m = \frac{\frac{A_1 Z_c + B_1}{C_1 Z_c + D_1} - Z_0}{\frac{A_1 Z_c + B_1}{C_1 Z_c + D_1} + Z_0} \tag{3.37}$$

where Z_0 is the reference impedance of the VNA (usually 50 Ω). (3.37) can be rewritten as:

$$Z_c = \frac{k_1 \Gamma_m + k_2}{\Gamma_m + k_3} \tag{3.38}$$

where

$$k_1 = -\frac{B_1 + D_1 Z_0}{A_1 + C_1 Z_0} \tag{3.39}$$

$$k_2 = -\frac{D_1 Z_0 - B_1}{A_1 + C_1 Z_0} \tag{3.40}$$

$$k_3 = \frac{C_1 Z_0 - A_1}{A_1 + C_1 Z_0} \tag{3.41}$$

Once k_1, k_2, and k_3 are properly determined, Z_c can be extorted through the measured Γ_m. k_1, k_2, and k_3 are dependent on the two-port *ABCD* parameters of the inductive probe and the reference impedance of the VNA (Z_0). To determine k_1, k_2, and k_3 a pre-measurement characterization must be performed by removing the SUT at *c*-*c′* and replacing it with three known distinct impedances, Z_1, Z_2 and Z_3, where $Z_1 \neq Z_2 \neq Z_3$. The pre-measurement characterization setup is shown in Fig. 3-8.

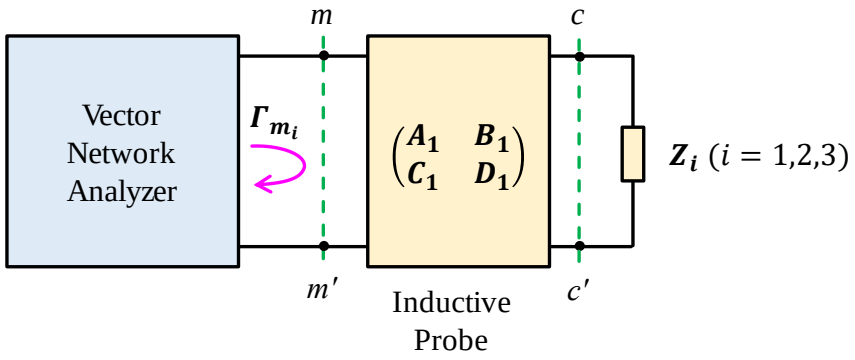

Fig. 3-8. Pre-measurement characterization with VNA at *c*-*c′*.

By substituting Z_1, Z_2, and Z_3 into (3.38):

$$Z_1 = \frac{k_1 \Gamma_{m_1} + k_2}{\Gamma_{m_1} + k_3} \tag{3.42}$$

$$Z_2 = \frac{k_1 \Gamma_{m_2} + k_2}{\Gamma_{m_2} + k_3} \tag{3.43}$$

$$\boldsymbol{Z_3 = \frac{k_1 \Gamma_{m_3} + k_2}{\Gamma_{m_3} + k_3}} \tag{3.44}$$

where $\boldsymbol{\Gamma_{m_1}}$, $\boldsymbol{\Gamma_{m_2}}$, and $\boldsymbol{\Gamma_{m_3}}$ are the reflection coefficients measured by the VNA at *m*-*m′* for $\boldsymbol{Z_1}$, $\boldsymbol{Z_2}$ and $\boldsymbol{Z_3}$ at *c*-*c′*, respectively. Combining (3.3), (3.42), and (3.43) leads to:

$$\left(\frac{\boldsymbol{Z_c - Z_1}}{\boldsymbol{Z_1 - Z_2}}\right) = \left(\frac{\dfrac{\boldsymbol{k_1 \Gamma_m + k_2}}{\boldsymbol{\Gamma_m + k_3}} - \dfrac{\boldsymbol{k_1 \Gamma_{m_1} + k_2}}{\boldsymbol{\Gamma_{m_1} + k_3}}}{\dfrac{\boldsymbol{k_1 \Gamma_{m_1} + k_2}}{\boldsymbol{\Gamma_{m_1} + k_3}} - \dfrac{\boldsymbol{k_1 \Gamma_{m_2} + k_2}}{\boldsymbol{\Gamma_{m_2} + k_3}}}\right) \tag{3.45}$$

Similarly, combining (3.3), (3.43), and (3.44) leads to:

$$\left(\frac{\boldsymbol{Z_2 - Z_3}}{\boldsymbol{Z_3 - Z_c}}\right) = \left(\frac{\dfrac{\boldsymbol{k_1 \Gamma_{m_2} + k_2}}{\boldsymbol{\Gamma_{m_2} + k_3}} - \dfrac{\boldsymbol{k_1 \Gamma_{m_3} + k_2}}{\boldsymbol{\Gamma_{m_3} + k_3}}}{\dfrac{\boldsymbol{k_1 \Gamma_{m_3} + k_2}}{\boldsymbol{\Gamma_{m_3} + k_3}} - \dfrac{\boldsymbol{k_1 \Gamma_m + k_2}}{\boldsymbol{\Gamma_m + k_3}}}\right) \tag{3.46}$$

By multiplying (3.45) and (3.46):

$$\boldsymbol{Z_c = \frac{a + b\Gamma_m}{c + d\Gamma_m}} \tag{3.47}$$

where

$$\boldsymbol{a = \Gamma_{m_1}\Gamma_{m_3}Z_2(Z_3 - Z_1) + \Gamma_{m_2}\Gamma_{m_3}Z_1(Z_2 - Z_3) + \Gamma_{m_1}\Gamma_{m_2}Z_3(Z_1 - Z_2)} \tag{3.48}$$

$$\boldsymbol{b = \Gamma_{m_1}Z_1(Z_2 - Z_3) + \Gamma_{m_2}Z_2(Z_3 - Z_1) + \Gamma_{m_3}Z_3(Z_1 - Z_2)} \tag{3.49}$$

$$\boldsymbol{c = \Gamma_{m_1}Z_1(\Gamma_{m_2} - \Gamma_{m_3}) + \Gamma_{m_2}Z_2(\Gamma_{m_3} - \Gamma_{m_1}) + \Gamma_{m_3}Z_3(\Gamma_{m_1} - \Gamma_{m_2})} \tag{3.50}$$

$$\boldsymbol{d = Z_1(\Gamma_{m_3} - \Gamma_{m_2}) + Z_2(\Gamma_{m_1} - \Gamma_{m_3}) + Z_3(\Gamma_{m_2} - \Gamma_{m_1})} \tag{3.51}$$

Comparing (3.3) and (3.47), $\boldsymbol{k_1}$, $\boldsymbol{k_2}$ and $\boldsymbol{k_3}$ can be expressed as:

$$\boldsymbol{k_1 = b/d} \tag{3.52}$$

$$\boldsymbol{k_2 = a/d} \tag{3.53}$$

$$\boldsymbol{k_3 = c/d} \tag{3.54}$$

With the measured $\boldsymbol{\Gamma_{m_1}}$, $\boldsymbol{\Gamma_{m_2}}$, and $\boldsymbol{\Gamma_{m_3}}$ for the respective $\boldsymbol{Z_1}$, $\boldsymbol{Z_2}$, and $\boldsymbol{Z_3}$, $\boldsymbol{k_1}$, $\boldsymbol{k_2}$ and $\boldsymbol{k_3}$ can be determined. Then the full relationship between $\boldsymbol{Z_c}$ and $\boldsymbol{\Gamma_m}$ can be derived. With this relationship, any unknown $\boldsymbol{Z_c}$ can be extracted with ease from the respective measured $\boldsymbol{\Gamma_m}$ at *m*-*m′*. Note that the $\boldsymbol{k_1}$ are $\boldsymbol{k_2}$ have units of Ω, and $\boldsymbol{k_3}$ is unitless.

If $\boldsymbol{Z_L}$ is accessible, through network analysis, *m-m′* of Fig. 3-7 is related to *l-l′* by:

$$\boldsymbol{Z_L = \frac{h_1 \Gamma_m + h_2}{\Gamma_m + h_3}} \tag{3.55}$$

where

$$\boldsymbol{h_1 = -\frac{Z_0(B_2C_1 + D_1D_2) + A_1B_2 + B_1D_2}{Z_0(A_1C_1 + C_2D_1) + A_1A_2 + B_1C_2}} \tag{3.56}$$

$$\boldsymbol{h_2 = -\frac{Z_0(B_2C_1 + D_1D_2) - A_1B_2 - B_1D_2}{Z_0(A_1C_1 + C_2D_1) + A_1A_2 + B_1C_2}} \tag{3.57}$$

$$\boldsymbol{h_3 = \frac{Z_0(A_2C_1 + C_2D_1) - A_1A_2 - B_1C_2}{Z_0(A_1C_1 + C_2D_1) + A_1A_2 + B_1C_2}} \tag{3.58}$$

Again, with known $\boldsymbol{h_1}$, $\boldsymbol{h_2}$, and $\boldsymbol{h_3}$, $\boldsymbol{Z_L}$ can be determined based on the measured $\boldsymbol{Z_m}$. $\boldsymbol{h_1}$, $\boldsymbol{h_2}$, and $\boldsymbol{h_3}$ are specific to the two-port *ABCD* parameters of the inductive probe, the power supply, the cables, and reference impedance of the VNA ($\boldsymbol{Z_0}$). To determine $\boldsymbol{h_1}$, $\boldsymbol{h_2}$, and $\boldsymbol{h_3}$ a pre-measurement characterization is performed, as shown in Fig. 3-9, by replacing $\boldsymbol{Z_L}$ at *l-l′* (if $\boldsymbol{Z_L}$ is accessible) with three known distinct impedances $\boldsymbol{Z_1}$, $\boldsymbol{Z_2}$ and $\boldsymbol{Z_3}$, where $\boldsymbol{Z_1 \neq Z_2 \neq Z_3}$.

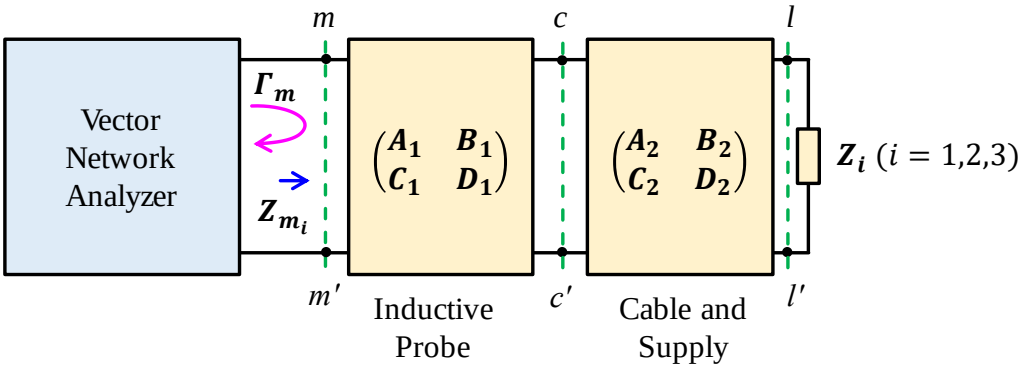

Fig. 3-9. Pre-measurement characterization of SPS with VNA at *l-l′*.

By substituting $\boldsymbol{Z_1}$, $\boldsymbol{Z_2}$, and $\boldsymbol{Z_3}$ into (3.55):

$$\boldsymbol{Z_1 = \frac{h_1 \Gamma_{m_1} + h_2}{\Gamma_{m_1} + h_3}} \tag{3.59}$$

$$\boldsymbol{Z_2 = \frac{h_1 \Gamma_{m_2} + h_2}{\Gamma_{m_2} + h_3}} \tag{3.60}$$

$$\boldsymbol{Z_3 = \frac{h_1 \Gamma_{m_3} + h_2}{\Gamma_{m_3} + h_3}} \tag{3.61}$$

where $\boldsymbol{\Gamma_{m_1}}$, $\boldsymbol{\Gamma_{m_2}}$, and $\boldsymbol{\Gamma_{m_3}}$ are the reflection coefficients measured by the VNA at *m*-*m′* for $\boldsymbol{Z_1}$, $\boldsymbol{Z_2}$ and $\boldsymbol{Z_3}$, respectively. Combining (3.55), (3.59), and (3.60) leads to:

$$\boldsymbol{\left(\frac{Z_L - Z_1}{Z_1 - Z_2}\right) = \left(\frac{\frac{h_1 \Gamma_m + h_2}{\Gamma_m + h_3} - \frac{h_1 \Gamma_{m_1} + h_2}{\Gamma_{m_1} + h_3}}{\frac{h_1 \Gamma_{m_1} + h_2}{\Gamma_{m_1} + h_3} - \frac{h_1 \Gamma_{m_2} + h_2}{\Gamma_{m_2} + h_3}}\right)} \tag{3.62}$$

Similarly, combining (3.55), (3.60), and (3.61) leads to:

$$\boldsymbol{\left(\frac{Z_2 - Z_3}{Z_3 - Z_L}\right) = \left(\frac{\frac{h_1 \Gamma_{m_2} + h_2}{\Gamma_{m_2} + h_3} - \frac{h_1 \Gamma_{m_3} + h_2}{\Gamma_{m_3} + h_3}}{\frac{h_1 \Gamma_{m_3} + h_2}{\Gamma_{m_3} + h_3} - \frac{h_1 \Gamma_m + h_2}{\Gamma_m + h_3}}\right)} \tag{3.63}$$

By multiplying (3.62) and (3.63):

$$\boldsymbol{Z_L = \frac{a + b\Gamma_m}{c + d\Gamma_m}} \tag{3.64}$$

where

$$\boldsymbol{a = \Gamma_{m_1}\Gamma_{m_3}Z_2(Z_3 - Z_1) + \Gamma_{m_2}\Gamma_{m_3}Z_1(Z_2 - Z_3) + \Gamma_{m_1}\Gamma_{m_2}Z_3(Z_1 - Z_2)} \tag{3.65}$$

$$\boldsymbol{b = \Gamma_{m_1}Z_1(Z_2 - Z_3) + \Gamma_{m_2}Z_2(Z_3 - Z_1) + \Gamma_{m_3}Z_3(Z_1 - Z_2)} \tag{3.66}$$

$$\boldsymbol{c = \Gamma_{m_1}Z_1(\Gamma_{m_2} - \Gamma_{m_3}) + \Gamma_{m_2}Z_2(\Gamma_{m_3} - \Gamma_{m_1}) + \Gamma_{m_3}Z_3(\Gamma_{m_1} - \Gamma_{m_2})} \tag{3.67}$$

$$\boldsymbol{d = Z_1(\Gamma_{m_3} - \Gamma_{m_2}) + Z_2(\Gamma_{m_1} - \Gamma_{m_3}) + Z_3(\Gamma_{m_2} - \Gamma_{m_1})} \tag{3.68}$$

Comparing (3.55) and (3.64), $\boldsymbol{h_1, h_2}$ and $\boldsymbol{h_3}$ can be expressed as:

$$\boldsymbol{h_1 = b/d} \tag{3.69}$$

$$\boldsymbol{h_2 = a/d} \tag{3.70}$$

$$\boldsymbol{h_3 = c/d} \tag{3.71}$$

By measuring $\boldsymbol{\Gamma_{m_1}}$, $\boldsymbol{\Gamma_{m_2}}$, and $\boldsymbol{\Gamma_{m_3}}$ for the respective $\boldsymbol{Z_1}$, $\boldsymbol{Z_2}$, and $\boldsymbol{Z_3}$, $\boldsymbol{h_1}$, $\boldsymbol{h_2}$, and $\boldsymbol{h_3}$ can be obtained. Then the relationship between $\boldsymbol{Z_L}$ and $\boldsymbol{\Gamma_m}$ can be fully described. With this known relationship, any unknown $\boldsymbol{Z_L}$ can be extracted from the respective measured $\boldsymbol{\Gamma_m}$ at *m*-*m′* by the VNA. Note that the $\boldsymbol{h_1}$ and $\boldsymbol{h_2}$ have units of Ω, and $\boldsymbol{h_3}$ is unitless. Similarly, any changes in the cabling and the power supply requires re-characterization of $\boldsymbol{h_1}$, $\boldsymbol{h_2}$ and $\boldsymbol{h_3}$.

3.4 Systematic Error Cancellation

With the pre-characterization of the SPS to determine $\boldsymbol{k_1}$, $\boldsymbol{k_2}$, and $\boldsymbol{k_3}$, or $\boldsymbol{h_1}$, $\boldsymbol{h_2}$ and $\boldsymbol{h_3}$, it allows cancellation of the systematic errors that exist in the measurement instrument, be it an IA or a VNA, which will be briefly explained in this section.

For a linear error model, the systematic error has two terms, the proportional error and the offset error. Assume that $\boldsymbol{\Gamma_m}$ measured by the VNA has an offset error and a proportional error of $\boldsymbol{\alpha}$ and $\boldsymbol{\beta}$, respectively. Then the measured $\boldsymbol{\Gamma_m}$ and the true reflection coefficients $\boldsymbol{\Gamma_T}$ at *m*-*m′* are related by:

$$\boldsymbol{\Gamma_m} = (1 + \boldsymbol{\beta})\boldsymbol{\Gamma_T} + \boldsymbol{\alpha} \tag{3.72}$$

Therefore, the measurements during the pre-measurement characterization of SPS can be expressed in terms of $\boldsymbol{\alpha}$ and $\boldsymbol{\beta}$ for the explanation of error cancellation. From (3.45) and (3.46) the following equations are formed:

$$\left(\frac{\boldsymbol{Z_c - Z_1}}{\boldsymbol{Z_1 - Z_2}}\right) = \left(\frac{\dfrac{\boldsymbol{k_1\Gamma_m + k_2}}{\boldsymbol{\Gamma_m + k_3}} - \dfrac{\boldsymbol{k_1\Gamma_{m_1} + k_2}}{\boldsymbol{\Gamma_{m_1} + k_3}}}{\dfrac{\boldsymbol{k_1\Gamma_{m_1} + k_2}}{\boldsymbol{\Gamma_{m_1} + k_3}} - \dfrac{\boldsymbol{k_1\Gamma_{m_2} + k_2}}{\boldsymbol{\Gamma_{m_2} + k_3}}}\right)$$

$$= \left(\frac{\dfrac{\boldsymbol{k_1\left((1+\beta)\Gamma_T + \alpha\right) + k_2}}{\boldsymbol{(1+\beta)\Gamma_T + \alpha + k_3}} - \dfrac{\boldsymbol{k_1\left((1+\beta)\Gamma_{T_1} + \alpha\right) + k_2}}{\boldsymbol{(1+\beta)\Gamma_{T_1} + \alpha + k_3}}}{\dfrac{\boldsymbol{k_1\left((1+\beta)\Gamma_{T_1} + \alpha\right) + k_2}}{\boldsymbol{(1+\beta)\Gamma_{T_1} + \alpha + k_3}} - \dfrac{\boldsymbol{k_1\left((1+\beta)\Gamma_{T_2} + \alpha\right) + k_2}}{\boldsymbol{(1+\beta)\Gamma_{T_2} + \alpha + k_3}}}\right) \quad (3.73)$$

$$\left(\frac{\boldsymbol{Z_2 - Z_3}}{\boldsymbol{Z_3 - Z_c}}\right) = \left(\frac{\dfrac{\boldsymbol{k_1\Gamma_{m_2} + k_2}}{\boldsymbol{\Gamma_{m_2} + k_3}} - \dfrac{\boldsymbol{k_1\Gamma_{m_3} + k_2}}{\boldsymbol{\Gamma_{m_3} + k_3}}}{\dfrac{\boldsymbol{k_1\Gamma_{m_3} + k_2}}{\boldsymbol{\Gamma_{m_3} + k_3}} - \dfrac{\boldsymbol{k_1\Gamma_m + k_2}}{\boldsymbol{\Gamma_m + k_3}}}\right)$$

$$= \left(\frac{\dfrac{\boldsymbol{k_1\left((1+\beta)\Gamma_{T_2} + \alpha\right) + k_2}}{\boldsymbol{(1+\beta)\Gamma_{T_2} + \alpha + k_3}} - \dfrac{\boldsymbol{k_1\left((1+\beta)\Gamma_{T_3} + \alpha\right) + k_2}}{\boldsymbol{(1+\beta)\Gamma_{T_3} + \alpha + k_3}}}{\dfrac{\boldsymbol{k_1\left((1+\beta)\Gamma_{T_3} + \alpha\right) + k_2}}{\boldsymbol{(1+\beta)\Gamma_{T_3} + \alpha + k_3}} - \dfrac{\boldsymbol{k_1\left((1+\beta)\Gamma_T + \alpha\right) + k_2}}{\boldsymbol{(1+\beta)\Gamma_T + \alpha + k_3}}}\right) \quad (3.74)$$

where $\boldsymbol{\Gamma_{T_1}}$, $\boldsymbol{\Gamma_{T_2}}$, and $\boldsymbol{\Gamma_{T_3}}$ are the true reflection coefficients when the $\boldsymbol{Z_1}$, $\boldsymbol{Z_2}$ and $\boldsymbol{Z_3}$ are connected at *c*-*c′*, respectively. The expressions (3.73) and (3.74) can be simplified as:

$$\left(\frac{\boldsymbol{Z_c - Z_1}}{\boldsymbol{Z_1 - Z_2}}\right) = \left(\frac{\boldsymbol{\Gamma_m - \Gamma_{m_1}}}{\boldsymbol{\Gamma_{m_1} - \Gamma_{m_2}}}\right)\left(\frac{\boldsymbol{k_3 + \Gamma_{m_2}}}{\boldsymbol{k_3 + \Gamma_m}}\right) = \left(\frac{\boldsymbol{\Gamma_T - \Gamma_{T_1}}}{\boldsymbol{\Gamma_{T_1} - \Gamma_{T_2}}}\right)\left(\frac{\boldsymbol{\alpha + (1+\beta)\Gamma_{T_2} + k_3}}{\boldsymbol{\alpha + (1+\beta)\Gamma_T + k_3}}\right) \quad (3.75)$$

$$\left(\frac{\boldsymbol{Z_2 - Z_3}}{\boldsymbol{Z_3 - Z_c}}\right) = \left(\frac{\boldsymbol{\Gamma_{m_2} - \Gamma_{m_3}}}{\boldsymbol{\Gamma_{m_3} - \Gamma_m}}\right)\left(\frac{\boldsymbol{k_3 + \Gamma_m}}{\boldsymbol{k_3 + \Gamma_{m_2}}}\right) = \left(\frac{\boldsymbol{\Gamma_{T_2} - \Gamma_{T_3}}}{\boldsymbol{\Gamma_{T_3} - \Gamma_T}}\right)\left(\frac{\boldsymbol{\alpha + (1+\beta)\Gamma_T + k_3}}{\boldsymbol{\alpha + (1+\beta)\Gamma_{T_2} + k_3}}\right) \quad (3.76)$$

By multiplying (3.75) and (3.76)

$$\left(\frac{\boldsymbol{Z_c - Z_1}}{\boldsymbol{Z_1 - Z_2}}\right)\left(\frac{\boldsymbol{Z_2 - Z_3}}{\boldsymbol{Z_3 - Z_c}}\right) = \left(\frac{\boldsymbol{\Gamma_m - \Gamma_{m_1}}}{\boldsymbol{\Gamma_{m_1} - \Gamma_{m_2}}}\right)\left(\frac{\boldsymbol{\Gamma_{m_2} - \Gamma_{m_3}}}{\boldsymbol{\Gamma_{m_3} - \Gamma_m}}\right)$$

$$= \left(\frac{\boldsymbol{\Gamma_T - \Gamma_{T_1}}}{\boldsymbol{\Gamma_{T_1} - \Gamma_{T_2}}}\right)\left(\frac{\boldsymbol{\Gamma_{T_2} - \Gamma_{T_3}}}{\boldsymbol{\Gamma_{T_3} - \Gamma_T}}\right) \quad (3.77)$$

As observed in (3.77), the two error terms $\boldsymbol{\alpha}$ and $\boldsymbol{\beta}$ have diminished, which shows that these error terms have been canceled during the pre-measurement characterization process at the *l*-*l′* reference plane. Similarly, the systematic errors in the IA-based measurement are also canceled out by this pre-measurement characterization procedure for the same reason.

3.5 Experimental Validation

For validation purposes, Fig. 3-10 emulates a simple DC-powered passive component as an energized SUT, where the in-circuit impedance will be measured with the SPS. The lithium battery (3.7 V – 18650) serves as the DC power source to the passive component. An inductive probe (Solar 9144–1N) is clamped onto a wire that connects the passive component to the battery. The VNA (Bode 100) is connected to the inductive probe with a coaxial cable and interfaced with a PC for data collection and post-processing. The actual setup is shown in Fig. 3-11(a). A few passive components are selected to emulate unknown impedances to be measured through the in-circuit measurement setup. Their respective impedance responses are measured off-circuit using an IA as references for comparison. These passive components are chosen to cover a wide dynamic impedance range of $\boldsymbol{Z_L}$. They include resistors (10 Ω – 5 kΩ), capacitors (330 pF – 10 nF), and inductors (1 µH – 100 µH). The pre-measurement characterization is performed at *l*-*l′* so that the impedance of the passive component can be extracted to compare against the reference. Fig. 3-11(b) shows a sample passive $\boldsymbol{Z_L}$ of the SUT

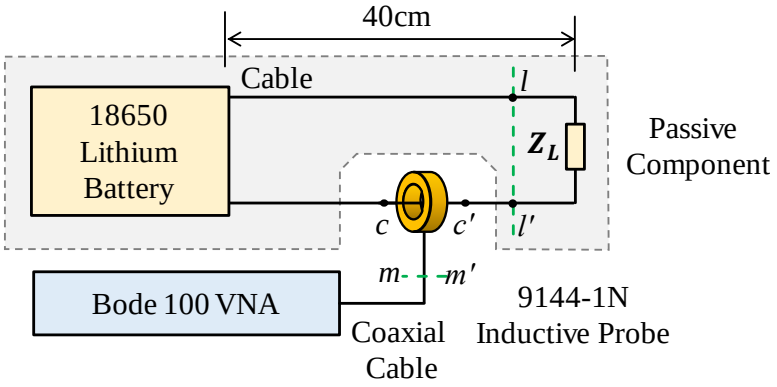

Fig. 3-10. Experimental validation of the SPS.

Fig. 3-12, Fig. 3-13, and Fig. 3-14 show the extracted $\boldsymbol{Z_L}$ with the SPS and compare with the corresponding reference from 150 kHz to 30 MHz. Good agreement with the reference, both in magnitude and phase is demonstrated. The worst discrepancies in magnitude and phase

are found to be within 5% and 2°, respectively, for a dynamic impedance range of 0.5 Ω to 10 kΩ.

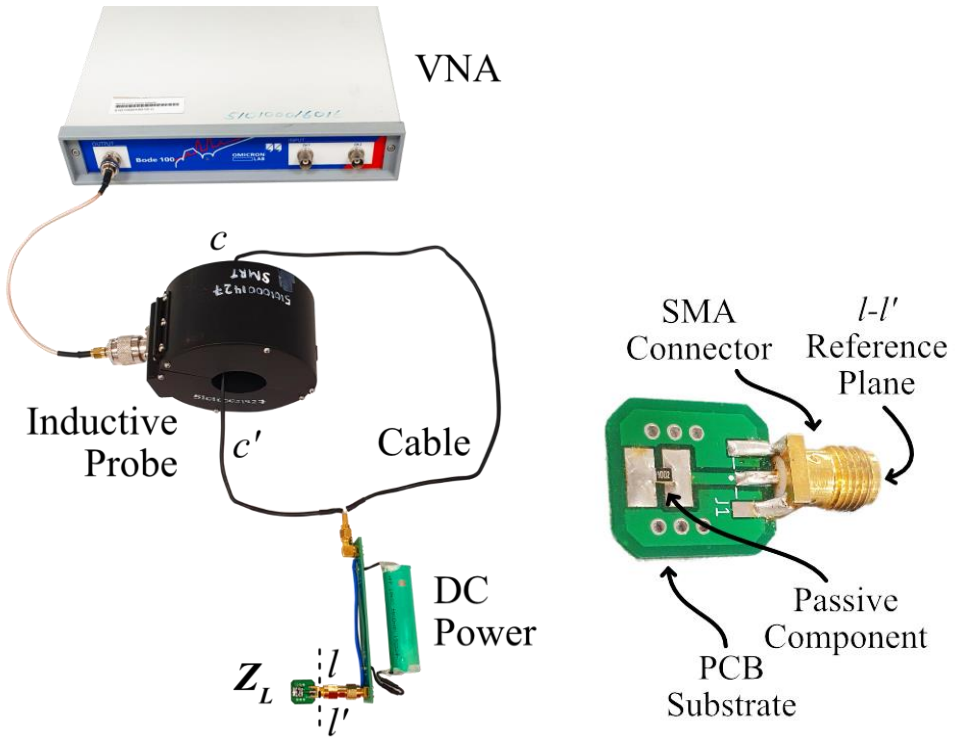

Fig. 3-11. $\boldsymbol{Z_L}$ (a) Measured by the SPS (b) Measured offline with an IA.

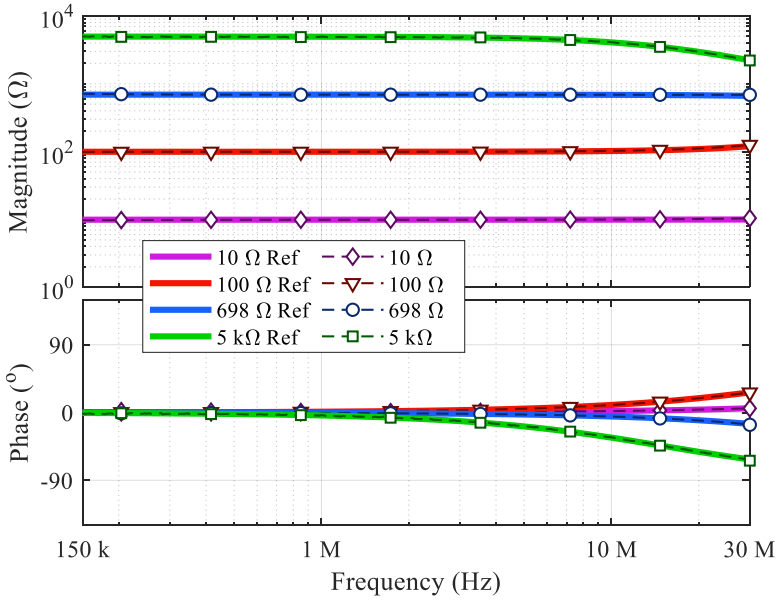

Fig. 3-12. Comparison of measured and reference impedances of resistors.

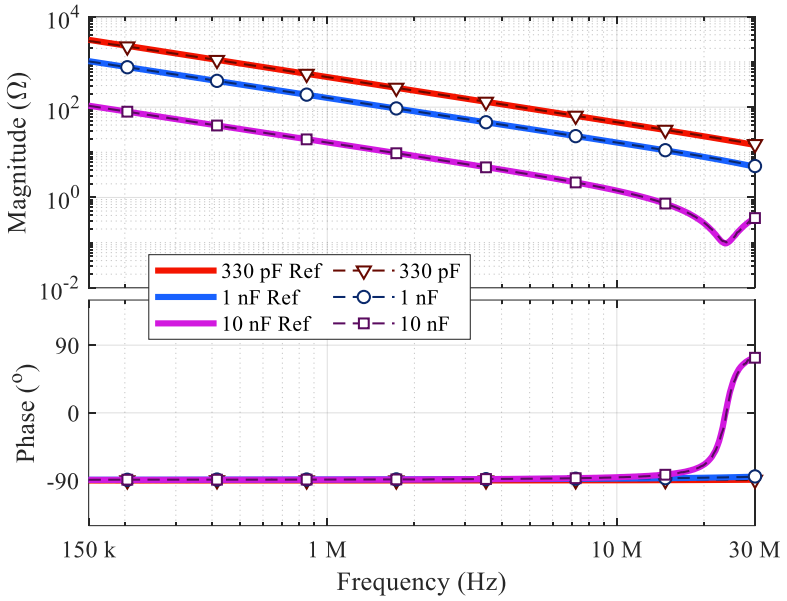

Fig. 3-13. Comparison of measured and reference impedances of capacitors.

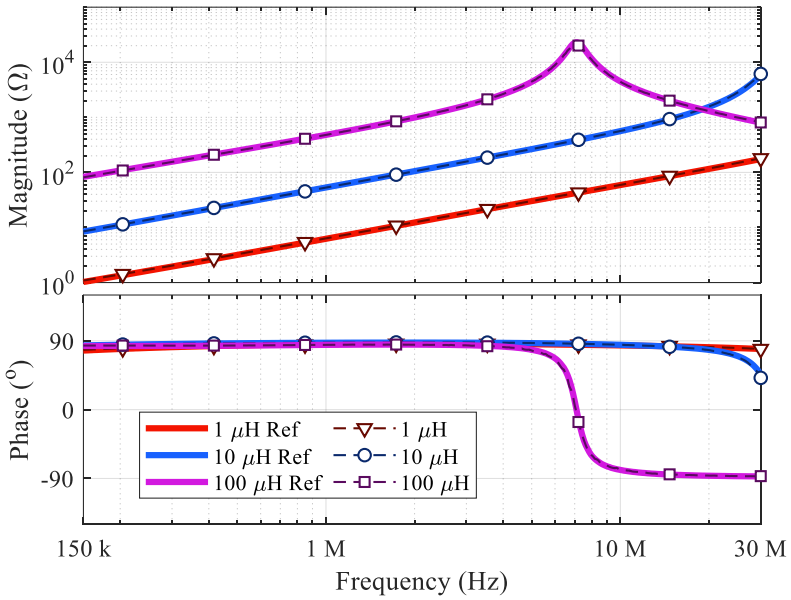

Fig. 3-14. Comparison of measured and reference impedances of inductors.

3.6 Discussion and Summary

The principle behind the SPS for in-circuit impedance measurement with FD-based instrumentation has been described. The implementations using an IA and a VNA have also

been elaborated in detail. The full mathematical expressions have been derived for the extraction of the SUT impedance seen by the inductive probe ($\boldsymbol{Z_c}$) and unknown load impedance ($\boldsymbol{Z_L}$). A pre-measurement characterization procedure has been developed so that the systematic error inherent in the test instrument can be canceled to preserve the measurement accuracy of the SPS. The validity of the SPS has been demonstrated experimentally using a DC-powered passive component as a SUT. The experimental validation has demonstrated the ability of the SPS to extract in-circuit impedance with a dynamic range of 0.5 Ω to 10 kΩ, and the magnitude and phase discrepancies are within 5% and 2°, respectively.

Chapter 4 Single-Probe In-Circuit Impedance Extraction with Time-Domain Based Instrumentation

This chapter describes the implementation of SPS with TD-based instrumentation for in-circuit impedance measurement. The TD-based instrumentation is usually preferred, as it can be combined with various DSP algorithms to perform more complex in-circuit impedance analysis tasks. The TD-based instrumentation also allows in-circuit impedance measurement to be done at multiple frequencies simultaneously, which significantly reduces the measurement time for a wide band of frequency, as compared to the FD-based counterpart. Therefore, the synthesis of a multitone excitation signal is adopted and described for simultaneous in-circuit impedance measurement at multiple frequencies. A DSP algorithm is also explained to obtain the required FD impedance from the acquired TD data. The validity of the proposed SPS with TD-based instrumentation is also experimentally verified.

4.1 Basic Principle

The SPS for in-circuit impedance measurement of an energized SUT with TD-based instrumentation is shown in Fig. 4-1. The SUT consists of a load powered by either an AC or a DC power supply through connecting cables. The measurement plane at the load is indicated as *l*-*l′*. An inductive probe is clamped onto one of the power cables at the location marked by *c*-*c′*. The inductive probe is connected to an arbitrary waveform generator (AWG) to provide excitation through an RF directional coupler. The coupled ports of the RF directional coupler

are terminated by a two-channel ADC whose channels are marked by CH1 and CH2, to measure TD signals v_{CH1} and v_{CH2}, respectively. $\boldsymbol{V_{CH1}}$ and $\boldsymbol{V_{CH2}}$ are the FD counterparts derived from the TD signals measured by the ADC using a DSP algorithm. Usually, the AWG and the ADC are parts of a computer-controlled SGAS. The SPS is similar to that of the FD-based approach except for both the excitation source and measurement instrument are TD-based.

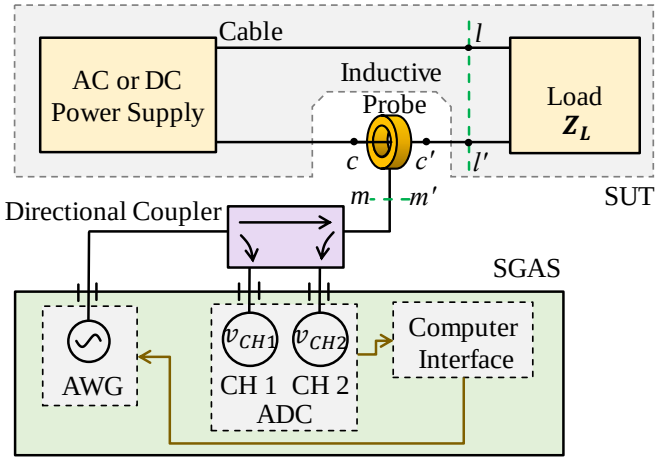

Fig. 4-1. TD-based implementation of SPS for in-circuit impedance measurement.

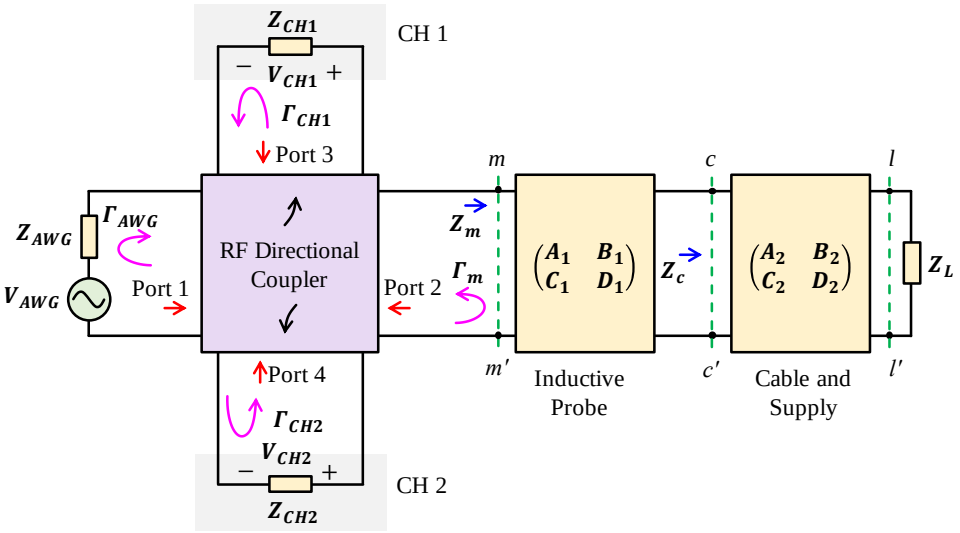

Fig. 4-2. Equivalent network representation of SPS with TD-based instrumentation.

The equivalent network of the SPS shown in Fig. 4-1 is given in Fig. 4-2. The termination impedance of the two ADC channels are denoted by $\boldsymbol{Z_{CH1}}$ and $\boldsymbol{Z_{CH2}}$. The excitation source

AWG has an output impedance of $\boldsymbol{Z_{AWG}}$. The reflection coefficients of CH1, CH2 and AWG terminations are denoted by $\boldsymbol{\Gamma_{CH1}}$, $\boldsymbol{\Gamma_{CH2}}$, and $\boldsymbol{\Gamma_{AWG}}$, respectively. The directional coupler is regarded as a four-port network. The signal flowgraph for the RF directional coupler is shown in Fig. 4-3 indicating the most significant couplings [60]. The directional coupler characteristics are denoted by four-port *S*-parameters. The reflection coefficients seen by the individual ports are denoted by their respective reflection coefficients $\boldsymbol{\Gamma_{CH1}}$, $\boldsymbol{\Gamma_{CH2}}$, $\boldsymbol{\Gamma_{AWG}}$, and $\boldsymbol{\Gamma_m}$.

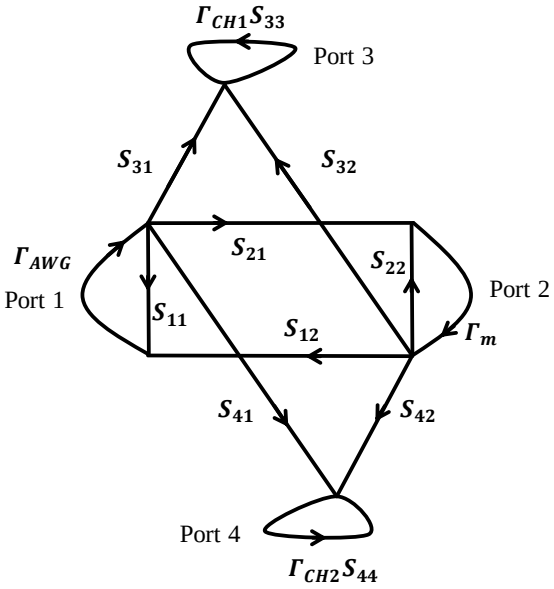

Fig. 4-3. Signal flow graph of the RF directional coupler.

The ratio of $\boldsymbol{V_{CH1}}$ and $\boldsymbol{V_{CH2}}$ can be established by signal flow graph analysis as

$$\frac{\boldsymbol{V_{CH2}}}{\boldsymbol{V_{CH1}}} = \left(\frac{\boldsymbol{p_1} + \boldsymbol{p_2}\boldsymbol{\Gamma_m}}{1 + \boldsymbol{p_3}\boldsymbol{\Gamma_m}}\right) \tag{4.1}$$

where

$$\boldsymbol{p_1} = \frac{\boldsymbol{S_{41}}}{\boldsymbol{S_{31}}}\left(\frac{1 - \boldsymbol{\Gamma_{CH1}}\boldsymbol{S_{33}}}{1 - \boldsymbol{\Gamma_{CH2}}\boldsymbol{S_{44}}}\right) \tag{4.2}$$

$$\boldsymbol{p_2} = \frac{(\boldsymbol{S_{21}}\boldsymbol{S_{42}} - \boldsymbol{S_{41}}\boldsymbol{S_{22}})}{\boldsymbol{S_{31}}}\left(\frac{1 - \boldsymbol{\Gamma_{CH1}}\boldsymbol{S_{33}}}{1 - \boldsymbol{\Gamma_{CH2}}\boldsymbol{S_{44}}}\right) \tag{4.3}$$

$$\boldsymbol{p_3} = \frac{(\boldsymbol{S_{21}}\boldsymbol{S_{32}} - \boldsymbol{S_{31}}\boldsymbol{S_{22}})}{\boldsymbol{S_{31}}} \tag{4.4}$$

and

$$\boldsymbol{Z_m = Z_0 \frac{1+\Gamma_m}{1-\Gamma_m}} \tag{4.5}$$

$$\boldsymbol{Z_c = -\frac{Z_m D_1 - B_1}{Z_m C_1 - A_1}} \tag{4.6}$$

By combining (4.5), (4.6) and rearranging,

$$\boldsymbol{\Gamma_m = -\frac{Z_c(C_1 Z_0 - A_1) + D_1 Z_0 - B_1}{Z_c(A_1 + C_1 Z_0) + D_1 Z_0 + B_1}} \tag{4.7}$$

By substituting $\boldsymbol{\Gamma_m}$ obtained from (4.7) to (4.1),

$$\boldsymbol{\frac{V_{CH2}}{V_{CH1}} = \frac{\big(A_1(p_1+p_2) + C_1 Z_0(p_1-p_2)\big)Z_c + B_1(p_1+p_2) + D_1 Z_0(p_1-p_2)}{\big(A_1(p_3+1) + C_1 Z_0(1-p_3)\big)Z_c + B_1(p_3+1) + D_1 Z_0(1-p_3)}} \tag{4.8}$$

The expression of (4.8) can be rearranged in the following form,

$$\boldsymbol{Z_c = \frac{k_1\left(\frac{V_{CH2}}{V_{CH1}}\right) + k_2}{\left(\frac{V_{CH2}}{V_{CH1}}\right) + k_3}} \tag{4.9}$$

where

$$\boldsymbol{k_1 = -\frac{D_1(1-p_3)Z_0 + B_1(1+p_3)}{C_1(1-p_3)Z_0 + A_1(1+p_3)}} \tag{4.10}$$

$$\boldsymbol{k_2 = -\frac{D_1(p_1-p_2)Z_0 + B_1(p_1+p_2)}{C_1(1-p_3)Z_0 + A_1(1+p_3)}} \tag{4.11}$$

$$\boldsymbol{k_3 = \frac{C_1(p_1-p_2)Z_0 + A_1(p_1+p_2)}{C_1(1-p_3)Z_0 + A_1(1+p_3)}} \tag{4.12}$$

Let define $(\boldsymbol{V_{CH2}/V_{CH1}})$ as the vector voltage ratio (VVR). Once $\boldsymbol{k_1}$, $\boldsymbol{k_2}$, and $\boldsymbol{k_3}$ are known, the impedance seen by the inductive probe ($\boldsymbol{Z_c}$) can be determined based on the measured VVR. $\boldsymbol{p_1}$, $\boldsymbol{p_2}$, and $\boldsymbol{p_3}$ are dependent on the directional coupler characteristics such as directivity, insertion loss, coupling factor, and isolation. $\boldsymbol{k_1}$, $\boldsymbol{k_2}$, and $\boldsymbol{k_3}$ are dependent on the directional coupler characteristics, as well as the inductive probe characteristics, and the selected reference impedance $\boldsymbol{Z_0}$. Since $\boldsymbol{k_1}$, $\boldsymbol{k_2}$, and $\boldsymbol{k_3}$ have already included the effects of $\boldsymbol{p_1}$, $\boldsymbol{p_2}$, and $\boldsymbol{p_3}$, it is sufficient to determine $\boldsymbol{k_1}$, $\boldsymbol{k_2}$, and $\boldsymbol{k_3}$ for the in-circuit impedance measurement using the SPS. Similar to the FD pre-measurement characterization procedure, $\boldsymbol{k_1}$, $\boldsymbol{k_2}$, and $\boldsymbol{k_3}$ can be obtained based on the measured VVR by connecting *c-c′* to three distinct

known impedances $\boldsymbol{Z_1}$, $\boldsymbol{Z_2}$ and $\boldsymbol{Z_3}$, where $\boldsymbol{Z_1 \neq Z_2 \neq Z_3}$. By substituting $\boldsymbol{Z_1}$, $\boldsymbol{Z_2}$, and $\boldsymbol{Z_3}$ into (4.9):

$$\boldsymbol{Z_1 = \frac{k_1\left(\frac{V_{CH2}}{V_{CH1}}\right)_{Z1} + k_2}{\left(\frac{V_{CH2}}{V_{CH1}}\right)_{Z1} + k_3}} \tag{4.13}$$

$$\boldsymbol{Z_2 = \frac{k_1\left(\frac{V_{CH2}}{V_{CH1}}\right)_{Z2} + k_2}{\left(\frac{V_{CH2}}{V_{CH1}}\right)_{Z2} + k_3}} \tag{4.14}$$

$$\boldsymbol{Z_3 = \frac{k_1\left(\frac{V_{CH2}}{V_{CH1}}\right)_{Z3} + k_2}{\left(\frac{V_{CH2}}{V_{CH1}}\right)_{Z3} + k_3}} \tag{4.15}$$

where $\boldsymbol{(V_{CH2}/V_{CH1})_{Z1}}$, $\boldsymbol{(V_{CH2}/V_{CH1})_{Z2}}$, and $\boldsymbol{(V_{CH2}/V_{CH1})_{Z3}}$ are the VVRs for $\boldsymbol{Z_1}$, $\boldsymbol{Z_2}$ and $\boldsymbol{Z_3}$ at *c*-*c′*, respectively. Combining (4.9), (4.13), and (4.14) leads to:

$$\boldsymbol{\left(\frac{Z_c - Z_1}{Z_1 - Z_2}\right) = \left(\frac{\frac{k_1\left(\frac{V_{CH2}}{V_{CH1}}\right) + k_2}{\left(\frac{V_{CH2}}{V_{CH1}}\right) + k_3} - \frac{k_1\left(\frac{V_{CH2}}{V_{CH1}}\right)_{Z1} + k_2}{\left(\frac{V_{CH2}}{V_{CH1}}\right)_{Z1} + k_3}}{\frac{k_1\left(\frac{V_{CH2}}{V_{CH1}}\right)_{Z1} + k_2}{\left(\frac{V_{CH2}}{V_{CH1}}\right)_{Z1} + k_3} - \frac{k_1\left(\frac{V_{CH2}}{V_{CH1}}\right)_{Z2} + k_2}{\left(\frac{V_{CH2}}{V_{CH1}}\right)_{Z2} + k_3}}\right)} \tag{4.16}$$

Similarly, combining (4.9), (4.14), and (4.15) leads to:

$$\boldsymbol{\left(\frac{Z_2 - Z_3}{Z_3 - Z_c}\right) = \left(\frac{\frac{k_1\left(\frac{V_{CH2}}{V_{CH1}}\right)_{Z2} + k_2}{\left(\frac{V_{CH2}}{V_{CH1}}\right)_{Z2} + k_3} - \frac{k_1\left(\frac{V_{CH2}}{V_{CH1}}\right)_{Z3} + k_2}{\left(\frac{V_{CH2}}{V_{CH1}}\right)_{Z3} + k_3}}{\frac{k_1\left(\frac{V_{CH2}}{V_{CH1}}\right)_{Z3} + k_2}{\left(\frac{V_{CH2}}{V_{CH1}}\right)_{Z3} + k_3} - \frac{k_1\left(\frac{V_{CH2}}{V_{CH1}}\right) + k_2}{\left(\frac{V_{CH2}}{V_{CH1}}\right) + k_3}}\right)} \tag{4.17}$$

By multiplying (4.16) and (4.17):

$$\boldsymbol{Z_c = \frac{a + b\left(\frac{V_{CH2}}{V_{CH1}}\right)}{c + d\left(\frac{V_{CH2}}{V_{CH1}}\right)}} \tag{4.18}$$

where

$$\boldsymbol{a} = \boldsymbol{Z}_2(\boldsymbol{Z}_3 - \boldsymbol{Z}_1)\left(\frac{\boldsymbol{V_{CH2}}}{\boldsymbol{V_{CH1}}}\right)_{\boldsymbol{Z1}}\left(\frac{\boldsymbol{V_{CH2}}}{\boldsymbol{V_{CH1}}}\right)_{\boldsymbol{Z3}} + \boldsymbol{Z}_1(\boldsymbol{Z}_2 - \boldsymbol{Z}_3)\left(\frac{\boldsymbol{V_{CH2}}}{\boldsymbol{V_{CH1}}}\right)_{\boldsymbol{Z2}}\left(\frac{\boldsymbol{V_{CH2}}}{\boldsymbol{V_{CH1}}}\right)_{\boldsymbol{Z3}} + \boldsymbol{Z}_3(\boldsymbol{Z}_1 - \boldsymbol{Z}_2)\left(\frac{\boldsymbol{V_{CH2}}}{\boldsymbol{V_{CH1}}}\right)_{\boldsymbol{Z1}}\left(\frac{\boldsymbol{V_{CH2}}}{\boldsymbol{V_{CH1}}}\right)_{\boldsymbol{Z2}} \tag{4.19}$$

$$\boldsymbol{b} = \boldsymbol{Z}_1(\boldsymbol{Z}_2 - \boldsymbol{Z}_3)\left(\frac{\boldsymbol{V_{CH2}}}{\boldsymbol{V_{CH1}}}\right)_{\boldsymbol{Z1}} + \boldsymbol{Z}_2(\boldsymbol{Z}_3 - \boldsymbol{Z}_1)\left(\frac{\boldsymbol{V_{CH2}}}{\boldsymbol{V_{CH1}}}\right)_{\boldsymbol{Z2}} + \boldsymbol{Z}_3(\boldsymbol{Z}_1 - \boldsymbol{Z}_2)\left(\frac{\boldsymbol{V_{CH2}}}{\boldsymbol{V_{CH1}}}\right)_{\boldsymbol{Z3}} \tag{4.20}$$

$$\boldsymbol{c} = \boldsymbol{Z}_1\left(\frac{\boldsymbol{V_{CH2}}}{\boldsymbol{V_{CH1}}}\right)_{\boldsymbol{Z1}}\left(\left(\frac{\boldsymbol{V_{CH2}}}{\boldsymbol{V_{CH1}}}\right)_{\boldsymbol{Z2}} - \left(\frac{\boldsymbol{V_{CH2}}}{\boldsymbol{V_{CH1}}}\right)_{\boldsymbol{Z3}}\right) + \boldsymbol{Z}_2\left(\frac{\boldsymbol{V_{CH2}}}{\boldsymbol{V_{CH1}}}\right)_{\boldsymbol{Z2}}\left(\left(\frac{\boldsymbol{V_{CH2}}}{\boldsymbol{V_{CH1}}}\right)_{\boldsymbol{Z3}} - \left(\frac{\boldsymbol{V_{CH2}}}{\boldsymbol{V_{CH1}}}\right)_{\boldsymbol{Z1}}\right) + \boldsymbol{Z}_3\left(\frac{\boldsymbol{V_{CH2}}}{\boldsymbol{V_{CH1}}}\right)_{\boldsymbol{Z3}}\left(\left(\frac{\boldsymbol{V_{CH2}}}{\boldsymbol{V_{CH1}}}\right)_{\boldsymbol{Z1}} - \left(\frac{\boldsymbol{V_{CH2}}}{\boldsymbol{V_{CH1}}}\right)_{\boldsymbol{Z2}}\right) \tag{4.21}$$

$$\boldsymbol{d} = \boldsymbol{Z}_1\left(\left(\frac{\boldsymbol{V_{CH2}}}{\boldsymbol{V_{CH1}}}\right)_{\boldsymbol{Z3}} - \left(\frac{\boldsymbol{V_{CH2}}}{\boldsymbol{V_{CH1}}}\right)_{\boldsymbol{Z2}}\right) + \boldsymbol{Z}_2\left(\left(\frac{\boldsymbol{V_{CH2}}}{\boldsymbol{V_{CH1}}}\right)_{\boldsymbol{Z1}} - \left(\frac{\boldsymbol{V_{CH2}}}{\boldsymbol{V_{CH1}}}\right)_{\boldsymbol{Z3}}\right) + \boldsymbol{Z}_3\left(\left(\frac{\boldsymbol{V_{CH2}}}{\boldsymbol{V_{CH1}}}\right)_{\boldsymbol{Z2}} - \left(\frac{\boldsymbol{V_{CH2}}}{\boldsymbol{V_{CH1}}}\right)_{\boldsymbol{Z1}}\right) \tag{4.22}$$

Comparing (4.9) and (4.18), $\boldsymbol{k_1}$, $\boldsymbol{k_2}$ and $\boldsymbol{k_3}$ can be expressed as:

$$\boldsymbol{k_1} = \boldsymbol{b}/\boldsymbol{d} \tag{4.23}$$

$$\boldsymbol{k_2} = \boldsymbol{a}/\boldsymbol{d} \tag{4.24}$$

$$\boldsymbol{k_3} = \boldsymbol{c}/\boldsymbol{d} \tag{4.25}$$

With the measured $(\boldsymbol{V_{CH2}}/\boldsymbol{V_{CH1}})_{\boldsymbol{Z1}}$, $(\boldsymbol{V_{CH2}}/\boldsymbol{V_{CH1}})_{\boldsymbol{Z2}}$, and $(\boldsymbol{V_{CH2}}/\boldsymbol{V_{CH1}})_{\boldsymbol{Z3}}$ for the respective respective $\boldsymbol{Z_1}$, $\boldsymbol{Z_2}$, and $\boldsymbol{Z_3}$, $\boldsymbol{k_1}$, $\boldsymbol{k_2}$, and $\boldsymbol{k_3}$ can be obtained. Then the full relationship between $\boldsymbol{Z_c}$ and the measured VVR can be established. With this relationship, any unknown $\boldsymbol{Z_c}$ can be extracted with ease from the new measured VVR. Note that the $\boldsymbol{k_1}$ and $\boldsymbol{k_2}$ have units of Ω, and $\boldsymbol{k_3}$ is unitless. The above derivations can be repeated to establish the relationship between $\boldsymbol{Z_L}$ and the measured VVR too. Thus,

$$\boldsymbol{Z_L} = \frac{\boldsymbol{h_1}\left(\frac{\boldsymbol{V_{CH2}}}{\boldsymbol{V_{CH1}}}\right) + \boldsymbol{h_2}}{\left(\frac{\boldsymbol{V_{CH2}}}{\boldsymbol{V_{CH1}}}\right) + \boldsymbol{h_3}} \tag{4.26}$$

where

$$\boldsymbol{h_1 = b/d} \tag{4.27}$$

$$\boldsymbol{h_2 = a/d} \tag{4.28}$$

$$\boldsymbol{h_3 = c/d} \tag{4.29}$$

and

$$\begin{aligned}\boldsymbol{a} = \boldsymbol{Z}_2(\boldsymbol{Z}_3 - \boldsymbol{Z}_1)\left(\frac{\boldsymbol{V_{CH2}}}{\boldsymbol{V_{CH1}}}\right)_{\boldsymbol{Z1}}\left(\frac{\boldsymbol{V_{CH2}}}{\boldsymbol{V_{CH1}}}\right)_{\boldsymbol{Z3}} + \boldsymbol{Z}_1(\boldsymbol{Z}_2 - \boldsymbol{Z}_3)\left(\frac{\boldsymbol{V_{CH2}}}{\boldsymbol{V_{CH1}}}\right)_{\boldsymbol{Z2}}\left(\frac{\boldsymbol{V_{CH2}}}{\boldsymbol{V_{CH1}}}\right)_{\boldsymbol{Z3}} \\ + \boldsymbol{Z}_3(\boldsymbol{Z}_1 - \boldsymbol{Z}_2)\left(\frac{\boldsymbol{V_{CH2}}}{\boldsymbol{V_{CH1}}}\right)_{\boldsymbol{Z1}}\left(\frac{\boldsymbol{V_{CH2}}}{\boldsymbol{V_{CH1}}}\right)_{\boldsymbol{Z2}}\end{aligned} \tag{4.30}$$

$$\boldsymbol{b} = \boldsymbol{Z}_1(\boldsymbol{Z}_2 - \boldsymbol{Z}_3)\left(\frac{\boldsymbol{V_{CH2}}}{\boldsymbol{V_{CH1}}}\right)_{\boldsymbol{Z1}} + \boldsymbol{Z}_2(\boldsymbol{Z}_3 - \boldsymbol{Z}_1)\left(\frac{\boldsymbol{V_{CH2}}}{\boldsymbol{V_{CH1}}}\right)_{\boldsymbol{Z2}} + \boldsymbol{Z}_3(\boldsymbol{Z}_1 - \boldsymbol{Z}_2)\left(\frac{\boldsymbol{V_{CH2}}}{\boldsymbol{V_{CH1}}}\right)_{\boldsymbol{Z3}} \tag{4.31}$$

$$\begin{aligned}\boldsymbol{c} = \boldsymbol{Z}_1\left(\frac{\boldsymbol{V_{CH2}}}{\boldsymbol{V_{CH1}}}\right)_{\boldsymbol{Z1}}\left(\left(\frac{\boldsymbol{V_{CH2}}}{\boldsymbol{V_{CH1}}}\right)_{\boldsymbol{Z2}} - \left(\frac{\boldsymbol{V_{CH2}}}{\boldsymbol{V_{CH1}}}\right)_{\boldsymbol{Z3}}\right) \\ + \boldsymbol{Z}_2\left(\frac{\boldsymbol{V_{CH2}}}{\boldsymbol{V_{CH1}}}\right)_{\boldsymbol{Z2}}\left(\left(\frac{\boldsymbol{V_{CH2}}}{\boldsymbol{V_{CH1}}}\right)_{\boldsymbol{Z3}} - \left(\frac{\boldsymbol{V_{CH2}}}{\boldsymbol{V_{CH1}}}\right)_{\boldsymbol{Z1}}\right) \\ + \boldsymbol{Z}_3\left(\frac{\boldsymbol{V_{CH2}}}{\boldsymbol{V_{CH1}}}\right)_{\boldsymbol{Z3}}\left(\left(\frac{\boldsymbol{V_{CH2}}}{\boldsymbol{V_{CH1}}}\right)_{\boldsymbol{Z1}} - \boldsymbol{\Gamma_{m_2}}\right)\end{aligned} \tag{4.32}$$

$$\begin{aligned}\boldsymbol{d} = \boldsymbol{Z}_1\left(\left(\frac{\boldsymbol{V_{CH2}}}{\boldsymbol{V_{CH1}}}\right)_{\boldsymbol{Z3}} - \left(\frac{\boldsymbol{V_{CH2}}}{\boldsymbol{V_{CH1}}}\right)_{\boldsymbol{Z2}}\right) + \boldsymbol{Z}_2\left(\left(\frac{\boldsymbol{V_{CH2}}}{\boldsymbol{V_{CH1}}}\right)_{\boldsymbol{Z1}} - \left(\frac{\boldsymbol{V_{CH2}}}{\boldsymbol{V_{CH1}}}\right)_{\boldsymbol{Z3}}\right) \\ + \boldsymbol{Z}_3\left(\left(\frac{\boldsymbol{V_{CH2}}}{\boldsymbol{V_{CH1}}}\right)_{\boldsymbol{Z2}} - \left(\frac{\boldsymbol{V_{CH2}}}{\boldsymbol{V_{CH1}}}\right)_{\boldsymbol{Z1}}\right)\end{aligned} \tag{4.33}$$

where $(\boldsymbol{V_{CH2}/V_{CH1}})_{\boldsymbol{Z1}}$, $(\boldsymbol{V_{CH2}/V_{CH1}})_{\boldsymbol{Z2}}$, and $(\boldsymbol{V_{CH2}/V_{CH1}})_{\boldsymbol{Z3}}$ are measured VVRs for $\boldsymbol{Z_1}$, $\boldsymbol{Z_2}$ and $\boldsymbol{Z_3}$ at *l*-*l'*, respectively. Note that the $\boldsymbol{h_1}$ and $\boldsymbol{h_2}$ have units of Ω, and $\boldsymbol{h_3}$ is unitless. Similar to the FD error analysis, the systematic errors in the measured VVR are also canceled out during the pre-measurement characterization process.

4.2 Multitone Excitation Signal Synthesis

The excitation signal can be either a single-tone sinusoid or sweeping sinusoid within the frequency range of interest. However, the true potential of the TD-based instrumentation is its

flexibility to excite the SUT with a multitone signal. The multitone signal excitation can drastically improve the measurement speed in comparison to other types of excitation signals due to reduced dead time and settling time [61]–[63]. A multitone signal can be synthesized with an arbitrary frequency and power spectra according to the required measurement specifications, such as the SNR. If no prior knowledge of the SUT is available, it is common to choose a linearly (equidistant) or logarithmically placed frequency spectrum with equal power distribution across the tones [64], [65]. A logarithmic distribution allows the excitation signal to cover several decades of frequency range with a limited number of spectral components [66]. If a linear placement of the excitation signal frequency components across the considered frequency range is desired, the synthesis methods explained in [67], [68] can be used with the drawback of losing resolution for a wider frequency range or else it needs a large number of excitation frequencies resulting in a poor SNR due to the limited power per excitation frequency component [69].

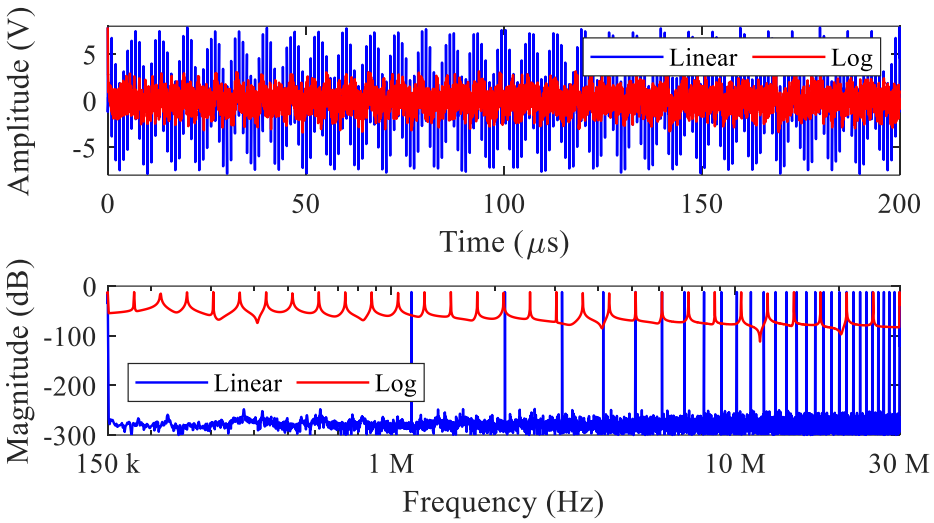

Fig. 4-4. Comparison of excitation signals with a linear and a log frequency distribution in TD and FD.

Fig. 4-4 shows two signals in the TD and FD with linear and logarithmic spectral distributions with 31 spectral components ranging from 150 kHz to 30 MHz, respectively. The

logarithmic distribution suffers from spectral leakage in a DSP stage and hence the noise floor is higher in contrast to the linear spectral distribution. Therefore, logarithmic multitone signal synthesis with minimum spectral leakage is proposed and discussed in this section.

A logarithmic multitone signal with N frequency components has the following relationship,

$$f_n = \alpha f_{n-1} \tag{4.34}$$

where $n = 1, 2, 3, \dots, N$ and $\alpha > 1$ and f_n denotes the n^{th} frequency component. Once N, f_1 and f_N are defined, α can be determined by:

$$\alpha = 10^{\frac{\log\left(\frac{f_N}{f_1}\right)}{N-1}} \tag{4.35}$$

Once α is obtained, f_n can be generated for $n = 1, 2, 3, \dots, N$ using (4.34). However, these frequencies are not guaranteed to fit into an inverse DFT bin in a synthesis stage or into a DFT bin in the DSP stage, and thereby deteriorates the SNR due to spectral leakage. If the above-generated frequencies are aligned with the nearest DFT bin of a DSP stage, the excitation signal is called to have a quasi-logarithmic spectral distribution. Hence (4.34) is approximately valid [70] where:

$$f_n \approx \alpha f_{n-1} \tag{4.36}$$

under the constraint:

$$f_n = H\frac{F_s}{K} \tag{4.37}$$

where F_s is the sampling rate, K is the number of samples, and $H \in \mathbb{N}$ [71].

Multitone signal synthesis requires another consideration, which is the phase relationship among the sinusoidal frequency components. The phase relationship should be selected to minimize the crest factor of the excitation signal. The crest factor describes the required maximum amplitude of the excitation signal for a given power distribution among the

frequency components. This allows maximizing the excitation signal power with limited amplitude [63]. It is advantageous both in the signal synthesis stage as well as the signal analysis stage for the actual impedance measurement. Such a signal can outperform other types of excitation signals at low SNR conditions for a given number of effective bits of the analog to digital converters used for time-domain data acquisition [63]–[65].

Consider the discrete multitone signal x_n with K number of frequency components where a_k, f_k and ϕ_k are the magnitude, frequency, and phase of the k^{th} frequency component, respectively. x_n can be expressed in the following form [62].

$$x_n = \sum_{k=1}^{K} a_k \cos\left(2\pi f_k \frac{n}{N} + \phi_k\right) \tag{4.38}$$

where N is the total number of samples in x_n and $n = 0,1,2,\dots,(N-1)$. The discrete-time crest factor CF of x_n is defined as [62],

$$CF = \frac{\max|x_n|}{\sqrt{\frac{1}{N}\sum_{n=0}^{N-1} x_n^2}} = \frac{\max|x_n|}{\sqrt{\sum_{k=1}^{K} \frac{a_k^2}{2}}} = \frac{\max|x_n|}{\sqrt{\sum_{k=1}^{K} p_k}} \tag{4.39}$$

where a_k and p_k are the amplitude and the power of the k^{th} sinusoidal component, respectively. For $x_n$with unity power to obtain normalized power spectrum:

$$\sum\nolimits_{k=1}^{K} p_k = 1 \tag{4.40}$$

Once an equal power distribution among the frequency components is considered as no prior knowledge of the SUT is assumed [64]:

$$p_k = 1/K \tag{4.41}$$

To this end, a_k can be determined by:

$$a_k = \sqrt{2p_k} \tag{4.42}$$

ϕ_k is determined firstly by the Schroeder method and iteratively optimized such that a lower CF is achieved [62]. Fig. 4-5 shows the quasi-logarithmic excitation signal synthesized by the explained approach with 31 spectral components ranging from 150 kHz to 30 MHz. This signal can be generated by the AWG and injected into the SUT through the inductive probe.

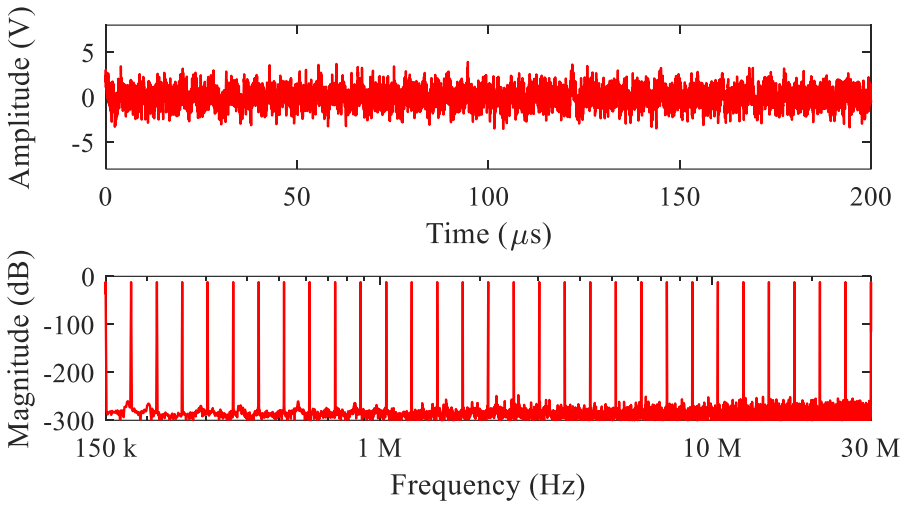

Fig. 4-5. Quasi-log multitone test signal in TD and FD.

4.3 Short-Time Discrete Fourier Transform

The short-time Fourier transform (STDFT) can be adopted for the time-frequency analysis of discrete signals. Therefore, it is chosen to convert the TD signals v_{CH1} and v_{CH2} to FD spectral components $\boldsymbol{V_{CH1}}$ and $\boldsymbol{V_{CH2}}$. This allows time-variant in-circuit impedance measurement to be discussed later. Under STDFT, a suitable trade-off between frequency and time localizations must be selected according to the application specifications. By borrowing the notation given in [71], and (4.9), STDFT can be defined for real and time-limited v_{CH1} and v_{CH2} as follows:

$$\boldsymbol{V_{CH1}}[\omega, q] = \sum_{n=1}^{K} w[n] v_{CH1}[n + Hq] e^{-j2\pi \frac{\omega n}{K}} \tag{4.43}$$

$$\boldsymbol{V_{CH2}}[\omega, q] = \sum_{n=1}^{K} w[n] v_{CH2}[n + Hq] e^{-j2\pi \frac{\omega n}{K}} \tag{4.44}$$

where v_{CH1} and v_{CH2} are the TD signals measured at CH1 and CH2, and then discretized and digitized by the ADC. The local time index relative to the analysis window is $n \in \{1,2,3, \dots, K\}$ and the window length $K \in \mathbb{N}$. The analysis frame index is $q \in \mathbb{N}$. $H \in \mathbb{N}$ is the time advancement from the current analysis frame to the next analysis frame given as the number of samples which can be alternatively expressed as the number of overlapping samples. $\mathbb{N}$ is the total number of samples in the acquired discrete signals v_{CH1} and v_{CH2}. A time-limited window function $w[n]$ is used to minimize spectral leakage. $\omega \in \{1,2,3, \dots, K\}$ and ω denotes the frequency localization of $\boldsymbol{V_{CH1}}$ and $\boldsymbol{V_{CH2}}$ in the discrete FD where the linear frequency $f = \omega f_s / K$. The time localization of $\boldsymbol{V_{CH1}}$ and $\boldsymbol{V_{CH2}}$ is represented in terms of the analysis frame index q. Let F_s be sample rate of the data acquisition and the continuous-time $t = qH/F_s$. The time resolution of the analysis is H/F_s and the frequency resolution is F_s/K. $\boldsymbol{V_{CH1}}$ and $\boldsymbol{V_{CH2}}$ are complex-valued sequences as v_{CH1} and v_{CH2} are real-valued sequences. From (4.43) and (4.44), time-frequency localized VVR ($\boldsymbol{V_{CH2}}[\omega, q]/\boldsymbol{V_{CH1}}[\omega, q]$) is computed to calculate time-variant impedance using (4.45).

$$\boldsymbol{Z_c}[\omega, q] = \frac{\boldsymbol{k_1}[\omega] \left(\frac{\boldsymbol{V_{CH2}}[\omega, q]}{\boldsymbol{V_{CH1}}[\omega, q]} \right) + \boldsymbol{k_2}[\omega]}{\left(\frac{\boldsymbol{V_{CH2}}[\omega, q]}{\boldsymbol{V_{CH1}}[\omega, q]} \right) + \boldsymbol{k_3}[\omega]} \tag{4.45}$$

The signal synthesis that provides excitation, TD signal acquisition, signal processing, pre-measurement characterization, and time-variant impedance measurement are illustrated in the flowchart shown in Fig. 4-6.

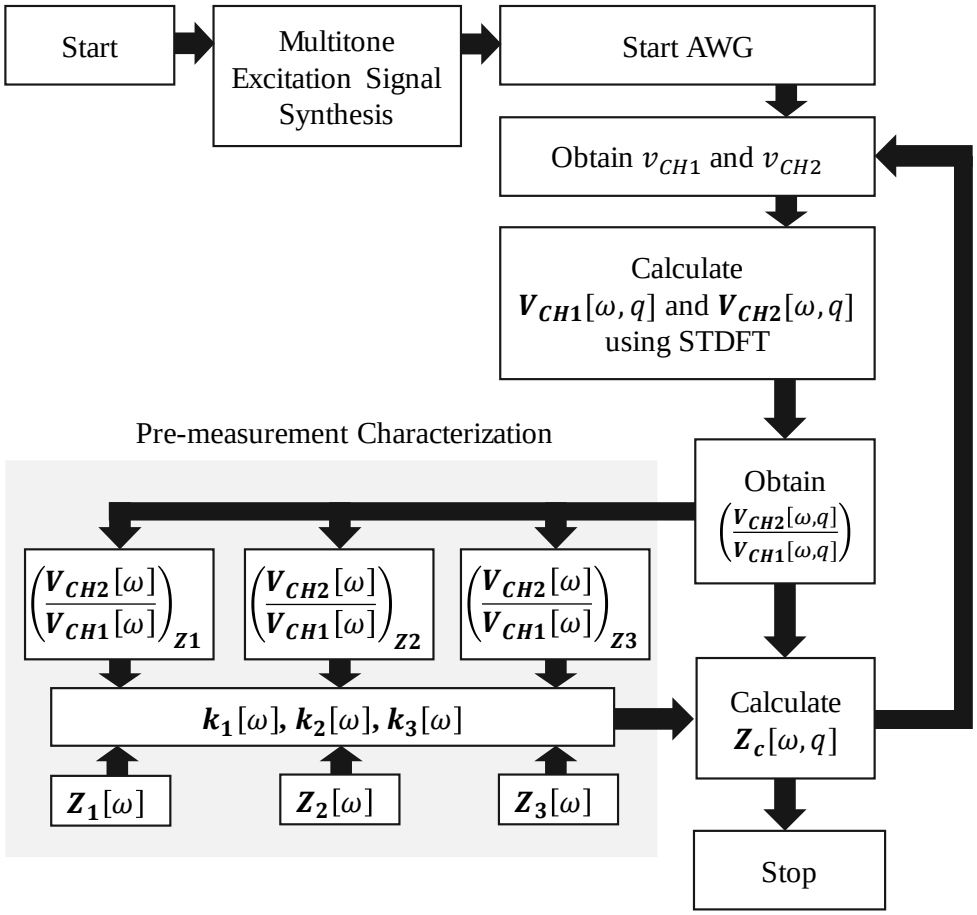

Fig. 4-6. Flowchart for signal synthesis that provides excitation, TD signal acquisition, signal processing, pre-measurement characterization and time-variant impedance measurement.

4.4 Experimental Validation

Fig. 4-7 shows the SPS for experimental validation with the intention to measure the time-invariant unknown in-circuit impedance $\boldsymbol{Z_L}$. The TD-based instrumentation comprises an SGAS with a two-channel oscilloscope module (National Instruments PXI-5142) and a direct digital synthesis AWG (National Instruments PXI-5412). The oscilloscope terminates the directional coupler outputs with 50 Ω. The selected sampling rate is 100 MHz. A multitone signal with 31 spectral components from 150 kHz – 30 MHz produced by the AWG is injected into the SUT through the directional coupler.

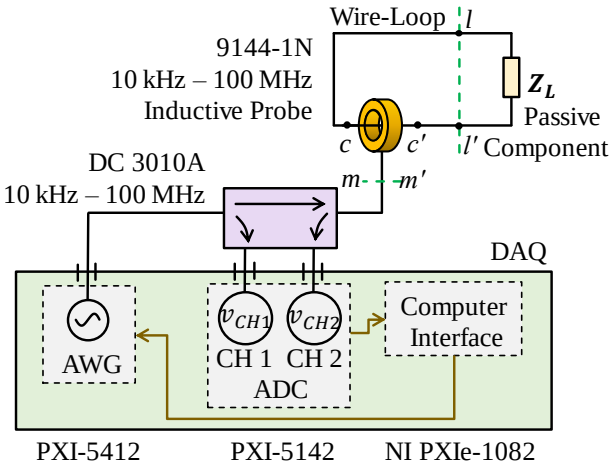

Fig. 4-7. SPS with TD-based instrumentation.

To perform the pre-measurement characterization, the open, short, and 50 Ω load (OSL) conditions are chosen as distinct impedances at *l*-*l′* and the respective VVRs are shown in Fig. 4-8 from 150 kHz – 30 MHz. Since the open and short conditions are adopted, (4.45) can be simplified further. Let $\boldsymbol{Z_1}$, $\boldsymbol{Z_2}$ and $\boldsymbol{Z_3}$ be open, short, and 50 Ω load. Then $\boldsymbol{Z_2} = 0$ Ω and $\boldsymbol{Z_3} = 50$ Ω and the limiting value of (4.45) when $\boldsymbol{Z_1}$ approaches infinite impedance becomes the measured impedance.

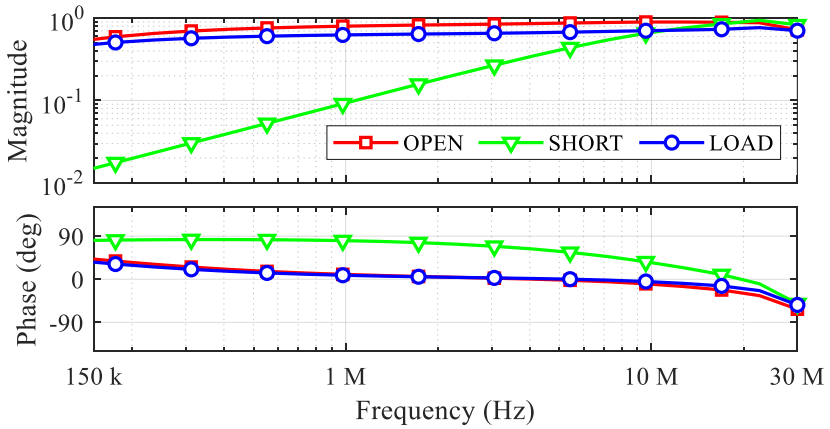

Fig. 4-8. VVRs of the SPS during the pre-measurement characterization.

The relationship given in (4.45) can be rewritten by substituting $\boldsymbol{Z_2}$ = 0 and $\boldsymbol{Z_3} = 50$ W into (4.45):

$$\boldsymbol{Z_c}[\omega] = \lim_{\boldsymbol{Z_1}\to\infty} 50\frac{\boldsymbol{U}-\boldsymbol{V}}{\boldsymbol{W}+\frac{1}{\boldsymbol{Z_1}}\boldsymbol{X}} \tag{4.46}$$

where

$$\mathbf{U} = \left(\frac{\boldsymbol{V_{CH2}}[\omega]}{\boldsymbol{V_{CH1}}[\omega]}\right)\left(\left(\frac{\boldsymbol{V_{CH2}}[\omega]}{\boldsymbol{V_{CH1}}[\omega]}\right)_{\boldsymbol{Z1}} - \left(\frac{\boldsymbol{V_{CH2}}[\omega]}{\boldsymbol{V_{CH1}}[\omega]}\right)_{\boldsymbol{Z3}}\right) \tag{4.47}$$

$$\boldsymbol{V} = \left(\frac{\boldsymbol{V_{CH2}}[\omega]}{\boldsymbol{V_{CH1}}[\omega]}\right)_{\boldsymbol{Z2}}\left(\left(\frac{\boldsymbol{V_{CH2}}[\omega]}{\boldsymbol{V_{CH1}}[\omega]}\right)_{\boldsymbol{Z1}} - \left(\frac{\boldsymbol{V_{CH2}}[\omega]}{\boldsymbol{V_{CH1}}[\omega]}\right)_{\boldsymbol{Z3}}\right) \tag{4.48}$$

$$\boldsymbol{W} = \left(\left(\frac{\boldsymbol{V_{CH2}}[\omega]}{\boldsymbol{V_{CH1}}[\omega]}\right) - \left(\frac{\boldsymbol{V_{CH2}}[\omega]}{\boldsymbol{V_{CH1}}[\omega]}\right)_{\boldsymbol{Z1}}\right)\left(\left(\frac{\boldsymbol{V_{CH2}}[\omega]}{\boldsymbol{V_{CH1}}[\omega]}\right)_{\boldsymbol{Z2}} - \left(\frac{\boldsymbol{V_{CH2}}[\omega]}{\boldsymbol{V_{CH1}}[\omega]}\right)_{\boldsymbol{Z3}}\right) \tag{4.49}$$

$$\boldsymbol{X} = \left(\left(\frac{\boldsymbol{V_{CH2}}[\omega]}{\boldsymbol{V_{CH1}}[\omega]}\right)_{\boldsymbol{Z1}} - \left(\frac{\boldsymbol{V_{CH2}}[\omega]}{\boldsymbol{V_{CH1}}[\omega]}\right)_{\boldsymbol{Z2}}\right)\left(\left(\frac{\boldsymbol{V_{CH2}}[\omega]}{\boldsymbol{V_{CH1}}[\omega]}\right) - \left(\frac{\boldsymbol{V_{CH2}}[\omega]}{\boldsymbol{V_{CH1}}[\omega]}\right)_{\boldsymbol{Z3}}\right) \tag{4.50}$$

When $\boldsymbol{Z_1} \to \infty$, (4.46) becomes:

$$\boldsymbol{Z_c}[\omega] = 50\frac{\boldsymbol{U}-\boldsymbol{V}}{\boldsymbol{W}} \tag{4.51}$$

The results obtained from the above-described method are shown in Fig. 4-9, Fig. 4-10, and Fig. 4-11 for three types of passive loads: resistors (2 Ω, 100 Ω and 3 kΩ), inductors (1 µH, 10 µH, 100 µH, and 1 mH) and capacitors (1 nF, 10 nF, 100 nF, and 1 µF), respectively. The reference impedances are obtained by off-circuit impedance measurement using an IA. The measured impedance responses agree well with the reference impedance responses.

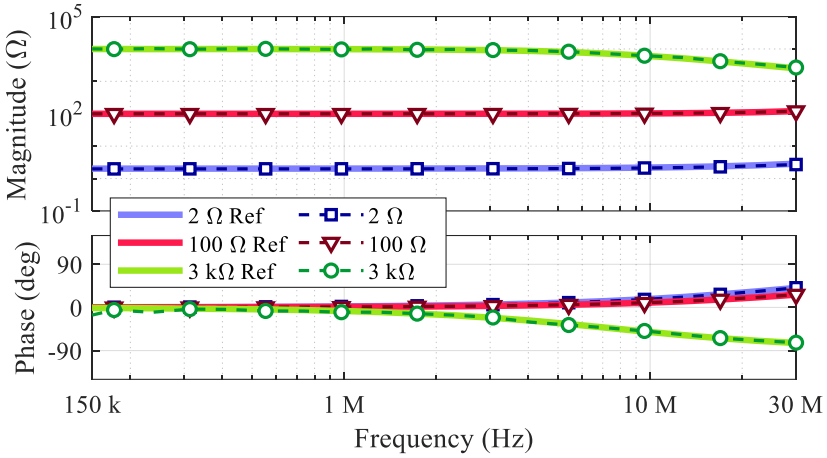

Fig. 4-9. Impedance responses of resistors measured with TD-based instrumentation after signal processing in comparison to reference impedance responses.

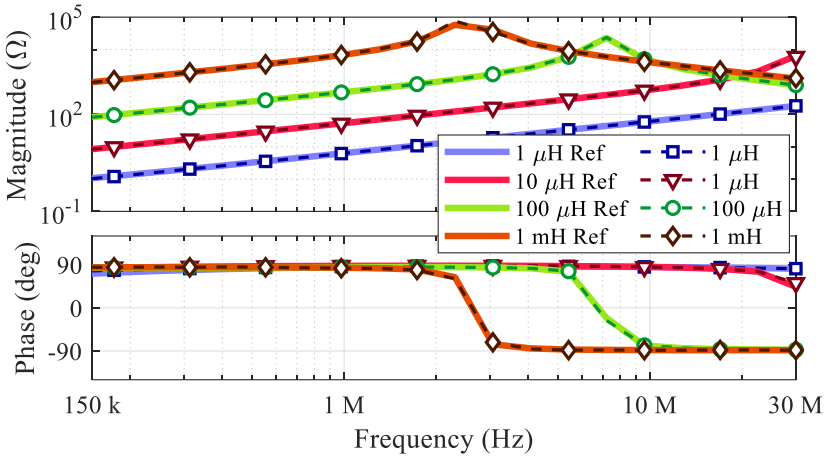

Fig. 4-10. Impedance responses of inductors measured with TD-based instrumentation after signal processing in comparison to reference impedance responses

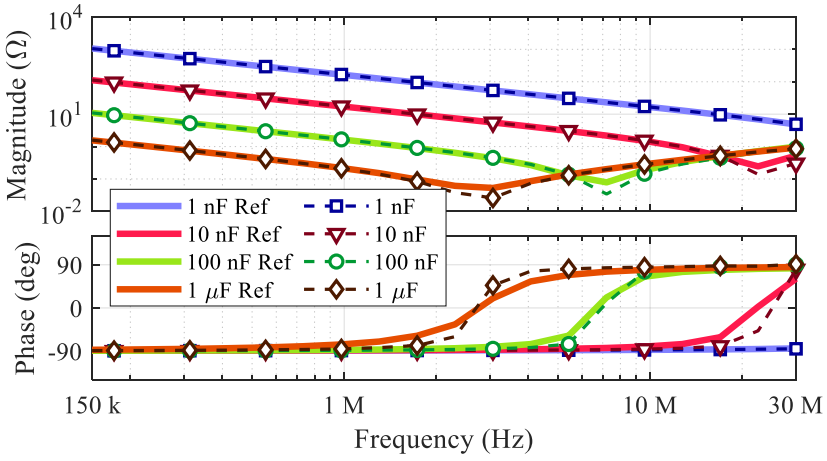

Fig. 4-11. Impedance responses of capacitors measured with TD-based instrumentation after signal processing in comparison to reference impedance responses.

Fig. 4-12 shows the SPS with the details of the TD-based instrumentation for experimental validation with the objective to measure a time-variant unknown impedance $\boldsymbol{Z_L}[\omega, q]$. The time-variant load is emulated by switching it to $\boldsymbol{Z_{L1}}$, $\boldsymbol{Z_{L2}}$, and $\boldsymbol{Z_{L3}}$ through a timed relay mechanism at $t = 10$ ms, $t = 30$ ms and $t = 50$ ms, respectively. $\boldsymbol{Z_{L1}}$, $\boldsymbol{Z_{L2}}$, and $\boldsymbol{Z_{L3}}$ are a combination of various RLC components in series. $\boldsymbol{Z_{L1}}$ is a 50 Ω resistor, a 3 nH inductor, and a 0.1 µF capacitor. $\boldsymbol{Z_{L2}}$ is a 25 Ω resistor, a 3 nH inductor, and a 0.1 µF capacitor. $\boldsymbol{Z_{L3}}$ is a 50 Ω resistor and a 0.1 µF capacitor. The selected sampling rate is 100 MHz, the DSP STDFT analysis window size is 100k samples and the time advancement is 100k samples. Therefore, the time resolution of the analysis is 1 ms and the frequency resolution is 1 kHz. A multitone signal with 51 spectral components from 150 kHz – 30 MHz produced by the AWG is injected into the SUT through the directional coupler. The pre-measurement characterization is performed at *l*-*l′* with OSL termination conditions. Fig. 4-13 shows the comparison of the measured time-variant impedance using the SPS with the reference measurements obtained offline with an IA. Table 4-1 gives a statistical overview of the measurement results.

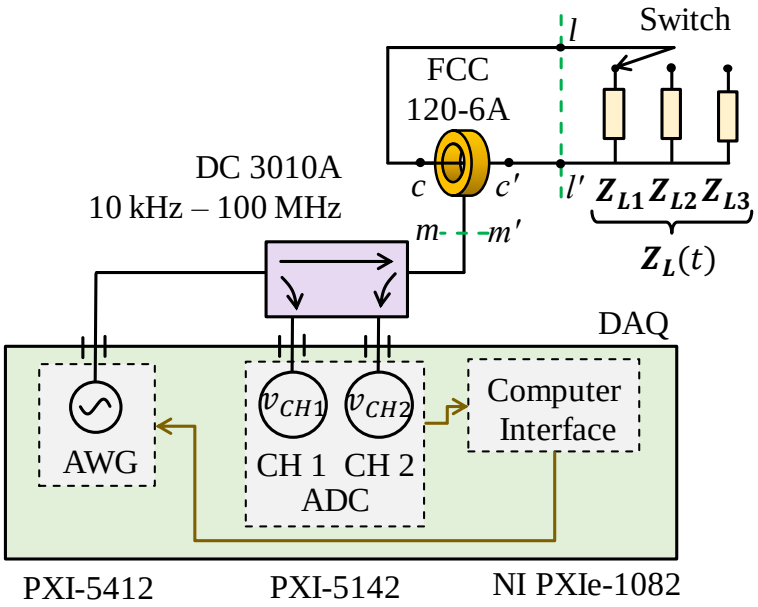

Fig. 4-12. SPS with TD-based instrumentation for in-circuit time-variant impedance measurement.

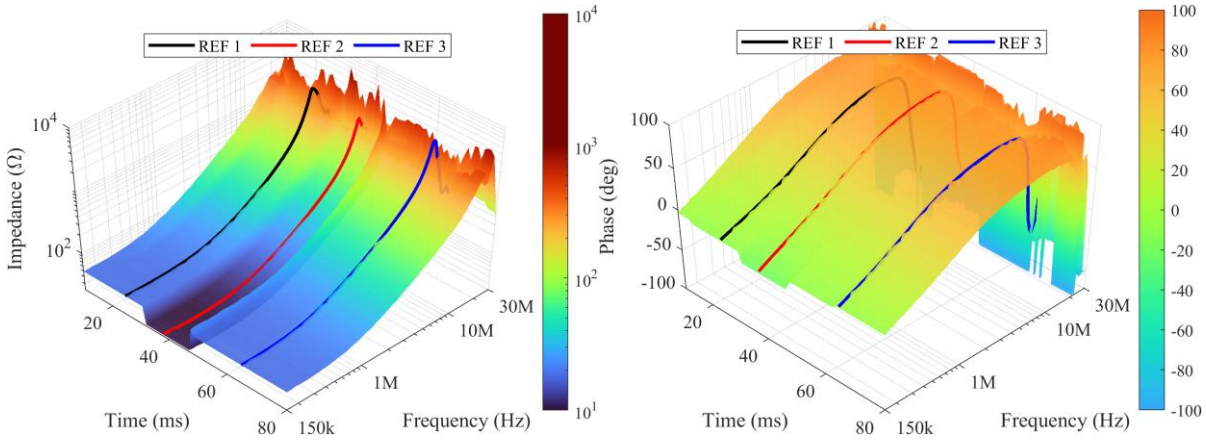

(a) (b)

Fig. 4-13. Time-varying impedance measurement results (a) magnitude (b) phase.

Table 4-1. Statistical Comparison of time-variant impedance measurement.

Z_L	Frequency (Hz)	REF	Mean	Standard Deviation	Error
$\|Z_{L1}\|$ (Ω)	150k	49.4	49.35	0.045	0.1 %
	1M	60.5	68.3	7.70	-12.9 %
	10M	461.6	522.9	115.1	-13.3 %
	30M	741.2	518.9	73.0	30.0 %
$\angle Z_{L1}$(°)	150k	-5.9	-6.0	1.9	0.1 °
	1M	34.2	41.0	6.9	-6.8 °
	10M	75.7	79.1	1.8	-3.4 °
	30M	-64.5	-74.8	7.4	10.3 °
$\|Z_{L2}\|$(Ω)	150k	25.9	25.4	0.02	1.9 %
	1M	29.8	29.7	0.01	0.3 %
	10M	205.2	197.4	0.84	3.8 %
	30M	730.1	651.9	57.9	10.7 %
$\angle Z_{L2}$ (°)	150k	-17.4	-6.5	0.02	-10.9 °
	1M	33.1	39.5	0.03	-6.4 °
	10M	78.3	79.2	0.5	-0.9 °
	30M	-54.6	-77.7	4.6	23.1 °
$\|Z_{L3}\|$(Ω)	150k	49.37	49.4	0.06	-0.1 %
	1M	75.3	66.4	7.33	11.8 %
	10M	708.4	495.3	111.95	30.1 %
	30M	413.6	513.0	53.63	-24.0 %
$\angle Z_{L3}$ (°)	150k	-5.9	-20.4	1.9	14.5 °
	1M	33.9	34.3	6.5	-0.4 °
	10M	73.7	79.2	2.0	-5.5 °
	30M	-62.2	-79.3	7.9	17.1 °

From Table 4-1 it is evident that above 10 MHz the measurement uncertainty is significantly higher. It is expected as the resonance frequency of the SUTs occurs in the 10 MHz – 30 MHz frequency range where the impedance of the SUT is very large and exceeds the dynamic range of the measurement setup. Below 10 MHz, about 10 % magnitude error can be maintained and the measurement uncertainty is very small as the SUT impedance is well within the dynamic range of the setup.

4.5 Discussion and Summary

The basic principle behind the SPS with TD-based instrumentation has been described. By adopting a quasi-log crest-factor optimized multitone excitation signal synthesis with a DSP technique, conversion of the measured TD signals to its FD counterparts has been elaborated and explained. Through a pre-measurement characterization, the relationship between the measured impedance and the setup can be established so that any unknown impedance can be measured with ease. The validity of the SPS with TD-based instrumentation is verified experimentally and its ability to measure time-variant impedance is also demonstrated.

Chapter 5 Practical Considerations for the Single-Probe Setup

Transient events and high excitation levels in an energized SUT can cause damage to the sensitive instrumentation. Therefore, protection devices must be incorporated in the SPS for practical applications [72]. This chapter describes the incorporation of protection devices to safeguard the instrumentation against transients and surges in a high voltage and high power energized SUT. In addition, it also elaborates the incorporation of power amplification in the SPS to maintain good SNR for robust and accurate in-circuit impedance measurement for SUT with the presence of strong background noise. To quantify the necessary SNR for good measurement accuracy, a comprehensive analysis is carried out to determine the desired SNR. In the event where high SNR cannot be achieved, an error correction method is developed to enhance the measurement accuracy.

5.1 Signal to Noise Ratio and Measurement Accuracy

Fig. 5-1 shows the setup to evaluate the impact of signal-to-noise ratio (SNR) on the in-circuit impedance measurement accuracy using the proposed SPS. The basic SPS consists of an inductive probe (Solar 9144-1N), a VNA (Bode 100), a pair of wires, and a 100 Ω resistor. The power supply is not included in the SPS to ensure the SNR analysis is not influenced by the noise generated by the power supply.

To emulate the noise signal, a signal generator (National Instruments PXI-5412) and an inductive probe (Tektronix CT1) injects a signal into the setup with known magnitude and

frequency. Another inductive probe (Tektronix CT1) with a spectrum analyzer (R&S FSH4) measures the excitation signal from the VNA and the noise signal from the signal generator. The signal generator is set at three different frequencies, 1 MHz, 5 MHz, and 10 MHz with adjustable signal levels. By measuring the excitation and noise signals separately with the inductive probe and the spectrum analyzer, the SNR can be computed.

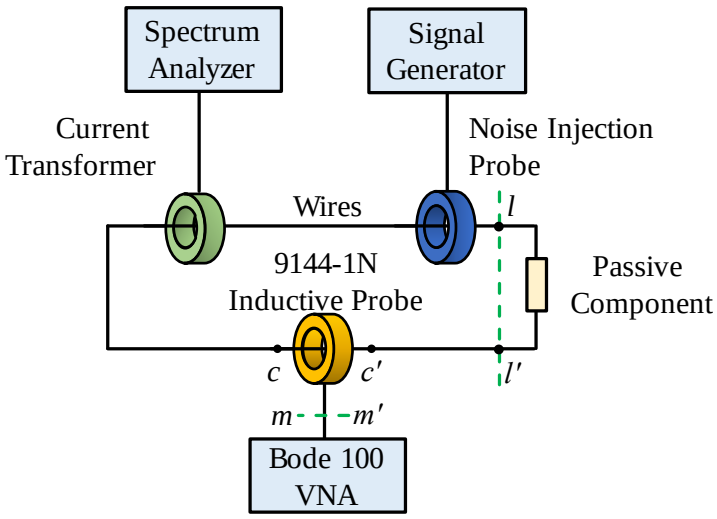

Fig. 5-1. Setup to evaluate the impact of the background noise on SPS measurement accuracy.

The errors of the measured in-circuit impedance with the presence of the emulated noise at 1 MHz, 5 MHz, and 10 MHz are shown in Fig. 5-2 for three different SNRs. It is clearly observed that the higher the SNR, the better is the measurement accuracy. By closely examining Fig. 5-2, it reveals that if SNR is 30 dB or higher, it yields a measurement accuracy with less than 5% magnitude error and less than 2^{o} phase error.

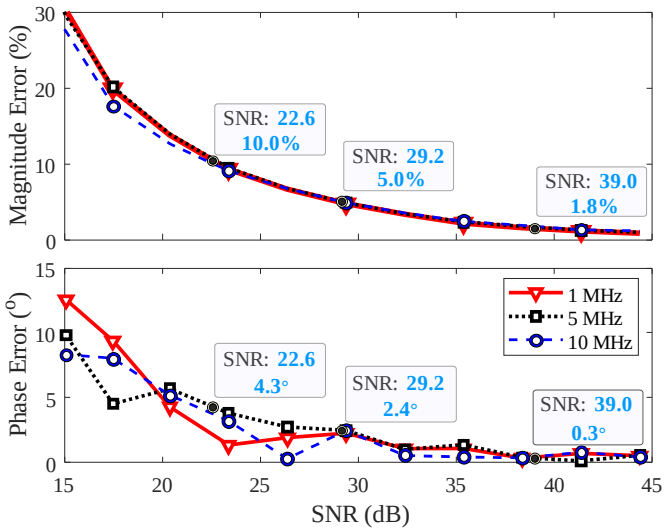

Fig. 5-2. Relationship between the measurement error and the SNR of SPS.

In some situations, where strong background noise is present and the VNA's built-in signal source may not be able to generate a high enough excitation signal to achieve sufficient SNR, an external power amplifier must be added to the SPS to improve its SNR. In addition, protection devices are also added to improve the SPS ruggedness, which will be discussed in the following section.

5.2 Improving SNR and Introducing Protection

To mitigate the concern of insufficient excitation signal level provided by the VNA, Fig. 5-3 shows a VNA-based SPS incorporated with power amplification. To protect the instrumentation from damage, surge protection devices and attenuators are also included in the setup. The excitation signal produced by the VNA is amplified by a power amplifier with a gain $\boldsymbol{A}$. The excitation level can be determined by measuring the noise levels in the energized SUT prior to the actual SPS measurement. The VNA output level should be decided such that the amplifier output can maintain an SNR > 30 dB according to the previous evaluation study. The inductive probe is connected to the directional coupler through a surge protector. Surge

protector guards against any high voltages induced in the inductive probe windings due to surge and transient events in the energized SUT. Two attenuators are used between the directional coupler outputs and the receivers (RX1, RX2) of the VNA to ensure the measured signals are within the permissible range of the VNA receiver input. The VNA and the directional coupler are configured in the reflectometer configuration so that the reflection coefficient at m-m' ($\boldsymbol{\Gamma_m}$) can be measured. With this improved setup, the in-circuit impedance measurement using the SPS can be deployed in practical electrical systems, where surges and transients are present.

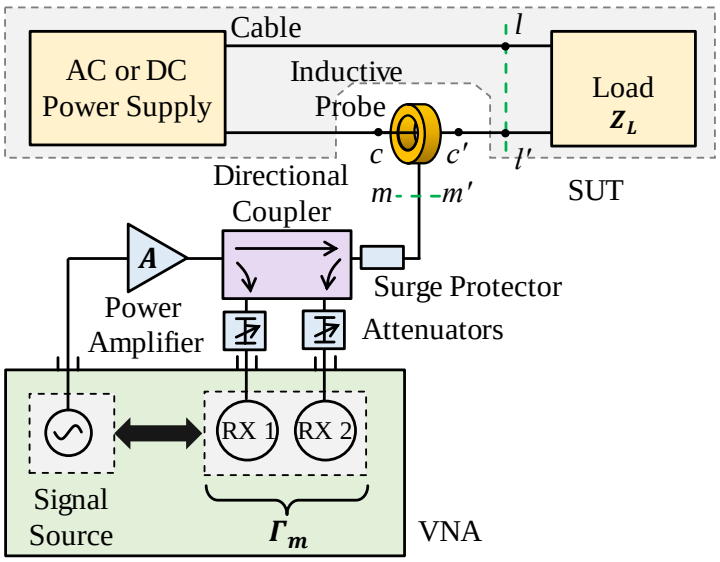

Fig. 5-3. VNA based SPS incorporated with power amplification and protection devices.

The equivalent network representation of the VNA-based SPS incorporated with power amplification and protection devices is shown in Fig. 5-4. I. omprises an RF directional coupler, two attenuators, and a surge protector, which can be considered as a four-port network whose ports are denoted by numbers from 1 to 4. The output reflection coefficient of the power amplifier is $\boldsymbol{\Gamma_A}$ at port 1. The reflection coefficients of the VNA receiver terminations are denoted by $\boldsymbol{\Gamma_{RX1}}$ and $\boldsymbol{\Gamma_{RX2}}$ at port 3 and 4, respectively. Since the VNA can measure $\boldsymbol{\Gamma_m}$, the extraction of $\boldsymbol{Z_c}$ or $\boldsymbol{Z_L}$ stays the same as the VNA-based SPS without the power amplification and protection devices. For further validation in a more realistic condition, the aforementioned

setup is adopted to extract the in-circuit impedance of a 230-V AC induction motor under its operating condition, as described in Section 6.2.

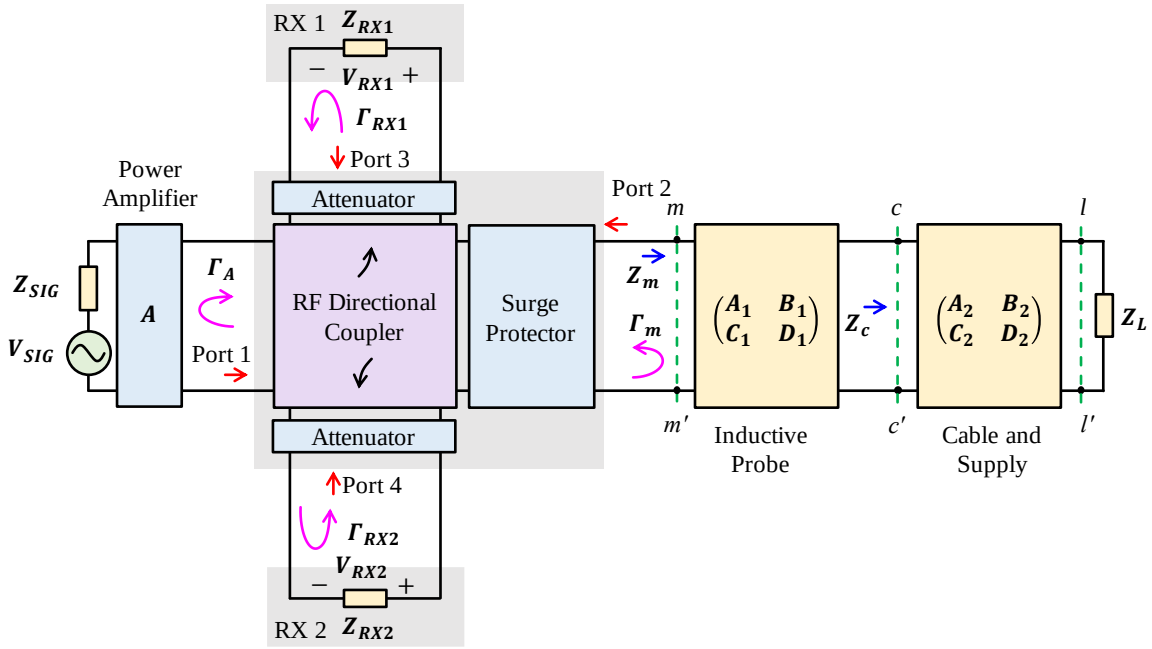

Fig. 5-4. Network representation of VNA based SPS incorporated with power amplification and protection devices.

5.3 Experimental Validation

Fig. 5-5 shows the SPS with signal amplification and surge protection devices incorporated. It consists of a VNA (Bode 100), an inductive probe (F-120-6A), a power amplifier (ZHL-32A-S+), a directional coupler (DC-3010A), two attenuators (DWZ P78), and a surge protector (LCSP 1049). Fig. 5-6 shows the measured in-circuit impedance responses of resistors (10 Ω and 5 kΩ) and capacitors (1 nF and 10 nF) powered by a DC power supply. The impedance responses of the same passive components are measured offline using an IA as references for comparison. The measured impedance responses from 150 kHz to 30 MHz are in good agreement with those of the references.

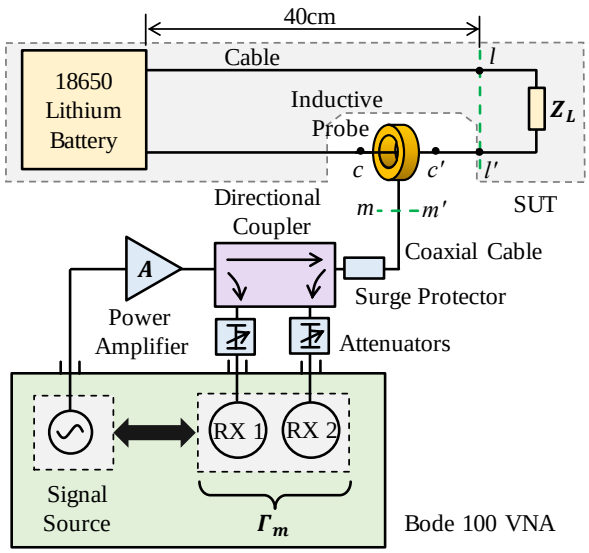

Fig. 5-5. Setup for experimental validation incorporating power amplification and protection devices.

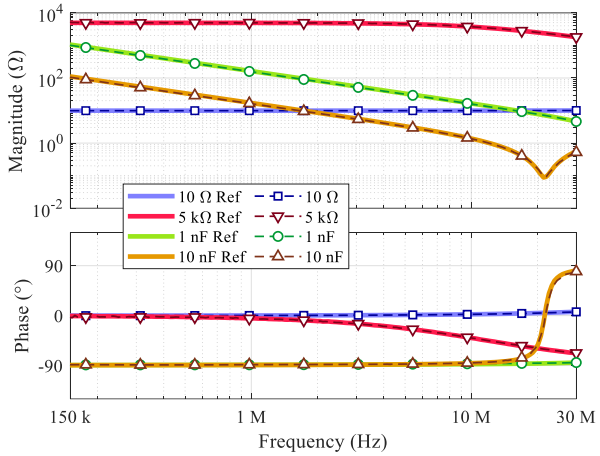

Fig. 5-6. Comparison of measured and reference impedances of passive devices using the VNA based improved SPS.

5.4 Error Correction Scheme

Statistical error correction methods are widely adopted for measurement systems with the presence of random noise. However, they are not suitable if the sources of the measurement errors have a strong correlation with the noise signals present in the measurement setup. This section proposes a non-statistical-based error correction approach for eliminating the errors contributed by the presence of noise signals that are correlated to the excitation signals that exist in the energized SUT. The errors resulted are studied and visualized analytically based

on an equivalent circuit of the SPS. The proposed error correction method is verified experimentally.

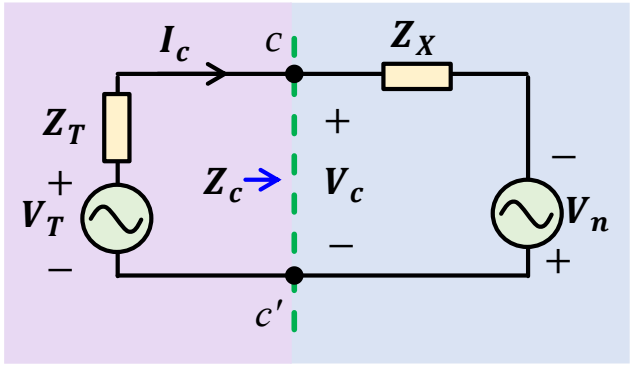

Fig. 5-7. Thevenin equivalent circuit of the SPS with the presence of noise.

Fig. 5-7 shows an equivalent circuit of the SPS shown in Fig. 3-2 including a deterministic noise source. The excitation signal source and the inductive probe can be modeled by and Thevenin voltage $\boldsymbol{V_T}$ and impedance $\boldsymbol{Z_T}$ and at *c*-*c*′. The noise in the energized SUT is denoted by $\boldsymbol{V_n}$. $\boldsymbol{V_n}$ and $\boldsymbol{V_T}$ are both vector quantities. The equivalent impedance of the SUT including $\boldsymbol{Z_L}$, $\boldsymbol{Z_{W1}}$, $\boldsymbol{Z_{W2}}$ and $\boldsymbol{Z_S}$. For simplicity, they are lumped together and represented by $\boldsymbol{Z_X}$. Through circuit analysis:

$$\boldsymbol{Z_c} = \boldsymbol{Z_X} - \frac{\boldsymbol{Z_X}}{\boldsymbol{SNR}+1} - \frac{\boldsymbol{Z_T}}{\boldsymbol{SNR}+1} \tag{5.1}$$

where $\boldsymbol{SNR} = \boldsymbol{V_T}/\boldsymbol{V_n}$, $|\boldsymbol{SNR}| \in \mathbb{R}^+$, $|\boldsymbol{SNR}| \neq 1$, and $0 < \angle\boldsymbol{SNR} \leq 2\pi$.

Equation (5.1) describes the expected measurement result with the presence of a noise signal. Besides $\boldsymbol{Z_X}$, it comprises of a proportional error $\boldsymbol{Z_X}/(\boldsymbol{SNR}+1)$ and an offset error $\boldsymbol{Z_T}/(\boldsymbol{SNR}+1)$. The proportional error is related to the equivalent impedance of the SUT ($\boldsymbol{Z_X}$), whereas the offset error is independent of $\boldsymbol{Z_X}$ but is influenced by the Thevenin equivalent impedance of the measurement setup ($\boldsymbol{Z_T}$). B. bserving (5.1), both proportional and offset errors diminish when $|\boldsymbol{SNR}| \to \infty$. Under the situation when the measured in-circuit impedance is small for a given $|\boldsymbol{SNR}|$, the offset error dominates. On the other hand, when the

measured in-circuit impedance is large for a given $|\boldsymbol{SNR}|$, the proportional error dominates. Also, a good excitation source with high $\boldsymbol{V_T}$ and small $\boldsymbol{Z_T}$, a better measurement accuracy is expected. From (5.1), for a given $|\boldsymbol{SNR}|$ the trajectory of $\boldsymbol{Z_c}$ with respect to $\angle\boldsymbol{SNR}$ can be approximated by a circle.

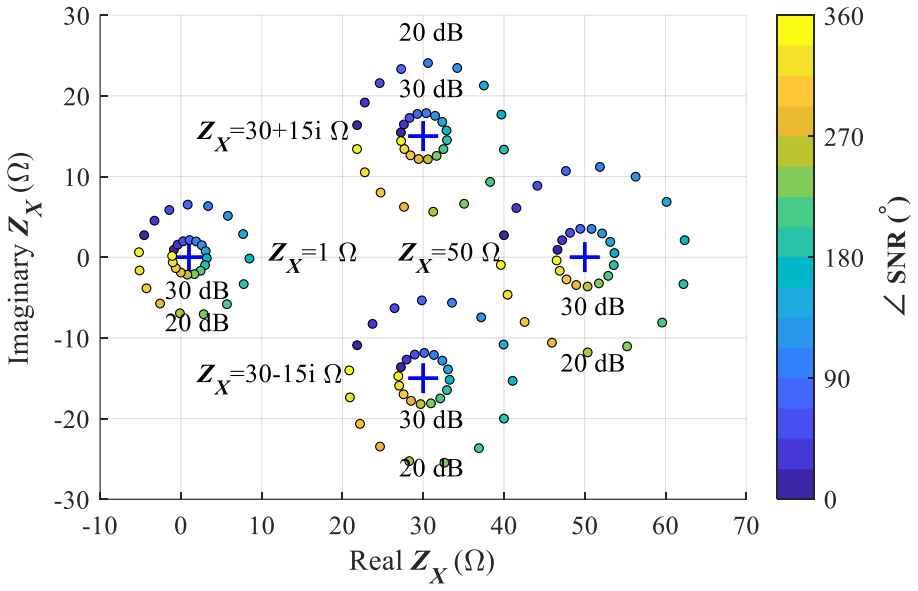

Fig. 5-8 Simulated $\boldsymbol{Z_c}$ at different $|\boldsymbol{SNR}|$ with varying $\angle\boldsymbol{SNR}$ (refer to vertical color bar) with reference $\boldsymbol{Z_X}$ (blue crosses).

Fig. 5-8 illustrates the simulated $\boldsymbol{Z_c}$ using (5.1) in the complex impedance plane for four different $\boldsymbol{Z_X}$ (1 Ω, 50 Ω, 30 + 15j Ω, and 30-15j Ω) at $|\boldsymbol{SNR}|$= 20 dB and $\boldsymbol{SNR}|$ = 30 dB, where $\angle\boldsymbol{SNR}$ ranges from 0° to 360°. $\boldsymbol{Z_X}$ is indicated as a blue cross. For $|\boldsymbol{SNR}|$ = 20 dB, the simulated $\boldsymbol{Z_c}$ exhibits larger deviation as compared to that of $|\boldsymbol{SNR}|$= 30 dB. The deviation is circularly distributed around $\boldsymbol{Z_X}$. It is clearly observed that the circle radius is inversely proportional to the $|\boldsymbol{SNR}|$.

This behavior can be further analyzed by using the simulated $\boldsymbol{Z_c}$ for $\boldsymbol{Z_X}$ = 30+60j Ω with $|\boldsymbol{SNR}|$ = 6 dB, 10 dB and 15 dB, as shown in Fig. 5-9. $\boldsymbol{Z_X}$ is indicated as a blue cross and the simulated $\boldsymbol{Z_c}$ is distributed as circles around $\boldsymbol{Z_X}$. The centers of the three circles C_1, C_2, and C_3 correspond to $|\boldsymbol{SNR}|$ = 6 dB, 10 dB, and 15 dB, respectively. Note that these centers deviate

from the reference $\boldsymbol{Z_X}$. It can be seen that the higher the $|\boldsymbol{SNR}|$, the closer the center converges towards $\boldsymbol{Z_X}$ and the error radius becomes smaller. It is also observed that three centers and $\boldsymbol{Z_X}$ lie on a straight line indicated by a black straight line.

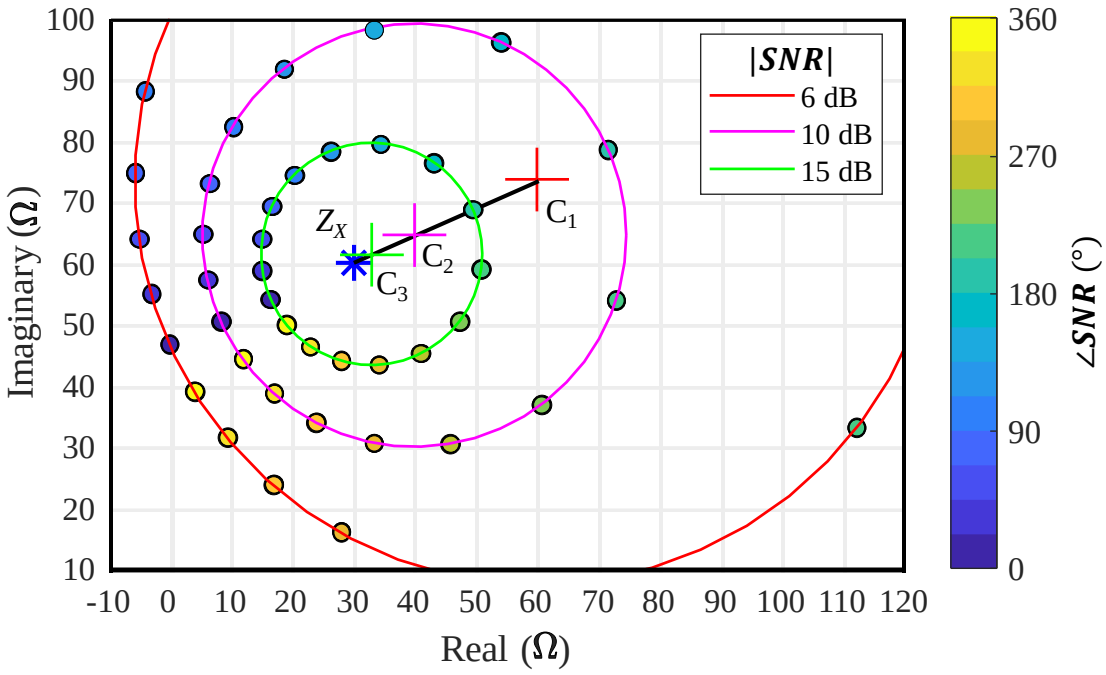

Fig. 5-9. Simulated $\boldsymbol{Z_c}$ for $\boldsymbol{Z_X}$=30+100j Ω at $|\boldsymbol{SNR}|$ = 6 dB, 10 dB and 15 dB with varying $\angle\boldsymbol{SNR}$

To verify the validity of the error analysis, the measurement setup shown in Fig. 5-1 is adopted with a passive load of 100 Ω resistor. The noise signals at three frequencies, 1 MHz, 3 MHz, and 5 MHz are emulated. By adjusting the VNA signal source output, $|\boldsymbol{SNR}|$ = 6 dB, 10 dB and 15 dB are established. With a large sample of repeated measurements at each $|\boldsymbol{SNR}|$, Fig. 5-10 is plotted. The measured in-circuit impedance without the noise present is shown as a cross for reference. The error circles can be seen clearly and higher $|\boldsymbol{SNR}|$ leads to the error circle converges towards the reference, indicating a higher measurement accuracy.

Instead of taking a large sample of repeated measurement data, it is possible to construct such an error circle for a given $|\boldsymbol{SNR}|$ using three uniquely taken measurement data by mathematically fitting them into a circle.

The coordinates of the center $C \equiv (x_c, y_c)$ and radius r of the circle that passes through the three non-colinear points $P_1 \equiv (x_1, y_1)$, $P_2 \equiv (x_2, y_2)$, and $P_3 \equiv (x_3, y_3)$ can be defined as:

$$x_c = -\frac{B}{2A} \tag{5.2}$$

$$y_c = -\frac{C}{2A} \tag{5.3}$$

$$r = \sqrt{\frac{B^2 + C^2 - 4AD}{4A^2}} \tag{5.4}$$

where,

$$A = x_1(y_2 - y_3) - y_1(x_2 - x_3) + x_2 y_3 - x_3 y_2 \tag{5.5}$$

$$B = (x_1^2 + y_1^2)(y_3 - y_2) + (x_2^2 + y_2^2)(y_1 - y_3) + (x_3^2 + y_3^2)(y_2 - y_1) \tag{5.6}$$

$$C = (x_1^2 + y_1^2)(x_2 - x_3) + (x_2^2 + y_2^2)(x_3 - x_1) + (x_3^2 + y_3^2)(x_1 - x_2) \tag{5.7}$$

$$D = (x_1^2 + y_1^2)(x_3 y_2 - x_2 y_3) + (x_2^2 + y_2^2)(x_1 y_3 - x_3 y_1) + (x_3^2 + y_3^2)(x_2 y_1 - x_1 y_2) \tag{5.8}$$

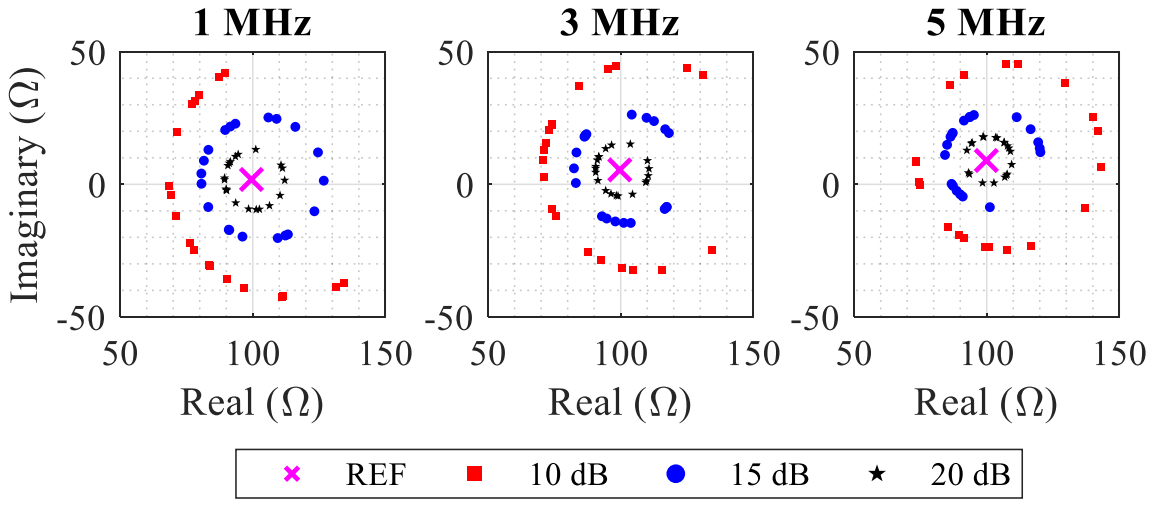

Fig. 5-10. Measurement result distribution in complex plane for a 100 Ω resistor at $|SNR|$= 10 dB, 15 dB and 20 dB at three emulated noise signal frequencies (1 MHz, 3 MHz, and 5 MHz).

Fig. 5-11 shows two circles constructed by fitting the three data points based on the above-mentioned approach under two $|\boldsymbol{SNR}|$ conditions at 1 MHz excitation frequency. The purpose of doing so is to estimate the reference impedance (the impedance without noise presence) by extrapolating the centers of the circles based on the two $|\boldsymbol{SNR}|$ conditions. Different $\boldsymbol{SNR}$ conditions can be emulated by adjusting the excitation signal level. The centers with the extrapolation are visualized in Fig. 5-12. Since the coordinates $C_1 \equiv (x_{C1}, y_{C1})$, $C_2 \equiv (x_{C2}, y_{C2})$ and REF lie on the same line, the line l_1 can be determined using coordinates C_1 and C_2.

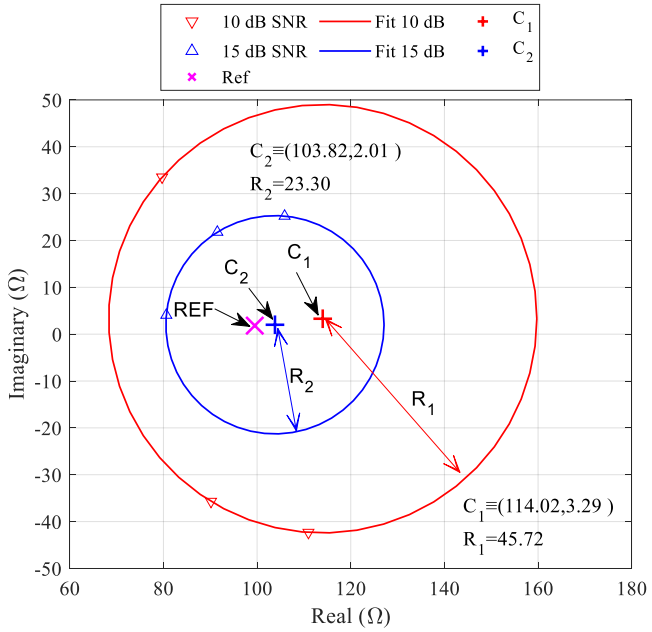

Fig. 5-11. Circles constructed by three consecutive measurements with the presence of noise at $|\boldsymbol{SNR}|$ = 10 dB and 15 dB with respect to the reference value.

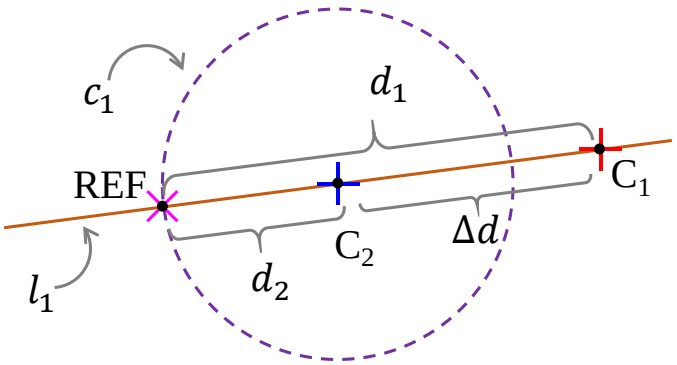

Fig. 5-12. Extrapolation of the coordinates of C_1 and C_2 to estimate the reference value.

The line l_1 is determined by:

$$y = \left(\frac{y_{C2} - y_{C1}}{x_{C2} - x_{C1}}\right) x + y_{C2} - x_{C2}\left(\frac{y_{C2} - y_{C1}}{x_{C2} - x_{C1}}\right) \tag{5.9}$$

Now d_2 can be obtained by:

$$d_2 = \frac{\Delta d}{\frac{|\boldsymbol{SNR_1}|}{|\boldsymbol{SNR_2}|} - 1} \tag{5.10}$$

where $\Delta d = \sqrt{(y_{C2} - y_{C1})^2 + (x_{C2} - x_{C1})^2}$.

Since C_2 and d_2 are known, the circle c_1 can be constructed. By finding the intersection point of the circle c_1 and the line l_1, the value of REF can be estimated.

Fig. 5-13 shows the measured in-circuit impedance without and with applying the error correction method described earlier based on the same setup shown in Fig. 5-1. As observed the error correction method can correct the measurement error due to the presence of noise, which is useful for measurement system with SNR constraints.

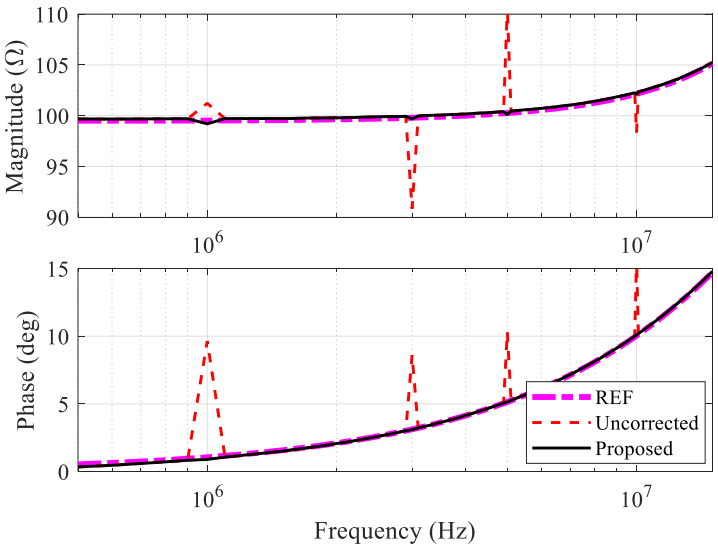

Fig. 5-13. Comparison of corrected and uncorrected measured impedance with respect to the reference.

5.5 Discussion and Summary

Considering the practical application of the SPS, power amplification and protection devices have been incorporated in the basic SPS. The modified SPS has been experimentally validated for in-circuit impedance measurement. A non-statistical error correction method has been proposed to correct measurement error due to the presence of a noise signal that is correlated to the excitation signal, which is also validated experimentally.

Chapter 6 Practical Applications

With the incorporation of power amplification and protection devices in the SPS, this chapter illustrates how to apply it for practical applications. The in-circuit impedance measurement based on the SPS can be used for EMI filter design, condition monitoring, and fault detection purposes.

6.1 Differential-Mode and Common-Mode Impedances of Variable Frequency Drive

The practical test case in this section is to apply the SPS to measure the differential-mode (DM) and common-mode (CM) impedances of a grid-connected variable frequency drive (VFD) system. The VFD system used in this experiment is modified by removing its built-in EMI filter at its AC input. The objective is to extract its CM and DM noise source impedance models. The VFD operates based on voltage-frequency (V/F) and sensor-less vector (SLV) controls. In this practical test case, we investigate the impact of various mode settings on the DM and CM noise source impedances. The VFD speed setting is set to 10 Hz, 30 Hz, and 50 Hz and Table 6-1 lists the details of the VFD and instruments used for the experimental setup.

Table 6-1. Details of the SUT and test instruments.

SUT/ Instrument	Model	Specifications
VFD	TECO L510s	230 VAC 50Hz
Induction Motor	RMS8024/B3	4 pole, 3 Phase, 0.75 kW, 50 Hz
Cables		VFD to Motor: 60 cm LISN to VFD: 100 cm
LISN	Electro-Metrics MIL 5 – 25/2	100 kHz – 65 MHz
Inductive Probe	SOLAR 9144 – 1N	4 kHz – 100 MHz
VNA	Omicron Bode 100	1 Hz – 40 MHz
Power Amplifier	Mini circuits LZY–22+	100 kHz – 200 MHz
Directional Coupler	DC3010A	10 kHz – 1 GHz
Surge Protector	SSC – N230/01	–
Attenuator 1	AIM-Cambridge 27-9300-6	6 dB
Attenuator 2	AIM-Cambridge 27-9300-3	3 dB

6.1.1 Differential-Mode Impedance Extraction

The SPS shown in Fig. 6-1 depicts a VFD connected to an AC power grid through a line impedance stabilization network (LISN). The earth connection has been removed to isolate the CM current path so that its influence on the DM impedance measurement is eliminated. The LISN decouples the power grid impedance variation and blocks unwanted conducted emissions from the power grid. T. VFD output is connected to a 3-phase induction motor. An inductive probe is clamped onto one of the power cables at the location *c*-*c′*. The resultant DM current is denoted as $\boldsymbol{I_{DM}}$. The SPS adopts a FD-based instrumentation with a power amplifier and an RF directional coupler. The power amplifier is needed to ensure good SNR due to the presence of noise generated by the VFD. Two attenuators (ATT) and a surge protector are added to safeguard the VNA should transients happen. r_{L1}, and r_{L2} denote the AC input reference plane of the VFD at which the DM impedance is measured.

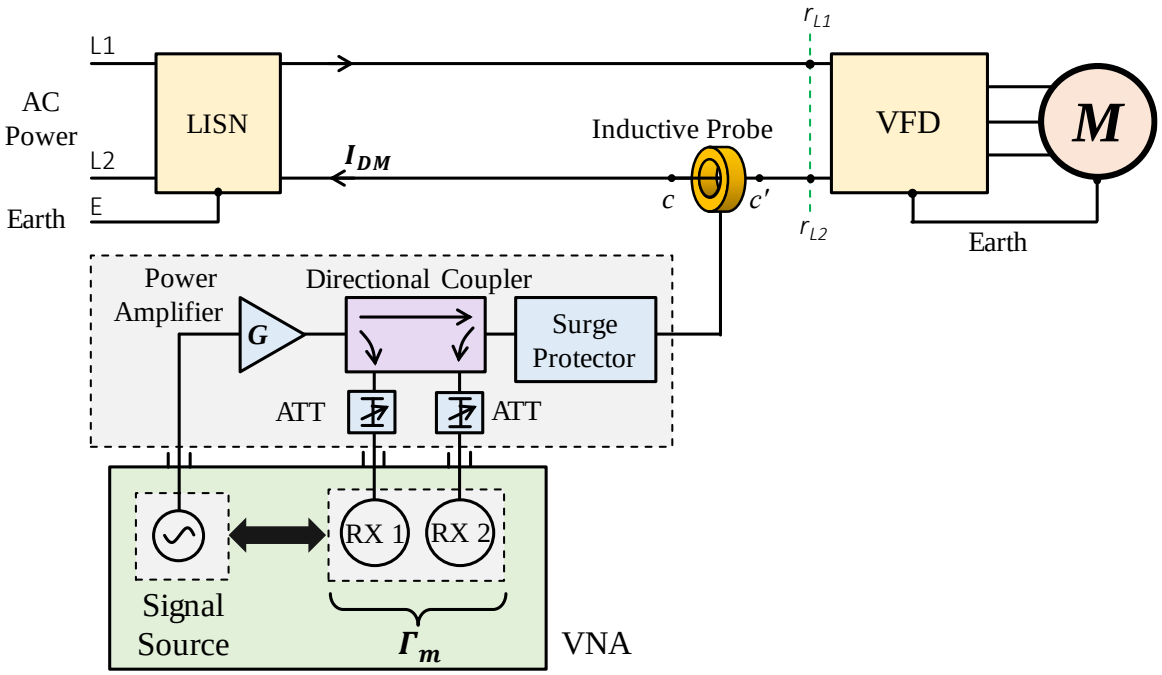

Fig. 6-1. DM impedance measurement of a VFD under operating conditions.

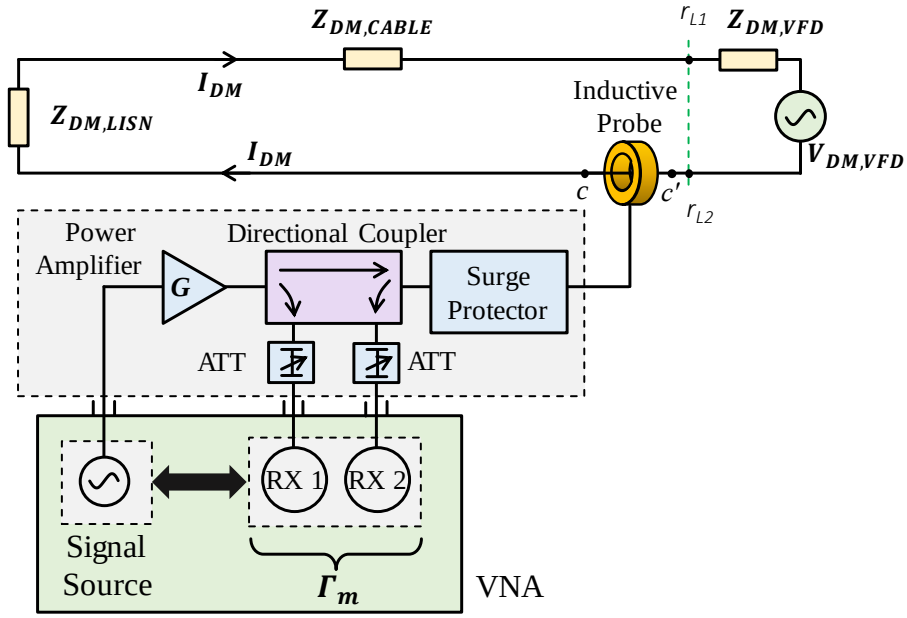

Fig. 6-2. DM Equivalent circuit of a VFD under operating conditions.

The DM equivalent circuit of the setup is shown in Fig. 6-2. The DM impedances of the LISN, the cables, and the VFD are denoted by $\boldsymbol{Z_{DM,LISN}}$, $\boldsymbol{Z_{DM,CABLE}}$, and $\boldsymbol{Z_{DM,VFD}}$, respectively. The equivalent DM noise source voltage is denoted by $\boldsymbol{V_{DM,VFD}}$. The pre-measurement characterization is performed by terminating r_{L1}-r_{L2} under OSL conditions without the AC

power supply and the VFD. The frequency-dependent $\boldsymbol{h_1}$, $\boldsymbol{h_2}$, and $\boldsymbol{h_3}$ of the SPS are determined and shown in Fig. 6-3. Once the pre-characterization is completed, the AC power is turned on with the VFD energized. Then, the in-circuit DM impedance of the VFD is measured.

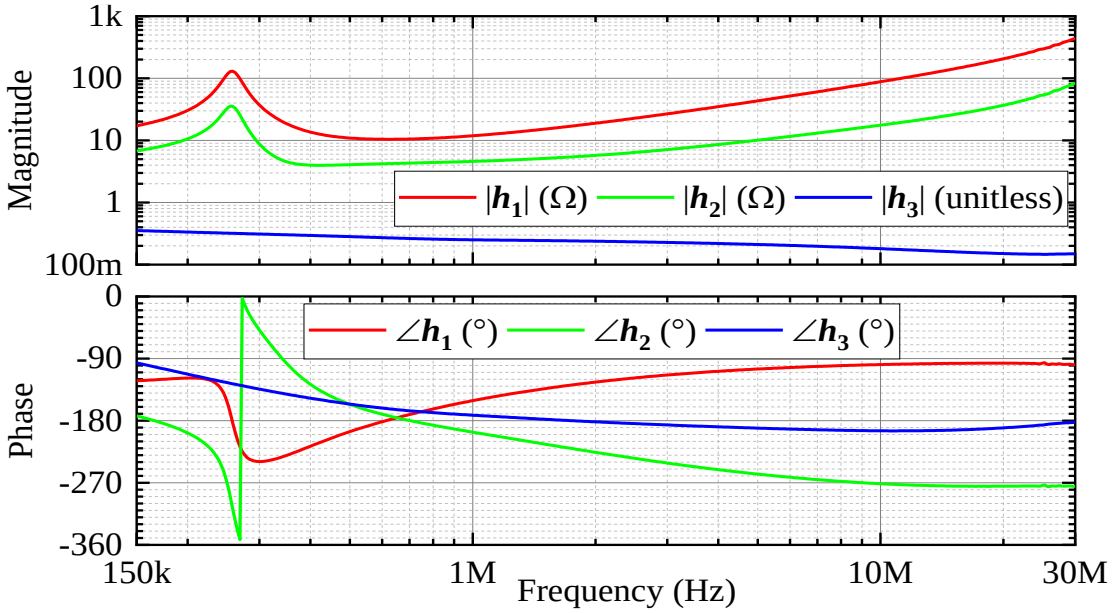

Fig. 6-3. Frequency-dependent $\boldsymbol{h_1}$, $\boldsymbol{h_2}$, and $\boldsymbol{h_3}$ for the SPS in DM impedance measurement.

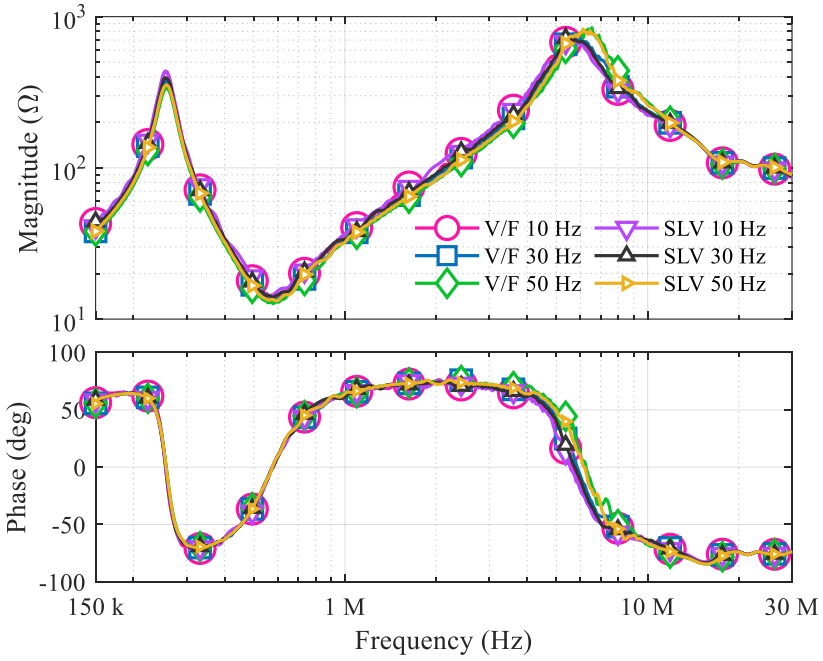

Fig. 6-4. DM impedance of the VFD at three speed settings (10 Hz, 30 Hz, 50 Hz) and two control modes (V/F and SLV).

The measured DM impedances with different modes and speed settings are shown in Fig. 6-4. It shows that the control modes and speed settings have a negligible impact on the in-circuit DM impedance. Therefore, a DM EMI filter can be designed based on the measured DM noise source impedance of the VFD.

6.1.2 SPS for Common-Mode Impedance Extraction

Fig. 6-5 depicts a VFD connected to an AC power grid through a LISN. An inductive probe is clamped onto the earth cable between the VFD and the LISN at the location *c*-*c′*. The resultant CM current is shown as $\boldsymbol{I_{CM}}$. r_{L1}, r_{L2}, and r_E denote the AC input measurement reference plane of the VFD at which the CM impedance will be measured.

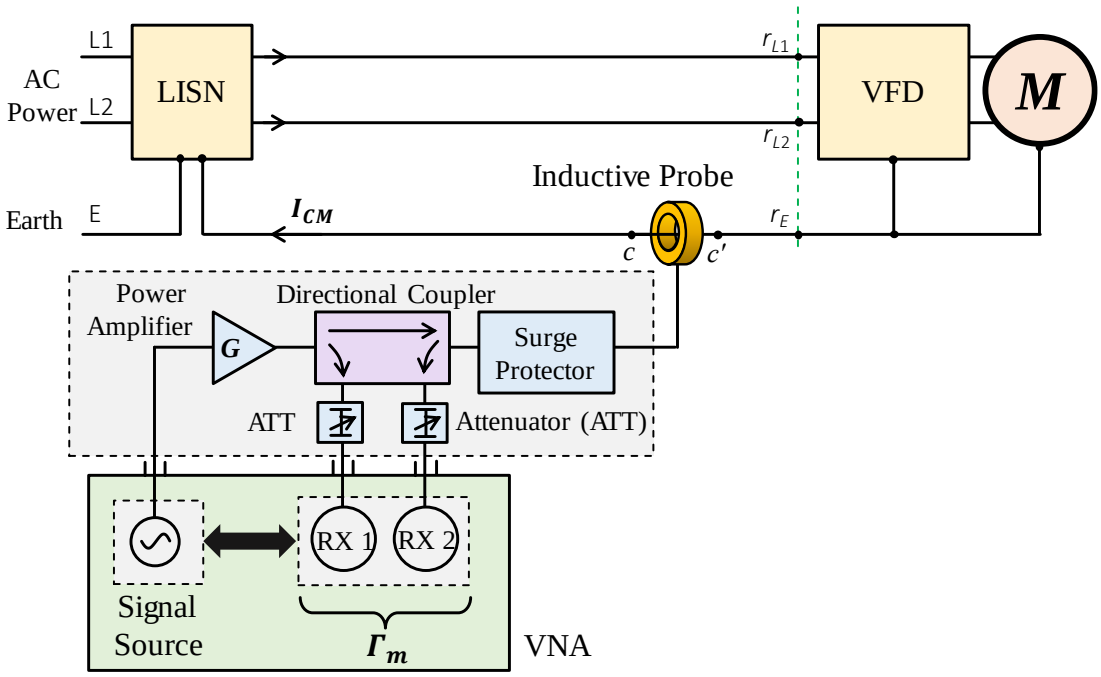

Fig. 6-5. CM impedance measurement of a VFD under operating conditions.

The CM equivalent circuit of the setup is given in Fig. 6-6. The CM impedances of the LISN, cables, and the VFD are denoted by $\boldsymbol{Z_{CM,LISN}}$, $\boldsymbol{Z_{CM,CABLE}}$, and $\boldsymbol{Z_{CM,VFD}}$. The equivalent CM noise source voltage is represented by $\boldsymbol{V_{CM,VFD}}$. Again, the pre-measurement characterization is performed with the OSL conditions without the AC power supply switched

off and the VFD disconnected. Note that during the pre-measurement characterization, r_{L1} and r_{L2} are shorted and treated as one terminal with r_E as another terminal. T. frequency-dependent $\boldsymbol{h_1}$, $\boldsymbol{h_2}$, and $\boldsymbol{h_3}$ of the SPS are determined and shown in Fig. 6-7.

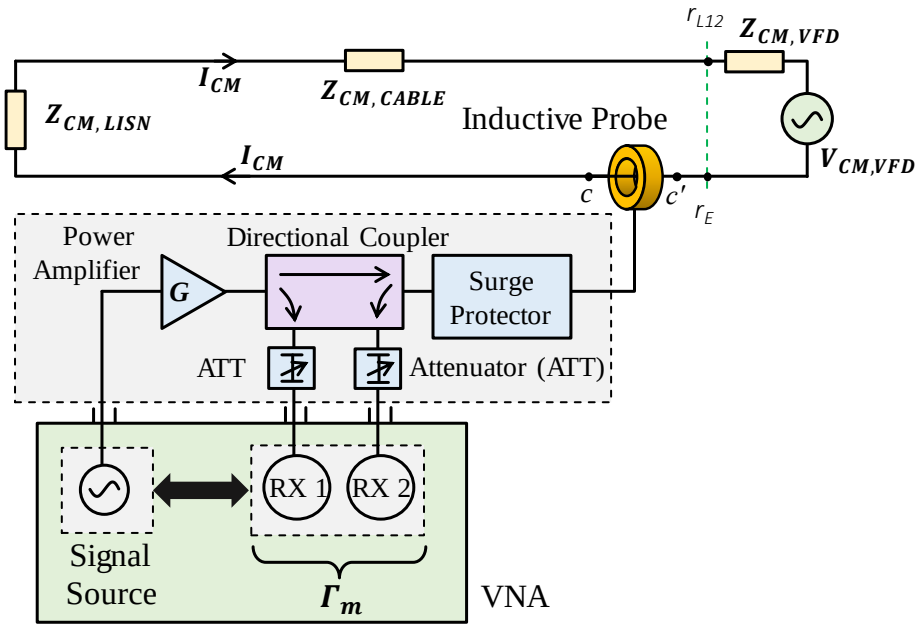

Fig. 6-6. CM Equivalent circuit of a VFD under operating conditions.

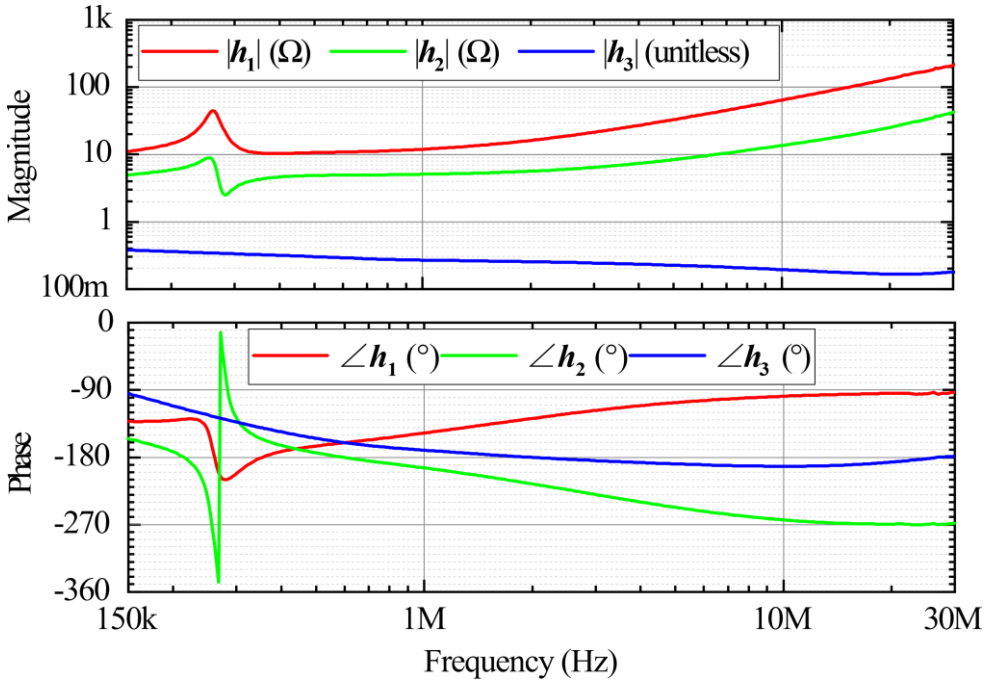

Fig. 6-7. Frequency-dependent $\boldsymbol{h_1}$, $\boldsymbol{h_2}$, and $\boldsymbol{h_3}$ parameters for the SPS in CM impedance measurement.

Once the pre-characterization is completed, the AC power is turned on and the VFD is energized. Then, the in-circuit CM impedance of the VFD is measured. The obtained CM impedances are shown in Fig. 6-8. Again, the CM impedance of the VFD is unaffected by the operating modes and speed settings. Hence, the CM noise source impedance of the VFD can be used for CM EMI filter design purposes.

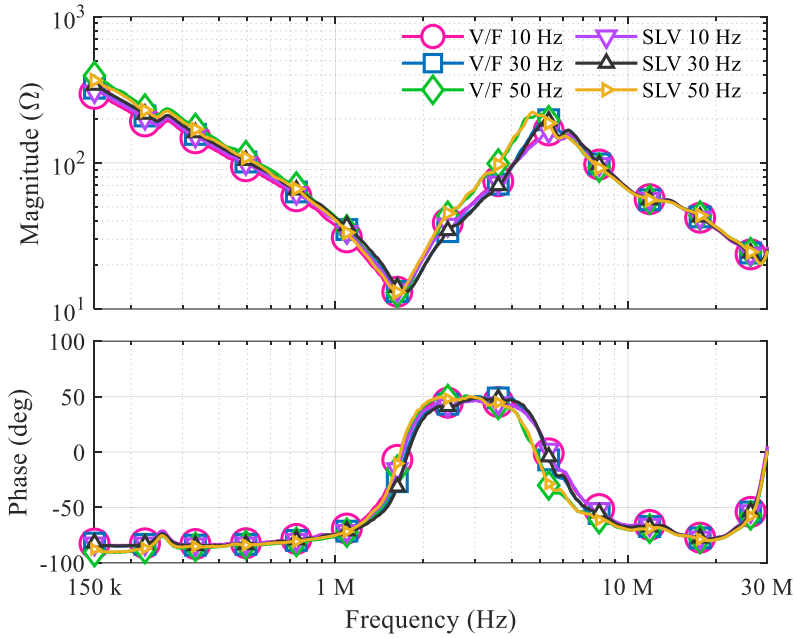

Fig. 6-8. CM impedance of a VFD at three speed settings (10 Hz, 30 Hz, 50 Hz) and two control modes (V/F and SLV).

6.2 Impedance Measurement of a Grid-Connected Induction Motor

This section illustrates another practical application to extract the in-circuit impedance of grid-connected induction motor. The in-circuit impedance of the induction motor is measured using three different measurement setups. The first one is SPS with FD-based instrumentation, the next one is SPS with TD-based instrumentation and the last one is based on the V-I measurement approach. The V-I measurement approach is served as a reference for validation

purposes. The individual measurement setups will be elaborated in detail in the following sub-sections followed by a comparison of the measured results obtained from the three different setups.

6.2.1 SPS with Frequency-Domain Based Instrumentation

Fig. 6-9 shows the SPS with FD-based instrumentation for in-circuit impedance measurement of an induction motor. The motor is connected to the power grid through a LISN (Electro-Metrics MIL 5-25/2). An inductive probe (FCC F-120-6A-3) is clamped onto one of the power cables at *c*-*c′*. The probe is connected to a VNA (Bode 100) through a power amplifier (Mini circuits LZY–22+) and an RF directional coupler (DC3010A). The power amplifier is necessary to ensure sufficient SNR. The two attenuators (AIM-Cambridge 27-9300-6 and AIM-Cambridge 27-9300-3) and a surge protector (SSC-N230/01) are incorporated in the SPS to protect the VNA input.

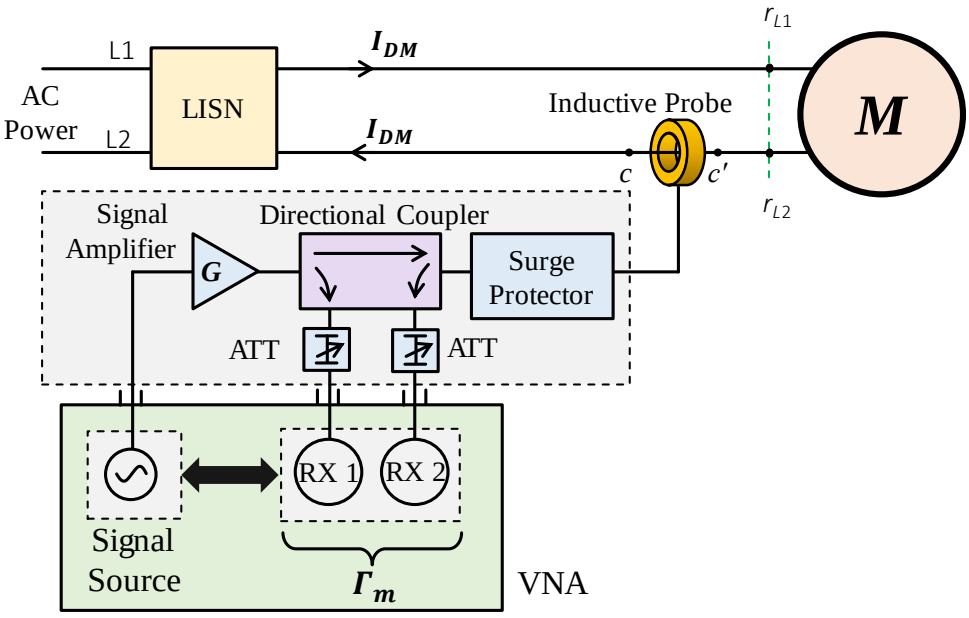

Fig. 6-9. SPS with FD-based instrumentation for in-circuit DM impedance measurement of an induction motor.

r_{L1}, and r_{L2} denote the reference plane of the SUT at which the impedance is measured. The pre-measurement characterization is performed with OSL conditions at r_{L1}-r_{L2} with the AC

power supply switched off and the induction motor disconnected. After the pre-measurement characterization, the AC power is reconnected back to the induction motor and the in-circuit DM impedance of the induction motor is measured. A photograph of the actual measurement setup is shown in Fig. 6-10.

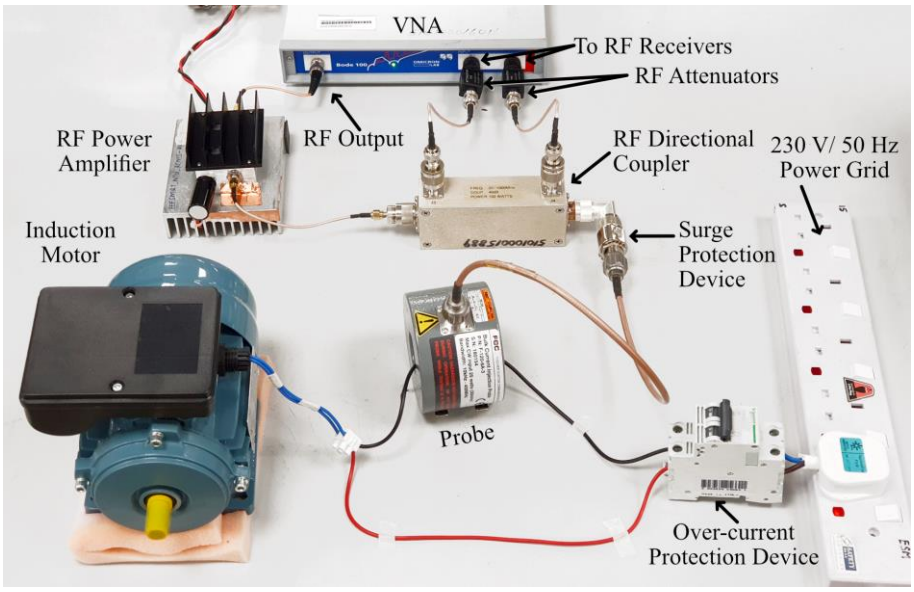

Fig. 6-10. In-circuit impedance measurement of an induction motor using the FD-based SPS.

6.2.2 Time-Domain Based SPS

Fig. 6-11 shows the SPS with TD-based instrumentation for in-circuit impedance measurement of an induction motor. The TD-based instrumentation comprises an SGAS with a two-channel ADC module (National Instruments PXI-5142) and a direct digital synthesis AWG (National Instruments PXI-5412). The motor is connected to the power grid through a LISN (Electro-Metrics MIL 5-25/2). An inductive probe (FCC F-120-6A-3) is mounted onto one of the power cables at *c*-*c′*. The probe is connected to the TD-based instrumentation through a power amplifier (Mini circuits LZY–22+) and an RF directional coupler (DC3010A). The power amplifier is to amplify the AWG signal output and provide sufficient SNR. Two attenuators (AIM-Cambridge 27-9300-6 and AIM-Cambridge 27-9300-3) and a surge protector (SSC-N230/01) are added to safeguard the SGAS from transients and surges. r_{L1}, and r_{L2} denote the reference

plane of the SUT at which the impedance is measured. The pre-measurement characterization is performed by OSL at r_{L1}-r_{L2} without the AC power supply and the induction motor. Once the pre-measurement characterization is done, the AC power is connected to the induction motor for in-circuit impedance measurement. A photograph of the actual measurement setup is shown in Fig. 6-13.

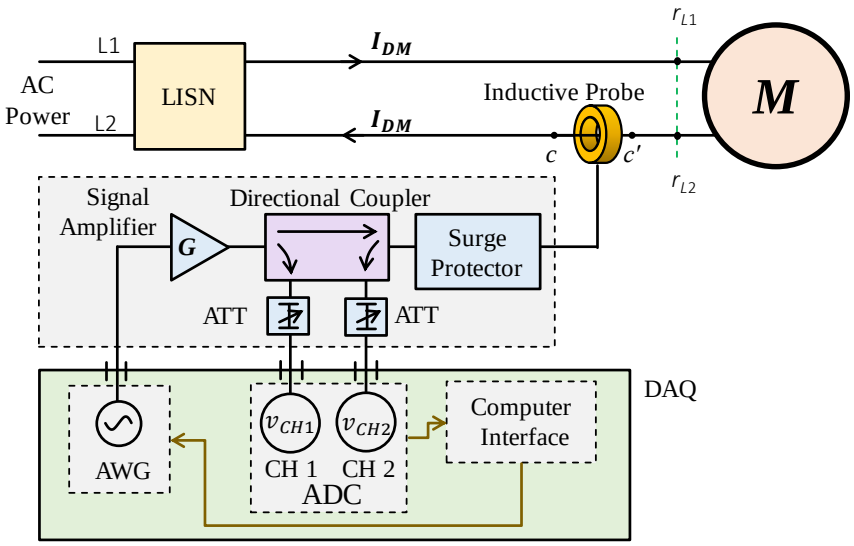

Fig. 6-11. SPS for in-circuit DM impedance measurement of an induction motor.

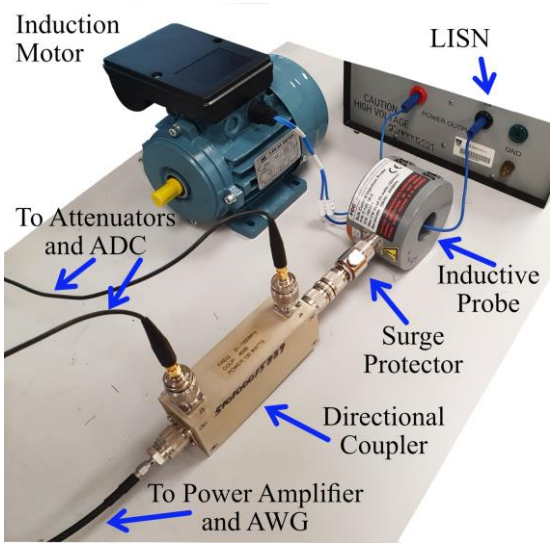

Fig. 6-12. In-circuit impedance measurement of an induction motor using TD-based SPS.

6.2.3 V-I Measurement approach

Fig. 6-13 shows a setup based on the well-established V-I measurement approach [43] to measue the in-circuit impedance of the induction motor. The excitation is provided by a signal generator (National Instruments PXI-5412) and it is injected into the SUT through an RF current injection probe (Solar 9144-1N). r_{L1}, and r_{L2} denote the reference plane of the SUT at which the impedance is measured. The terminal voltage $\boldsymbol{V_{DM}}$ at r_{L1}-r_{L2} is measured using a differential voltage probe (GDP-025, 0-25 MHz). As mentioned earlier, the V-I measurement setup requires a direct electrical contact to the energized induction motor, as shown in Fig. 6-13.

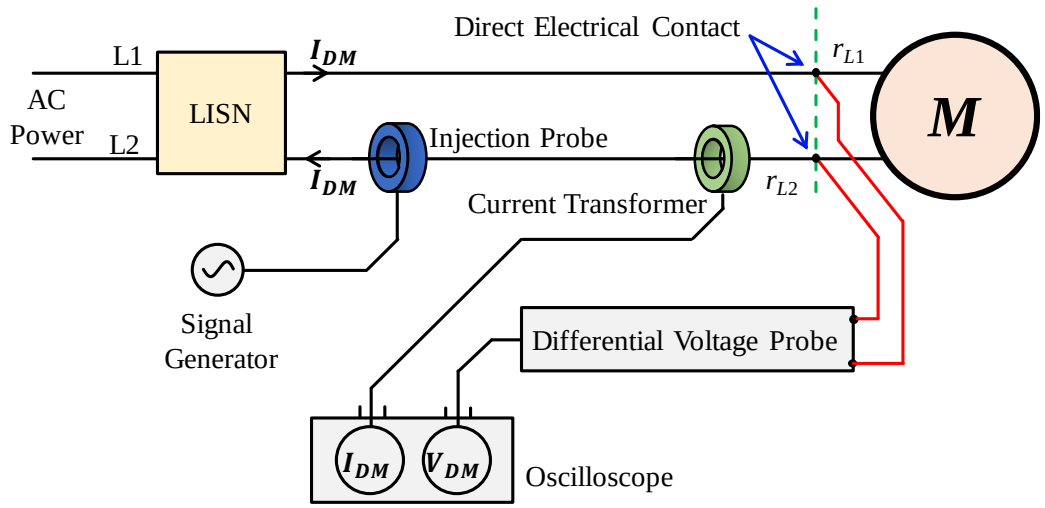

Fig. 6-13. V-I measurement approach setup for in-circuit impedance measurement of the induction motor.

The current $\boldsymbol{I_{DM}}$ through the SUT is sensed by a current transformer (Tektronix CT1, 25 kHz-1 GHz). It is to take note that the differential voltage probe has an effective bandwidth up to 25 MHz and therefore the maximum measurement frequency of the V-I approach stops at 25 MHz. The voltage and current measurements are obtained using a digital oscilloscope (R&S RTB2004). Then a fast Fourier transform (FFT) algorithm is applied to obtain the voltage and current in FD so that the in-circuit impedance of the induction motor can be computed. A photograph of the actual measurement setup is shown in Fig. 6-14.

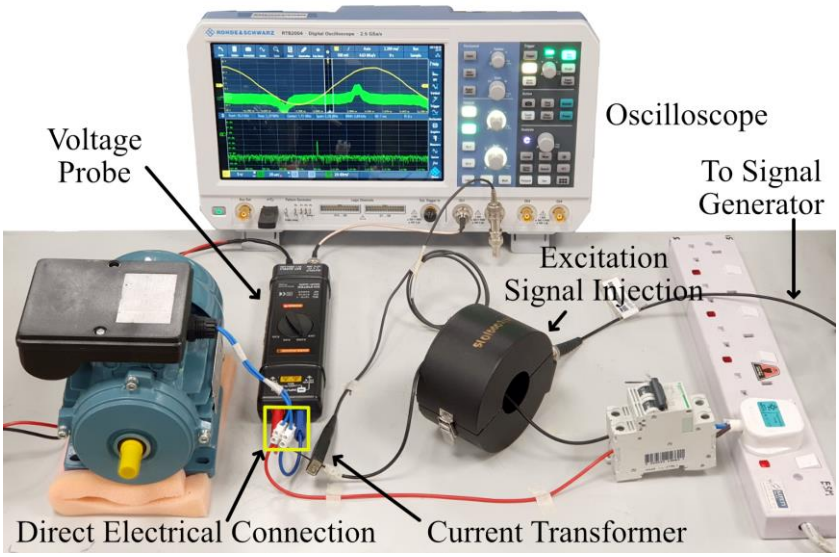

Fig. 6-14. Actual implementation of V-I measurement setup.

6.2.4 Measurement Results

As described in Section 5.1 of Chapter 5, an SNR above 30 dB yields good measurement accuracy. Therefore, the excitation level is adjusted to be higher than the noise of the energized SUT by 30 dB. The measured noise floor, excitation level, and the SNR using a current transformer (R&S EZ-17) and a spectrum analyzer (R&S FSH4) are shown in Fig. 6-15.

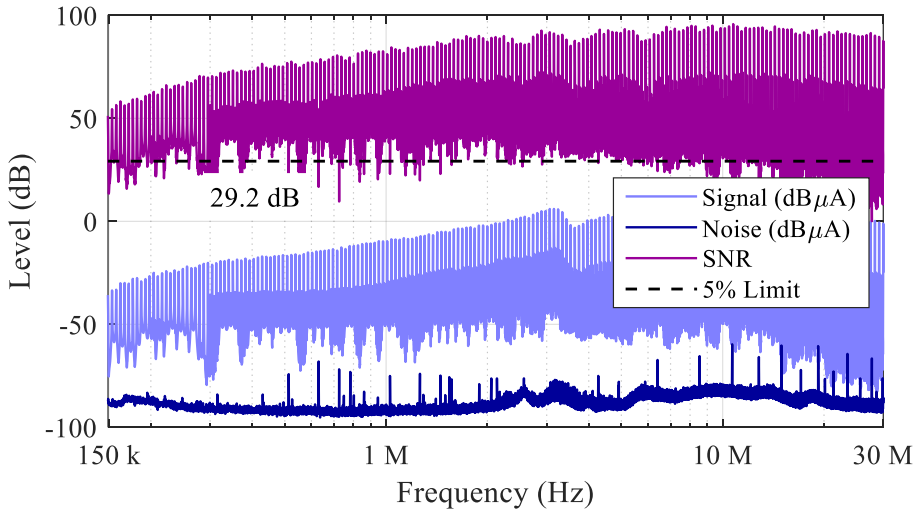

Fig. 6-15. Measured excitation signal, background noise, and SNR for the energized induction motor.

The measured in-circuit impedance response using the FD-based SPS, TD-based SPS, and the V-I measurement approach are compared in Fig. 6-16. In general, all three setups show relatively good agreement in the considered frequency range.

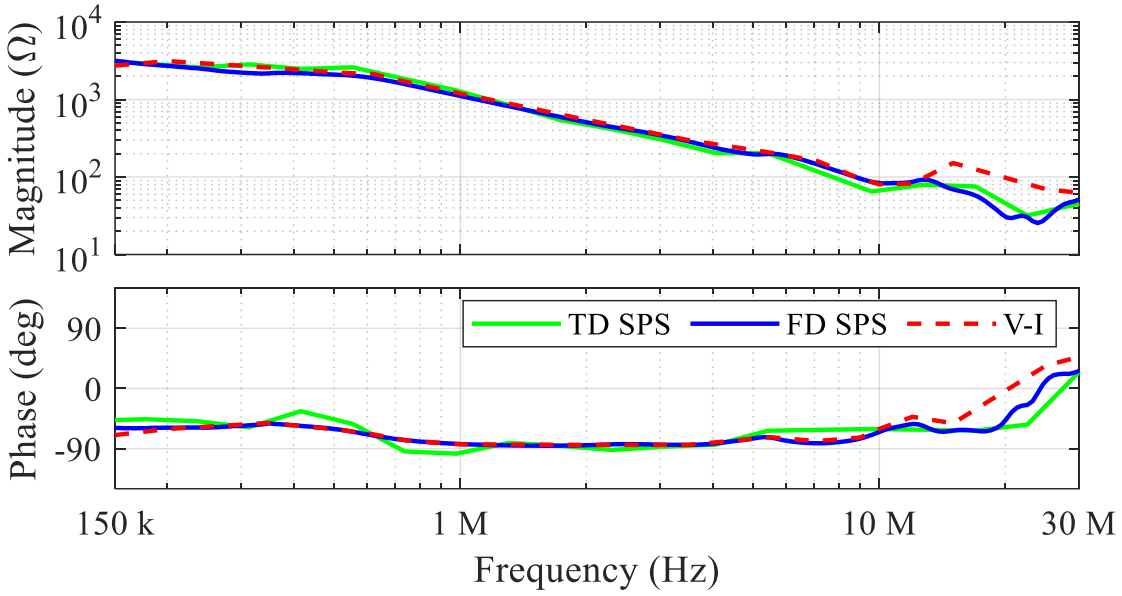

Fig. 6-16. In-circuit impedance of the induction motor measured by TD-based SPS, FD-based SPS and V-I measurement approach.

6.3 Discussion and Summary

The proposed SPS has been applied for two practical test cases. The first case has shown the use of FD-based SPS to extract the DM and CM noise source impedances of an energized VFD system under various operating modes and speed settings. The extracted DM and CM noise source impedances facilitate the systematic designs of DM and CM EMI filters so that the respective conducted DM and CM emissions can be suppressed below the required limits. The second case has demonstrated the ability to extract the in-circuit impedance measurement of an induction motor for condition monitoring purposes. The two SPSs with both FD-based and TD-based instrumentations are compared with the conventional V-I approach. The comparison has shown that the measurement results obtained from the SPS agree well with

that from the V-I measurement approach. However, it is to take note that the SPS requires no direct electrical contact to the energized SUT and only needs a single inductive probe.

Chapter 7 Conclusion and Future Works

7.1 Conclusions

The basic theory behind the SPS for in-circuit impedance measurement has been described and validated experimentally. The SPS not only reduces the hardware overhead by reducing two probes to only one probe but also overcomes the limitations of the TPS, such as probe-to-probe coupling and the pre-characterization errors of the inductive probes with standard calibration fixture.

In conclusion, the work presented in this thesis has resulted in the following key achievements:

- Derivation of the theory behind SPS for in-circuit impedance measurement with both FD and TD-based instrumentations and validate them experimentally.
- Development of a pre-measurement characterization of the SPS through three distinct impedance terminations to cancel all potential measurement errors contributed by the setup and the instrumentation.
- Successful incorporation of the signal amplification and the protection modules in the SPS to preserve its measurement accuracy and ruggedness.
- Detailed analysis of the impact of SNR on the measurement accuracy of the SPS.
- Proposal of an error correction method to recover the measurement accuracy of the SPS under the situation of poor SNR.

- Incorporation of a quasi-log multitone excitation signal synthesis technique with TD-based instrumentation to extract in-circuit impedance efficiently across a wide frequency band.
- Demonstration of the SPS for in-circuit impedance measurement under practical test cases for EMI filter design and condition monitoring purposes.

7.2 Recommended Future Works

A robust and rugged in-circuit impedance measurement based on SPS has been developed and validated. Further works on the post-processing of the in-circuit measurement data should be developed so that its scope of applications can be expanded further. The following future works are worth exploring:

- Long-term in-circuit impedance monitoring and statistical analysis to predict the renewal timeline for critical assets, such as induction motors and transformers.
- Wavelet-based analysis techniques to further improve the efficiency of time-variant impedance measurement.
- Analysis of the factors affecting the dynamic range of the proposed technique such as the inductive probe selection and a comparison with two-probe counterpart.
- Analysis of measurement uncertainty under extreme physical conditions.
- Selection of a suitable time-domain or frequency measurement instrument to achieve certain measurement specifications.

AUTHOR'S PUBLICATIONS

Journal Publications

As the first Author:

1. *A. Weerasinghe*, Z. Zhao, N. B. Narampanawe, Z. Yang, T. Svimonishvili and K. Y. See, "Single-Probe Inductively Coupled In-Circuit Impedance Measurement," in *IEEE Transactions on Electromagnetic Compatibility*, vol. 64, no. 1, pp. 2-10, Feb. 2022.
2. A. Weerasinghe, Z. Zhao, Q. Sun, F. Fan, P. Tu, W. Wang and K. Y. See, "A Novel Single-Probe Setup for Multi-Frequency Simultaneous Measurement of In-Circuit Impedance" *IEEE Transactions on Industrisal Electronics*, (submitted and under review).

As co-Author:

1. Z. Zhao, A. Weerasinghe, W. Wang, E. K. Chua, and K. Y. See, "Eliminating the Effect of Probe-to-Probe Coupling in Inductive Coupling Method for In-Circuit Impedance Measurement," in *IEEE Transactions on Instrumentation and Measurement*, vol. 70, pp. 1-8, 2021.
2. Z. Zhao, K. Y. See, W. Wang, E. Chua, A. Weerasinghe, Z. Yang, and W. Chen, "Voltage-Dependent Capacitance Extraction of SiC Power MOSFETs Using Inductively Coupled In-Circuit Impedance Measurement Technique," in *IEEE Transactions on Electromagnetic Compatibility*, vol. 61, no. 4, pp. 1322-1328, Aug. 2019.
3. Z. Zhao, K. Y. See, E. Chua, A. S. Narayanan, W. Chen and A. Weerasinghe, "Time-Variant In-Circuit Impedance Monitoring Based on the Inductive Coupling Method,"

in *IEEE Transactions on Instrumentation and Measurement*, vol. 68, no. 1, pp. 169-176, Jan. 2019.

Conference Publications

As the first author:

1. A. Weerasinghe, Z. Zhao, F. Fan, P. Tu, K. Y. See, "In-Circuit Differential-Mode Impedance Extraction at the AC Input of a Motor Drive System," *Asia-Pacific International Symposium on Electromagnetic Compatibility (APEMC)*, Bali, 2021.
2. A. Weerasinghe, Z. Zhao, W. Wang, H. Jie, and K. Y. See, "Inductively Coupled In-Circuit Impedance Measurement Under Low Signal-To-Noise Ratio," *Asia-Pacific International Symposium on Electromagnetic Compatibility (APEMC)*, Beijing, 2022. (Accepted)

As co-author:

1. Z. Zhao, F. Fan, A. Weerasinghe, P. Tu, K. Y. See, "Measurement of In-Circuit Common-Mode Impedance at the AC Input of a Motor Drive System," *Asia-Pacific International Symposium on Electromagnetic Compatibility (APEMC)*, Bali, 2021.
2. K. Li, K. Y. See, N. B. Narampanawe, A. Weerasinghe, and V. H. Y. Tong, "Condition Monitoring of Power Feeder with Multiple Parallel Cables Based on Inductive Coupling Method," *in 2018 International Conference on Intelligent Rail Transportation (ICIRT)*, Singapore, 2018, pp. 1–4
3. Arun Shankar Narayanan, Zhenyu Zhao, Eng Kee Chua, Arjun Weerasinghe, K. Y. See, "Study on the Parameters Affecting the Impedance Extraction Accuracy by Inductive Coupling Method," i*n 2018 International Conference on Intelligent Rail Transportation (ICIRT)*, Singapore, 2018, pp. 1–5.

REFERENCES

[1] A. V. A. V. Timbus, R. Teodorescu, F. Blaabjerg, and U. Borup, "Online Grid Measurement and ENS Detection for PV Inverter Running on Highly Inductive Grid," *IEEE Power Electron. Lett.*, vol. 2, no. 3, pp. 77–82, Sep. 2004, doi: 10.1109/LPEL.2004.834921.

[2] M. S. B. Rathnayaka, "Non-intrusive inductively coupled method for condition monitoring of electrical systems," Nanyang Technological University, 2018.

[3] P. A. Lindahl, M. A. Cornachione, and S. R. Shaw, "A Time-Domain Least Squares Approach to Electrochemical Impedance Spectroscopy," *IEEE Trans. Instrum. Meas.*, vol. 61, no. 12, pp. 3303–3311, Dec. 2012, doi: 10.1109/TIM.2012.2210457.

[4] S. Bin Lee and T. G. Habetler, "An online stator winding resistance estimation technique for temperature monitoring of line-connected induction machines," *IEEE Trans. Ind. Appl.*, vol. 39, no. 3, pp. 685–694, 2003, doi: 10.1109/TIA.2003.811789.

[5] A. M. Pasdar, I. H. Cavdar, and Y. Sozer, "Power-Line Impedance Estimation at FCC Band Based on Intelligent Home Appliances Status Detection Algorithm Through Their Individual Energy and Impedance Signatures," *IEEE Trans. Power Deliv.*, vol. 29, no. 3, pp. 1407–1416, Jun. 2014, doi: 10.1109/TPWRD.2013.2286154.

[6] D. E. Budoya and F. G. Baptista, "A Comparative Study of Impedance Measurement Techniques for Structural Health Monitoring Applications," *IEEE Trans. Instrum. Meas.*, vol. 67, no. 4, pp. 912–924, 2018, doi: 10.1109/TIM.2018.2792854.

[7] D. K. Alves, R. L. A. A. Ribeiro, F. B. Costa, and T. O. A. Rocha, "Real-Time Wavelet-Based Grid Impedance Estimation Method," *IEEE Trans. Ind. Electron.*, vol. 66, no. 10, pp. 8263–8265, Oct. 2019, doi: 10.1109/TIE.2018.2870407.

[8] W. Chang, K. See, and B. Hu, "Characterization of Component Under DC Biasing Condition Using an Inductive Coupling Approach," *IEEE Trans. Instrum. Meas.*, vol. 59, no. 8, pp. 2109–2114, 2010, doi: 10.1109/TIM.2009.2031850.

[9] W.-Y. Chang, W.-S. Soh, K.-Y. See, and L.-B. Wang, "Extraction of Clock Driver Output Impedance for Signal Integrity Design," *IEEE Trans. Electromagn. Compat.*, vol. 53, no. 4, pp. 1034–1039, Nov. 2011, doi: 10.1109/TEMC.2011.2162096.

[10] K. Li, K. See, N. B. Narampanawe, A. Weerasinghe, and V. H. Y. Tong, "Condition Monitoring of Power Feeder with Multiple Parallel Cables Based on Inductive Coupling Method," in *2018 International Conference on Intelligent Rail Transportation (ICIRT)*, 2018, pp. 1–4, doi: 10.1109/ICIRT.2018.8641583.

[11] S. B. Rathnayaka and K. Y. See, "Early detection of induction motor's defects using an inductively coupled impedance extraction method," in *2017 IEEE International Electric Machines and Drives Conference (IEMDC)*, 2017, pp. 1–6, doi: 10.1109/IEMDC.2017.8002000.

[12] F. Huet, "A review of impedance measurements for determination of the state-of-charge or state-of-health of secondary batteries," *J. Power Sources*, vol. 70, no. 1, pp. 59–69, Jan. 1998, doi: 10.1016/S0378-7753(97)02665-7.

[13] D. A. Howey, P. D. Mitcheson, V. Yufit, G. J. Offer, and N. P. Brandon, "Online Measurement of Battery Impedance Using Motor Controller Excitation," *IEEE Trans. Veh. Technol.*, vol. 63, no. 6, pp. 2557–2566, Jul. 2014, doi: 10.1109/TVT.2013.2293597.

[14] Y. L. Familiant, K. A. Corzine, J. Huang, and M. Belkhayat, "Ac impedance measurement techniques," *2005 IEEE Int. Conf. Electr. Mach. Drives*, pp. 1850–1857, 2005, doi: 10.1109/iemdc.2005.195972.

[15] K. Kiatgamjorn, V. Tarateeraseth, and W. Khan-Ngern, "The comparison of the input impedance

measurement of SMPS between the resonance method and the insertion loss method," in *The 2007 ECTI International Conference*, 2007, pp. 97–100.

[16] A. Arya, M. W. Ahmad, N. Agarwal, and S. Anand, "Capacitor impedance estimation utilizing dc-link voltage oscillations in single phase inverter," *IET Power Electron.*, vol. 10, no. 9, pp. 1046–1053, Jul. 2017, doi: 10.1049/iet-pel.2016.0603.

[17] M. Sumner, B. Palethorpe, and D. W. P. Thomas, "Impedance Measurement for Improved Power Quality—Part 1: The Measurement Technique," *IEEE Trans. Power Deliv.*, vol. 19, no. 3, pp. 1442–1448, Jul. 2004, doi: 10.1109/TPWRD.2004.829873.

[18] G. Hallak, C. Niess, and G. Bumiller, "Accurate Low Access Impedance Measurements With Separated Load Impedance Measurements on the Power-Line Network," *IEEE Trans. Instrum. Meas.*, vol. 67, no. 10, pp. 2282–2293, Oct. 2018, doi: 10.1109/TIM.2018.2814138.

[19] X. Shang, D. Su, H. Xu, and Z. Peng, "A Noise Source Impedance Extraction Method for Operating SMPS Using Modified LISN and Simplified Calibration Procedure," *IEEE Trans. Power Electron.*, vol. 32, no. 6, pp. 4132–4139, 2017, doi: 10.1109/TPEL.2016.2631578.

[20] T. Funaki, N. Phankong, T. Kimoto, and T. Hikihara, "Measuring Terminal Capacitance and Its Voltage Dependency for High-Voltage Power Devices," *IEEE Trans. Power Electron.*, vol. 24, no. 6, pp. 1486–1493, Jun. 2009, doi: 10.1109/TPEL.2009.2016566.

[21] D. Junhong, "In-circuit RF impedance measurement for EMI filter design in switched mode power supplies," 2008.

[22] V. Tarateeraseth, K. Y. See, F. G. Canavero, and R. W. Chang, "Systematic Electromagnetic Interference Filter Design Based on Information From In-Circuit Impedance Measurements," *IEEE Trans. Electromagn. Compat.*, vol. 52, no. 3, pp. 588–598, 2010, doi: 10.1109/TEMC.2010.2046419.

[23] Z. Zhao, K. See, E. Chua, A. S. Narayanan, A. Weerasinghe, and W. Chen, "Extraction of voltage-dependent capacitances of SiC device through inductive coupling method," in *2018 IEEE International Symposium on Electromagnetic Compatibility and 2018 IEEE Asia-Pacific Symposium on Electromagnetic Compatibility (EMC/APEMC)*, 2018, pp. 1301–1304, doi: 10.1109/ISEMC.2018.8393999.

[24] M. F. Sultan, "Modeling of a Bulk Current Injection Setup for Susceptibility Threshold Measurements.," *IEEE Int. Symp. Electromagn. Compat.*, vol. 00, no. c, pp. 188–195, 1986, doi: 10.1109/isemc.1986.7568237.

[25] S. B. Rathnayaka, K. Y. See, and K. Li, "On-line impedance monitoring of transformer based on inductive coupling approach," *IEEE Trans. Dielectr. Electr. Insul.*, vol. 24, no. 2, pp. 1273–1279, 2017, doi: 10.1109/TDEI.2017.006111.

[26] F. Fan, K. Y. See, K. Li, X. Liu, M. A. Zagrodnik, and A. K. Gupta, "In-circuit common-mode impedance measurement for motor drive system," *2017 Asia-Pacific Int. Symp. Electromagn. Compat. APEMC 2017*, pp. 1–3, 2017, doi: 10.1109/APEMC.2017.7975408.

[27] Q. He, L. Y. Wang, and G. G. Yin, *System Identification Using Regular and Quantized Observations*. New York, NY: Springer New York, 2013.

[28] K. Li, A. Videt, and N. Idir, "Multiprobe Measurement Method for Voltage-Dependent Capacitances of Power Semiconductor Devices in High Voltage," *IEEE Trans. Power Electron.*, vol. 28, no. 11, pp. 5414–5422, 2013, doi: 10.1109/TPEL.2013.2240016.

[29] N. B. Narampanawe, K. Y. See, K. Li, and V. H. Y. Tong, "Condition Monitoring of High Voltage Power Delivery Path to Train using Non-Invasive Impedance Measurement Method," in *2018 International Conference on Intelligent Rail Transportation (ICIRT)*, 2018, pp. 1–5, doi: 10.1109/ICIRT.2018.8641567.

[30] Z. Zhao, F. Fan, W. Wang, Y. Liu, and K. Y. See, "Detection of Stator Interturn Short-Circuit Faults in Inverter-Fed Induction Motors by Online Common-Mode Impedance Monitoring," *IEEE Trans. Instrum. Meas.*, vol. 70, 2021, doi: 10.1109/TIM.2021.3066193.

[31] S. Kye Yak and D. Junhong, "Measurement of noise source impedance of SMPS using a two probes

approach," *IEEE Trans. Power Electron.*, vol. 19, no. 3, pp. 862–868, 2004, doi: 10.1109/TPEL.2004.826520.

[32] H. Yang, K. Y. See, R. Simanjorang, and K. R. Li, "Offline Health Diagnosis of Power Device Based on Nonintrusive Inductively Coupled Approach," *IEEE J. Emerg. Sel. Top. Power Electron.*, vol. 6, no. 4, pp. 2053–2059, 2018, doi: 10.1109/JESTPE.2018.2811753.

[33] S. B. Rathnayaka, K. Y. See, and K. Li, "Inductively coupled on-line impedance measurement for condition monitoring of electrical equipment," *IET Sci. Meas. Technol.*, vol. 12, no. 3, pp. 382–387, 2018, doi: 10.1049/iet-smt.2017.0083.

[34] Z. Zhao *et al.*, "Voltage-Dependent Capacitance Extraction of SiC Power mosfets Using Inductively Coupled In-Circuit Impedance Measurement Technique," *IEEE Trans. Electromagn. Compat.*, vol. 61, no. 4, pp. 1322–1328, 2019, doi: 10.1109/TEMC.2019.2914704.

[35] Z. Zhao *et al.*, "Online Insulation Fault Detection of Stator Winding of Induction Motor based on a Non-Intrusive Impedance Extraction Technique," in *2018 International Conference on Intelligent Rail Transportation (ICIRT)*, 2018, pp. 1–5, doi: 10.1109/ICIRT.2018.8641627.

[36] Z. Zhao, "Measurement setup consideration and implementation for inductively coupled online impedance extraction," Nanyang Technological University, 2021.

[37] K. M. M. Prabhu, *Window Functions and Their Applications in Signal Processing*. CRC Press, 2018.

[38] Z. Zhao, T. Svimonishvili, and K. Y. See, "Two-probe online impedance measurement setup with improved SNR and enhanced ruggedness," *2020 IEEE 1st China Int. Youth Conf. Electr. Eng. CIYCEE 2020*, vol. 639798, pp. 1–6, 2020, doi: 10.1109/CIYCEE49808.2020.9332557.

[39] A. S. Narayanan *et al.*, "Study on the Parameters Affecting the Impedance Extraction Accuracy by Inductive Coupling Method," in *2018 International Conference on Intelligent Rail Transportation (ICIRT)*, Dec. 2018, pp. 1–5, doi: 10.1109/ICIRT.2018.8641624.

[40] Z. Zhao, A. Weerasinghe, W. Wang, E. K. Chua, and K. Y. See, "Eliminating the Effect of Probe-to-Probe Coupling in Inductive Coupling Method for In-Circuit Impedance Measurement," *IEEE Trans. Instrum. Meas.*, vol. 70, pp. 1–8, 2021, doi: 10.1109/TIM.2020.3013688.

[41] D. Pommerenke, R. Chundru, and S. Chandra, "A new test setup and method for the calibration of current clamps," *IEEE Trans. Electromagn. Compat.*, vol. 47, no. 2, pp. 335–343, 2005, doi: 10.1109/TEMC.2005.847381.

[42] I. Yokoshima, "RF Impedance Measurements by Voltage-Current Detection," *IEEE Trans. Instrum. Meas.*, vol. 42, no. 2, 1993, doi: 10.1109/19.278616.

[43] C. J. Kikkert, "An on-line PLC frequency impedance analyzer," *2013 IEEE Int. Conf. Smart Grid Commun. SmartGridComm 2013*, pp. 606–611, 2013, doi: 10.1109/SmartGridComm.2013.6688025.

[44] L. Asiminoaei, R. Teodorescu, F. Blaabjerg, and U. Borup, "A Digital Controlled PV-Inverter With Grid Impedance Estimation for ENS Detection," *IEEE Trans. Power Electron.*, vol. 20, no. 6, pp. 1480–1490, Nov. 2005, doi: 10.1109/TPEL.2005.857506.

[45] L. Angrisani, A. Baccigalupi, and A. Pietrosanto, "A digital signal-processing instrument for impedance measurement," *IEEE Trans. Instrum. Meas.*, vol. 45, no. 6, pp. 930–934, 1996, doi: 10.1109/19.543988.

[46] C. González, J. Pleite, V. Valdivia, and J. Sanz, "An overview of the on line application of frequency response analysis (FRA)," *IEEE Int. Symp. Ind. Electron.*, pp. 1294–1299, 2007, doi: 10.1109/ISIE.2007.4374785.

[47] R. A. Southwick and W. C. Dolle, "Line Impedance Measuring Instrumentation Utilizing Current Probe Coupling," *IEEE Trans. Electromagn. Compat.*, vol. EMC-13, no. 4, pp. 31–36, 1971, doi: 10.1109/TEMC.1971.303150.

[48] V. Tarateeraseth, B. Hu, K. Y. See, and F. G. Canavero, "Accurate Extraction of Noise Source Impedance of an SMPS Under Operating Conditions," *IEEE Trans. Power Electron.*, vol. 25, no. 1, pp. 111–117, 2010, doi: 10.1109/TPEL.2009.2024675.

[49] K. R. Li, K. Y. See, and X. M. Li, “Inductive Coupled In-Circuit Impedance Monitoring of Electrical System Using Two-Port ABCD Network Approach,” *IEEE Trans. Instrum. Meas.*, vol. 64, no. 9, pp. 2489–2495, 2015, doi: 10.1109/TIM.2015.2403091.

[50] Z. Zhao and K. Y. See, “A Multiprobe Inductive Coupling Method for Online Impedance Measurement of Electrical Devices Distributed in Multibranch Cables,” *IEEE Trans. Instrum. Meas.*, vol. 69, no. 9, pp. 5975–5977, 2020, doi: 10.1109/TIM.2020.3010669.

[51] F. Fan, K. Y. See, X. Liu, K. Li, and A. K. Gupta, “Systematic Common-Mode Filter Design for Inverter-Driven Motor System Based on In-Circuit Impedance Extraction,” *IEEE Trans. Electromagn. Compat.*, vol. 62, no. 5, pp. 1711–1722, 2020, doi: 10.1109/TEMC.2019.2944663.

[52] Z. Zhao, K.-Y. See, E.-K. Chua, A. S. Narayanan, W. Chen, and A. Weerasinghe, “Time-Variant In-Circuit Impedance Monitoring Based on the Inductive Coupling Method,” *IEEE Trans. Instrum. Meas.*, vol. 68, no. 1, pp. 169–176, Jan. 2019, doi: 10.1109/TIM.2018.2838198.

[53] F. Grassi, S. A. Pignari, and F. Marliani, “Improved lumped-Pi circuit model for bulk current injection probes,” *IEEE Int. Symp. Electromagn. Compat.*, vol. 2, pp. 451–456, 2005, doi: 10.1109/ISEMC.2005.1513557.

[54] M. N. Iddagoda, N. V. Venkatarayalu, and Y. B. Gan, “Characterization, calibration and macromodeling of RF current probes,” *APMC 2009 - Asia Pacific Microw. Conf. 2009*, pp. 629–632, 2009, doi: 10.1109/APMC.2009.5384143.

[55] F. Grassi, F. Marliani, and S. A. Pignari, “Circuit modeling of injection probes for bulk current injection,” *IEEE Trans. Electromagn. Compat.*, vol. 49, no. 3, pp. 563–576, 2007, doi: 10.1109/TEMC.2007.902385.

[56] D. M. Pozar, *Microwave Engineering*, 4th ed. Hoboken: Wiley, 2012.

[57] F. Grassi and S. A. Pignari, “Characterization of the bulk current injection calibration-jig for probe-model extraction,” in *2010 IEEE International Symposium on Electromagnetic Compatibility*, 2010, pp. 344–347, doi: 10.1109/ISEMC.2010.5711298.

[58] M. Prajapati and K. Y. See, “Extraction of equivalent impedance of photovoltaic panel under its actual operating conditions,” *2018 IEEE Int. Symp. Electromagn. Compat. 2018 IEEE Asia-Pacific Symp. Electromagn. Compat. EMC/APEMC 2018*, no. 1, pp. 1145–1149, 2018, doi: 10.1109/ISEMC.2018.8393967.

[59] G. Cerri, R. De Leo, V. M. Primiani, S. Pennesi, and P. Russo, “Wide-band characterization of current probes,” *IEEE Trans. Electromagn. Compat.*, vol. 45, no. 4, pp. 616–625, 2003, doi: 10.1109/TEMC.2003.819061.

[60] G. H. Bryant, *Principles of Microwave Measurements*. Institution of Engineering and Technology, 1993.

[61] M. Friese, “Multitone signals with low crest factor,” *IEEE Trans. Commun.*, vol. 45, no. 10, pp. 1338–1344, 1997, doi: 10.1109/26.634697.

[62] Y. Yang, F. Zhang, K. Tao, B. Sanchez, H. Wen, and Z. Teng, “An improved crest factor minimization algorithm to synthesize multisines with arbitrary spectrum,” *Physiol. Meas.*, vol. 36, no. 5, pp. 895–910, 2015, doi: 10.1088/0967-3334/36/5/895.

[63] F. M. Janeiro, Y. Hu, and P. M. Ramos, “Peak factor optimization of multi-harmonic signals using artificial bee colony algorithm,” *Meas. J. Int. Meas. Confed.*, vol. 150, p. 107040, 2020, doi: 10.1016/j.measurement.2019.107040.

[64] B. Sanchez, G. Vandersteen, R. Bragos, and J. Schoukens, “Basics of broadband impedance spectroscopy measurements using periodic excitations,” *Meas. Sci. Technol.*, vol. 23, no. 10, 2012, doi: 10.1088/0957-0233/23/10/105501.

[65] B. Sanchez, G. Vandersteen, R. Bragos, and J. Schoukens, “Optimal multisine excitation design for broadband electrical impedance spectroscopy,” *Meas. Sci. Technol.*, vol. 22, no. 11, 2011, doi: 10.1088/0957-0233/22/11/115601.

[66] P. Guillaume, J. Schoukens, R. Pintelon, and I. Kollái, “Crest-Factor Minimization Using Nonlinear Chebyshev Approximation Methods,” *IEEE Trans. Instrum. Meas.*, vol. 40, no. 6, pp. 982–989, 1991, doi: 10.1109/19.119778.

[67] M. Schroeder, “Synthesis of low-peak-factor signals and binary sequences with low autocorrelation,” *IEEE Transactions on Information Theory*, vol. 16, no. 1. pp. 85–89, 1970, doi: 10.1109/TIT.1970.1054411.

[68] L. J. Greenstein and P. J. Fitzgerald, “Phasing Multitone Signals to Minimize Peak Factors,” *IEEE Trans. Commun.*, vol. 29, no. 7, pp. 1072–1074, 1981, doi: 10.1109/TCOM.1981.1095086.

[69] O. I. Olayiwola and P. S. Barendse, “Characterization of Silicon-Based Photovoltaic Cells Using Broadband Impedance Spectroscopy,” *IEEE Trans. Ind. Appl.*, vol. 54, no. 6, pp. 6309–6319, 2018, doi: 10.1109/TIA.2018.2850025.

[70] E. Geerardyn, Y. Rolain, and J. Schoukens, “Design of quasi-logarithmic multisine excitations for robust broad frequency band measurements,” *IEEE Trans. Instrum. Meas.*, vol. 62, no. 5, pp. 1364–1372, 2013, doi: 10.1109/TIM.2012.2232474.

[71] H. Zhivomirov, “A Novel Visual Representation of the Signals in the Time-Frequency Domain,” *Univ. Politeh. Bucharest Sci. Bull. Ser. C-Electrical Eng. Comput. Sci.*, vol. 80, no. 3, pp. 75–84, 2018.

[72] F. Fan, K. Y. See, K. Li, J. K. Banda, X. Liu, and A. K. Gupta, “Efficient inductive coupled in-circuit impedance extraction with enhanced SNR and instrument protection,” in *2018 IEEE International Symposium on Electromagnetic Compatibility and 2018 IEEE Asia-Pacific Symposium on Electromagnetic Compatibility (EMC/APEMC)*, 2018, pp. 1288–1292, doi: 10.1109/ISEMC.2018.8393996.